Chapter 1

Introduction

1.1 Background

Gold was the motive which led to the European colonisation of Zimbabwe, and it has been the mainstay of its prosperity until recent times (Swift, 1961). Zimbabwe is one of the major gold producers in the world (Foster et al., 1986). In Zimbabwe, gold mineralization is found mainly in greenstone belts and is associated with sulphides such as pyrrhotite and pyrite. The gold mineralization is hosted by a variety of lithologies which lie at different stratigraphical horizons within the greenstone belts (Vinyu, 1994).

A geophysical survey to locate areas of gold mineralization was carried out on Lorna Doone farm, which is situated on the Harare-Bindura-Shamva greenstone belt. This greenstone belt is located in the NE of the Zimbabwe Craton. It is one of the largest greenstone belts in the craton, measuring up to 140 km NE-SW and 80 km NW-SE (Campbell and Pittfield, 1994).

1.2 The Survey Area

Lorna Doone farm is located near Domboshava some 40 km from Harare's city centre. There are several boreholes and a water tank constructed on the farm. The main activity there is dairy farming with about ninety cows on the farm; therefore most of the land is divided into paddocks. Finished milk products are produced on the farm including fresh milk, sour milk, cheese and yoghurt. Surrounding small scale and commercial farms produce soya beans, maize, ground nuts and winter wheat. On Willesden farm, adjacent to the survey area, there are small scale mining activities for gold from claims which are reporting an average grade of 45 g per tonne (Chiwalo, 2006, pers. comm.).

The landscape of the survey area is hilly with a mountain covering almost half of the study area. Fig. 1.1 shows the topography of the surveyed area. The topographic data were taken using a Garmin Etrex Global Positioning System receiver. The map shows that the elevation values are increasing towards the SE part of the farm, rising up to a conical hill. The NW corner is low lying.

The vegetation on the red greenstone soils consists of mainly indigenous trees including the mutsatsati, mukarati, muunga, mupfuti, muhacha, mutamba, muchecheni, msasa, muzhanje and munhondo trees. A few exotic trees are also present which include the jacaranda, cyprus and gum trees. The geology of the study area is given in Fig 1.3 below.

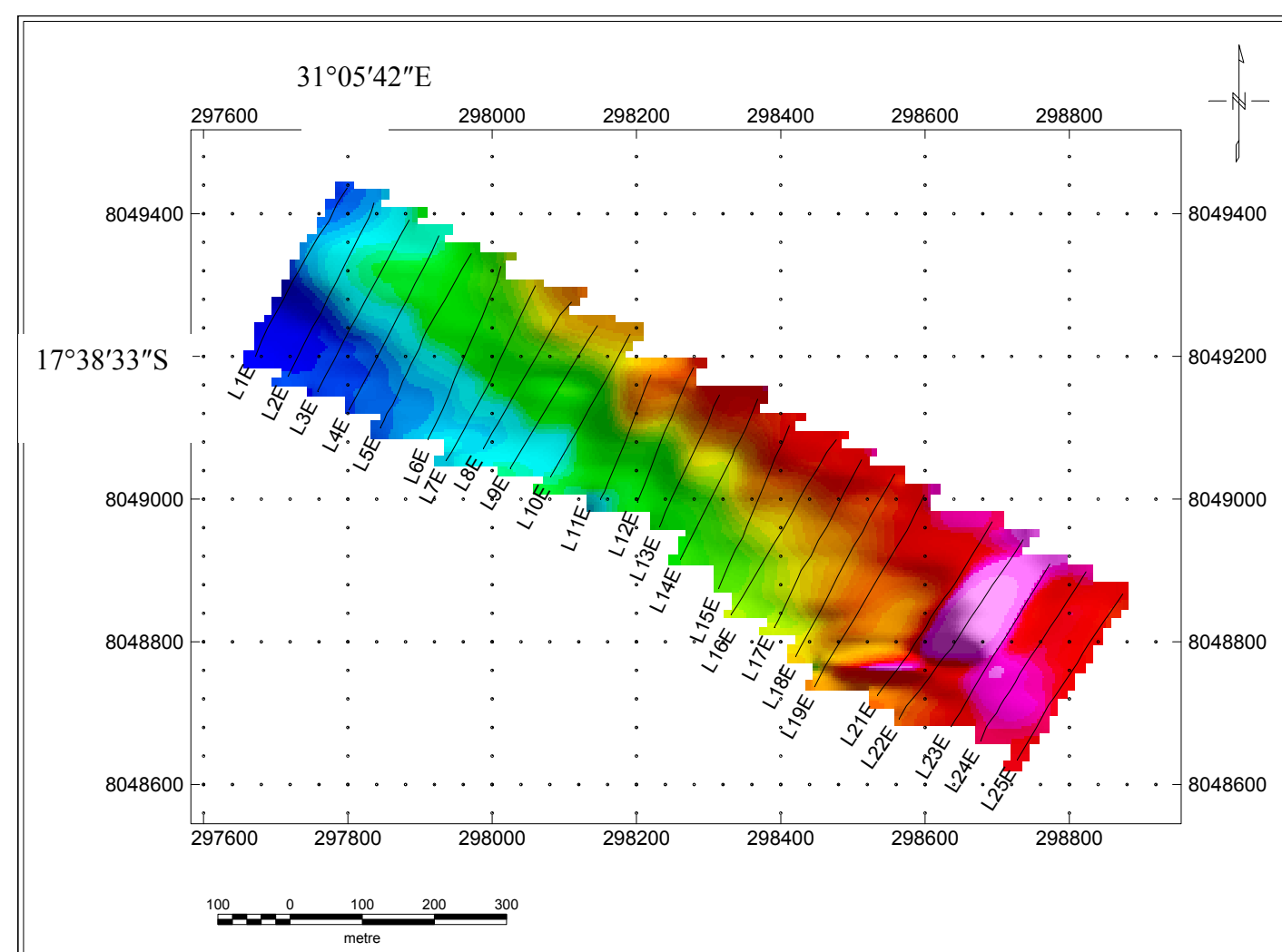


Fig. 1.1 The topography map. Note that the surveyed lines are represented by say L1E. Elevations are metres above sea level.

1.3 Regional Geology

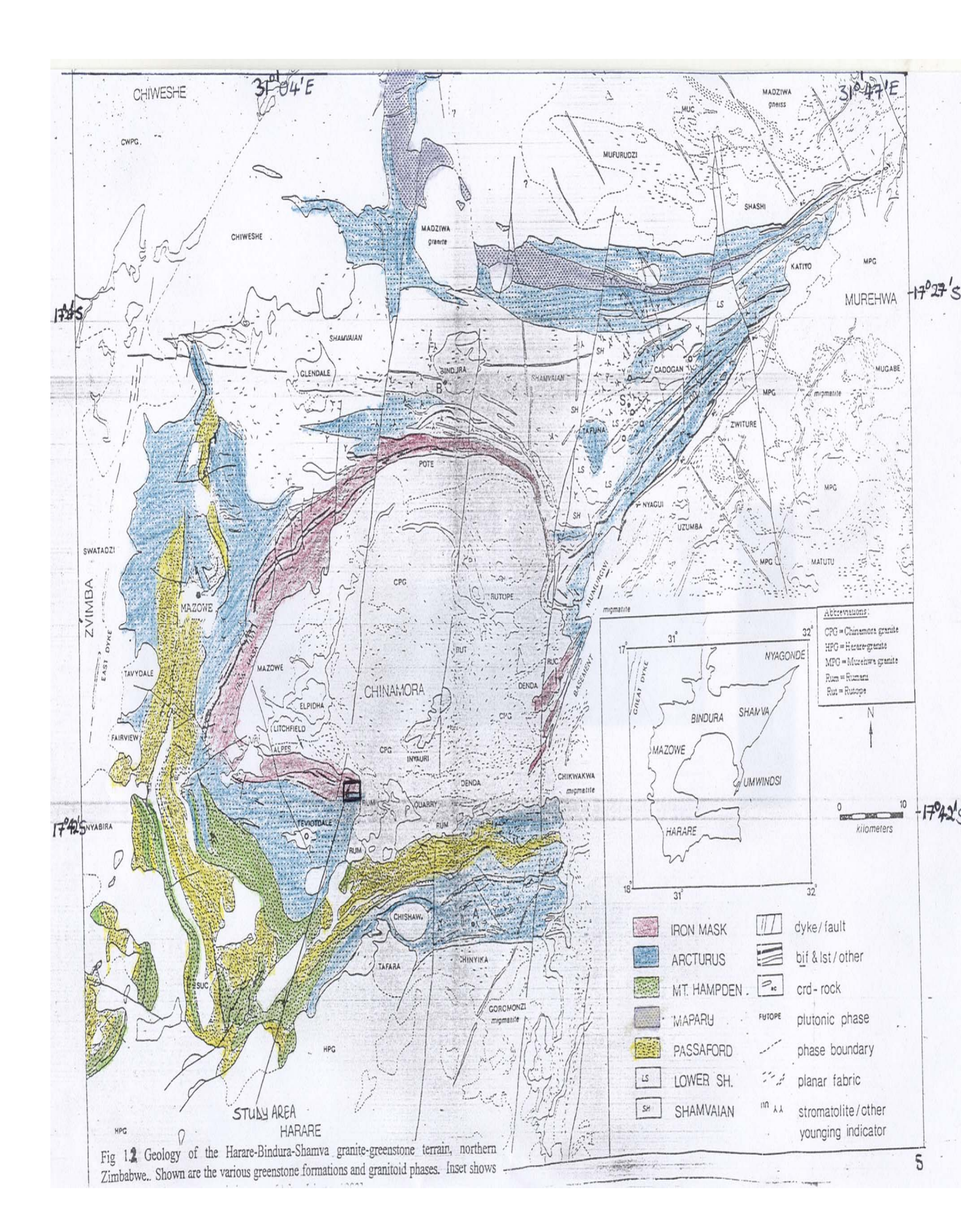
The regional geology of the study area consists of younger intrusive granites, granodiorite-adamellite and tonalities, and falls under the Harare-Bindura-Shamva greenstone belt (Fig. 1.2). This belt comprises of the meta-volcano-sedimentary succession, related meta-intrusive rocks and a range of meta-basaltic lithologies, hence it is dominantly a succession of metamorphosed felsic volcanics. Rocks of the Harare-Bindura-Shamva greenstone belt are divided into four formations based on lithology (Baldock, 1991). These are the:

- Iron Mask Formation,
- Arcturus Formation,
- Mt Hampden Formation and
- Passaford Formation.

The Mt Hampden Formation and Passaford Formations do not exist in the study area (Fig. 1.2).

1.3.1 The Iron Mask Formation

The Iron Mask Formation is made up of folded and sheared felsic meta-volcanic rocks, with associated minor meta-sediments. A bimodal pile of ultramafic and mafic lavas disconformably overlies rocks of this formation. The rocks are basically felsic pyroclastics with minor intercalations of banded iron formations and limestone (Baldock,



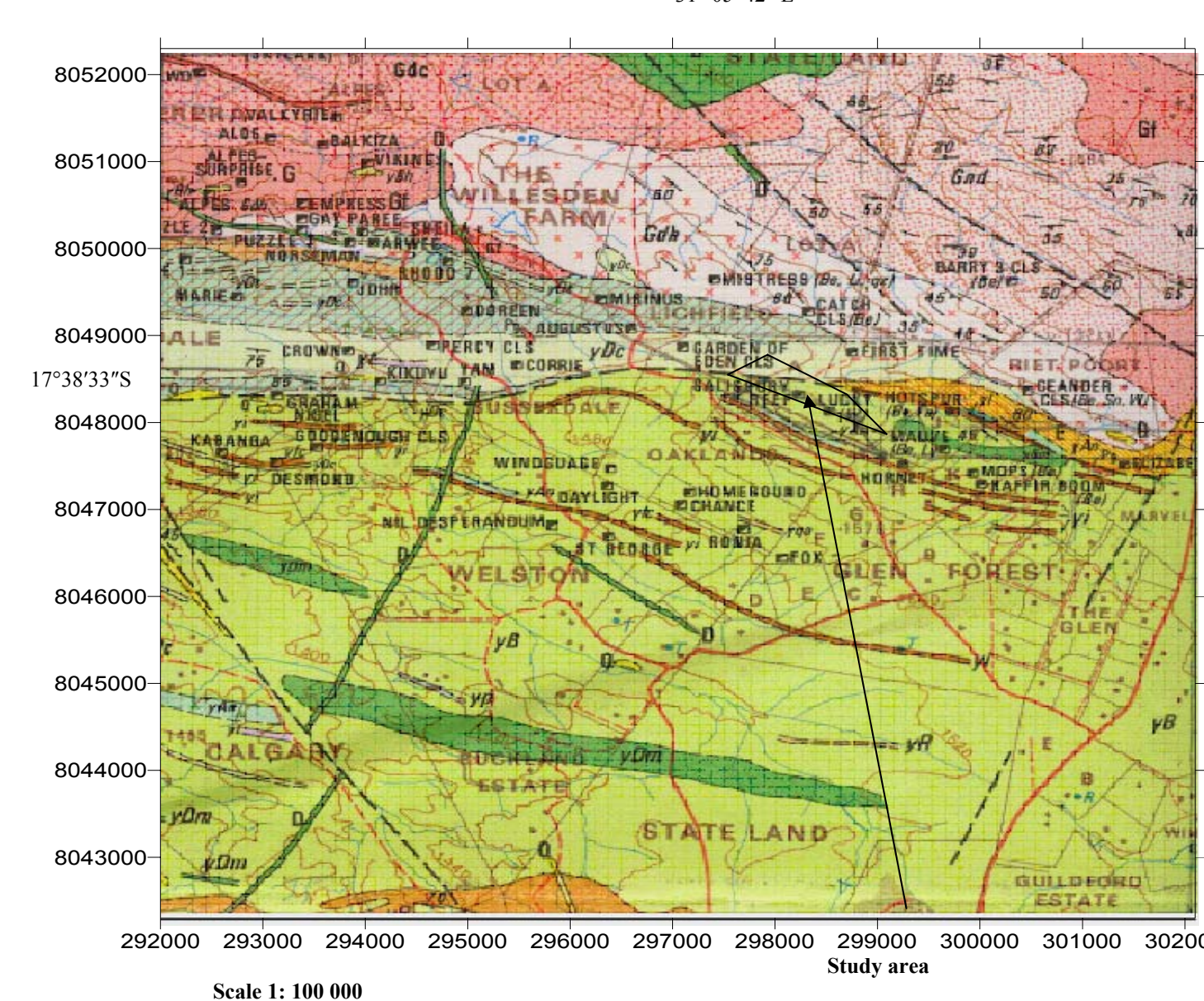
1991). The Iron Mask Formation structurally overlies the Chinamora batholith and it comprises of calc-alkaline felsic volcanic rocks, mainly metadacites and interbanded horizons of meta-andesites with prominent horizons of banded or gossaneous ironstone and ferruginous quartzite. Shear zone related gold mineralization in quartz veins occurs in felsic metavolcaniclastics of this formation (Jelsma, 1993).

1.3.2 The Arcturus Formation

This is a 3 – 4 km thick sequence of mafic meta-volcanic rocks that consists mainly of the metabasalts, subordinate ultramafites, metagabbro, metadolerite, meta-andesite, metasediments and minor iron formations (Baldock, 1991). The uppermost units within this formation are stratigraphically intercalated with the rocks of the Mt Hampden Formation (Vinyu, 1994). Intercalated within the meta-volcanics are horizons of banded iron formation, gossaneous ironstone, ferruginous quartzite and marble, casilicate rocks and some felsic metavolcanics (Jelsma, 1993).

1.4 Local Geology

The rocks are mainly greenstones which include andesites and basalts (Fig. 1.3). Granites, banded ironstones and white quartz are also found in the area. A distinct granitic outcrop could be seen striking NW – SE towards the northern end of Lorna Doone farm.



Key

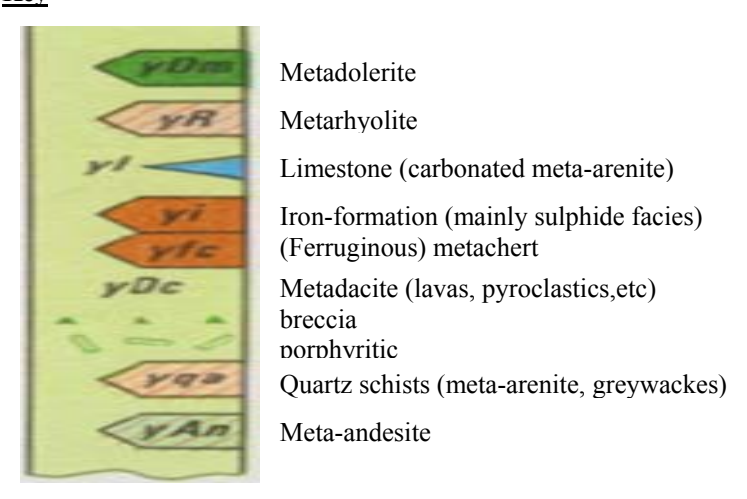


Fig. 1.3 The local geology map. After Balbock (1991).

1.5 Present Geophysical Work

The objective of this study was to locate geophysical anomalous areas which could be associated with possible gold mineralization on Lorna Doone farm. Work commenced on 14 June 2006 and ended on 16 July 2006. A total of 24 lines ranging from 225 m to 312.5 m in length were cut during the first five days (Fig. 1.1). The lines had 50 m line spacing with 25 m station spacing. The stations were numbered in the N – S direction and the lines in a W - E direction. Coordinates of the stations were taken using a Garmin Etrex Global Positioning System receiver with an accuracy of +/- 5 m. The induced polarization and magnetic methods were used in the survey. There is no known previous geophysical work done in this area apart from the National Aeromagnetic Survey.

Chapter 2

The Magnetic Survey

2.1 Introduction

Magnetic surveys have found great use in mineral exploration, geological mapping, oil exploration, mapping ocean floor ages and archaeology of buried buildings. It is also used in hydrogeology to detect faults, contacts or dykes hopefully linked to aquifers (Dobrin and Savit, 1998). They play an important role in mineral exploration because many mineral deposits are associated with anomalous magnetite concentrations. The magnetic method depends on measuring accurately the anomalies of the local geomagnetic field produced by the variations in the intensity of magnetization of different rock formations (Telford et al., 1990).

2.2 Theory

2.2.1 The Earth's Magnetic Field

Magnetic anomalies arise from the interaction of the Earth's main magnetic field with the rocks of the Earth's crust. The Earth's magnetic field arises from several different sources, i.e.:

- the Earth's core which contributes about 90% of the field,
- variations in the remanence and susceptibility of crustal rocks,
- small diurnal variations arising from the ionosphere, and
- cultural effects associated with man-made structures such as power lines, bridges, telephone lines, fences etc (Telford et al., 1990).

The main component of the geomagnetic field is called the dipolar field. It behaves to a first order approximation like a magnetic dipole located at the centre of the Earth but inclined at 11.5° to the rotational axis, Fig. 2.1 (Reynolds, 1997).

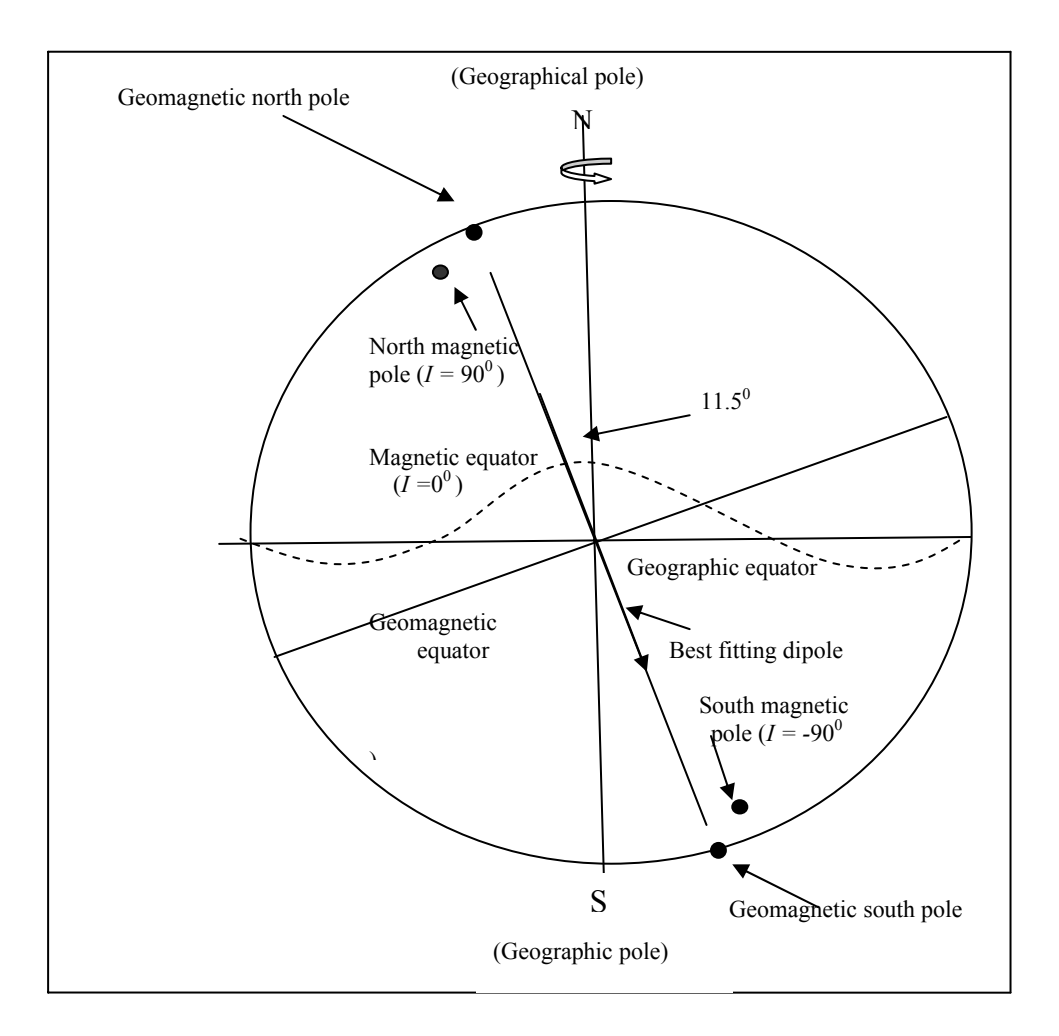


Fig. 2.1. The field due to an inclined geocentric dipole. After Reynolds (1997).

2.2.2 The Geomagnetic Elements

There are seven interrelated magnetic elements as shown in Fig. 2.2 below. These are **X**, **Y**, **Z**, *D*, *I*, **H** and **F** (Dobrin and Savit, 1988). The total magnetic field **F** is a vector which varies in magnitude and direction all over the Earth's surface. **H** is its

horizontal component which makes an angle D with true North. D is the declination (i.e. the difference between true North and magnetic North) and is positive East and negative West. I is the inclination of F or dip and is positive down and negative up. F can be resolved into 3 perpendicular components (X, Y and Z) along the geographic co-ordinates. These quantities are related as follows:

$$H^2 = X^2 + Y^2$$
, $F^2 = H^2 + Z^2 = X^2 + Y^2 + Z^2$ (2.1)

$$Y = H \sin D$$
, $\tan I = Z/H$. (2.2)

$$Z = F \sin I = H \tan I$$
, $X = H \cos D$. (2.3)

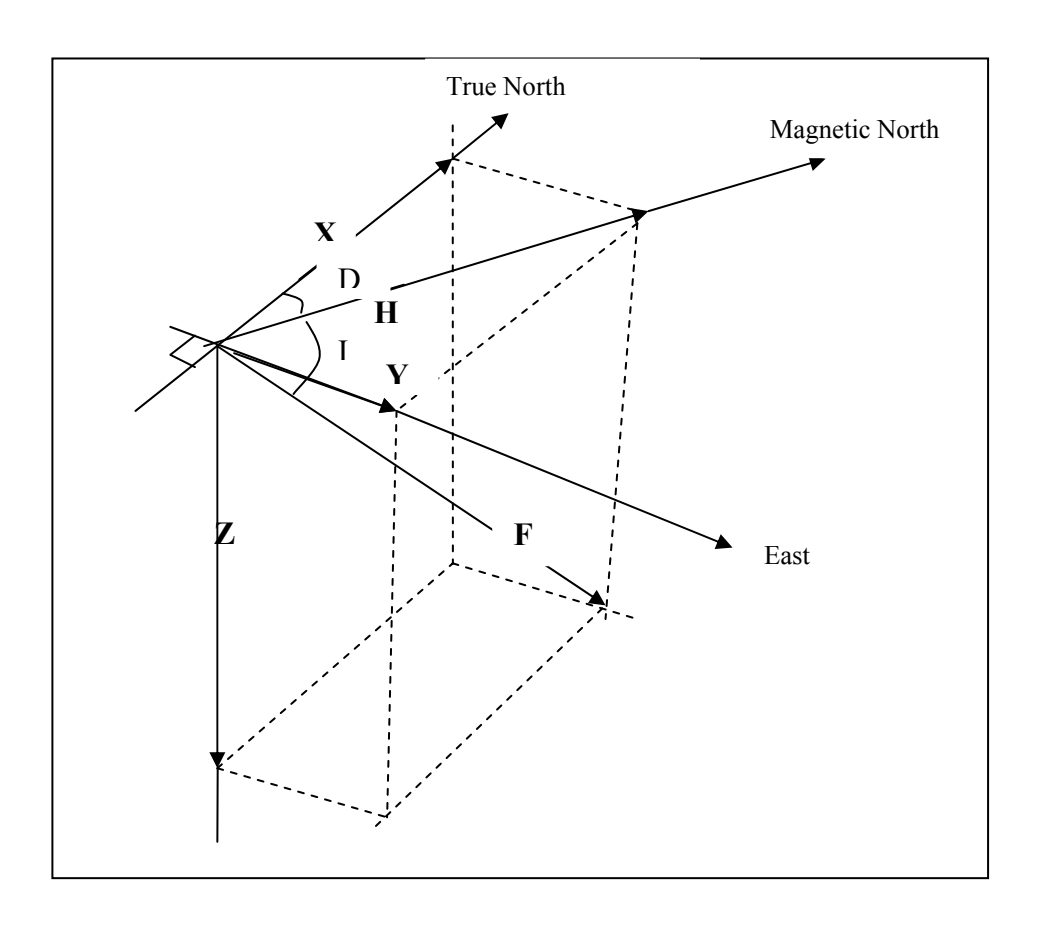


Fig. 2.2. The magnetic elements. After Reynolds (1997).

2.2.3 Variations with Time in the Earth's Magnetic Field

2.2.3.1 Secular Variations

These are slow changes in the Earth's field which take place over decades or centuries. They can be corrected using models such as the International Geomagnetic Reference Field (IGRF) which give the estimated value and the annual change of the main magnetic field of the Earth in a specific area. The IGRF is a mathematical representation of the Earth's main magnetic field due to large scale sources in the liquid conducting outer core (Dobrin and Savit, 1988). When this is removed from the data, the results are residual magnetic anomalies due to the local geology only, assuming that the core field is accurately described by the IGRF model.

2.2.3.2 Diurnal Variations

Diurnal variations are smaller but more rapid variations in the Earth's field. These are caused by the flow of charged particles from the Sun within the ionosphere towards the Earth. They have a periodicity of approximately one day. They are subject to amplitude and phase changes depending on the geographic location of the observer. These variations can also be influenced by geological conditions such as rock susceptibility at the place of observation (Dobrin and Savit, 1988). Necessary corrections are done by the continuous observation of a base station magnetometer located in or near the survey area.

The measured magnetic field in the survey area is then corrected for the observed diurnal changes at a specific time through a direct subtraction of the two data sets.

2.2.3.3 Magnetic Storms

These are rapid, unpredictable variations of large amplitude (hundreds of nT) in the magnetic field such that no corrections can be made. They are produced by sunspot and solar flare activity. Magnetic surveying has to be discontinued for hours or even days under such conditions (Milsom, 1989).

2.2.4 Magnetization of Rocks

The intensity of magnetization is the characteristic of a rock which determines its magnetic effect on the observed field. It has both magnitude and direction and depends on the rock's susceptibility and permanent magnetization (Reynolds, 1997). Magnetic anomalies are caused by magnetic minerals (mainly magnetite and pyrrhotite) contained in rocks (Telford et al., 1990). In general rocks have both induced and remanent magnetization (Reynolds, 1997).

2.2.4.1 Induced Magnetization

This is magnetization acquired in the presence of a magnetic field which disappears when the field is removed. It is in the same direction as the present day Earth's field. Induced magnetisation thus refers to the action of the field on the material wherein the ambient field is enhanced and the material itself acts as a magnet (Breiner, 1973).

2.2.4.2 Remanent Magnetization

This is permanent magnetization acquired by a rock when it cools down in the presence of a magnetic field, or by orientation of magnetic grains due to great pressure or during sedimentation. Remanent magnetization may be in any direction and may be independent of the present day Earth's field (Breiner, 1973).

2.2.5 Susceptibility of Rocks

Susceptibility is a measure of how easily a material becomes magnetized. It has no units and depends upon the alignment and shape of magnetic grains dispersed throughout the rock. Rocks that have a significant concentration of ferro- and /or ferri-magnetic minerals tend to have the highest susceptibilities. Basic and ultra-basic rocks have the highest susceptibilities. Acid igneous and metamorphic rocks have intermediate to low values, whilst sedimentary rocks have very small susceptibilities (Reynolds, 1997). Susceptibility can be expressed as the ratio of the intensity of induced magnetism to the

magnetising force (Dobrin and Savit, 1988). Equation 2.4 gives the relationship between susceptibility, magnetisation and the magnetising field.

$$\mathbf{M} = \mathbf{X}_{\mathbf{m}} \mathbf{H} \tag{2.4}$$

M is magnetisation (A m⁻¹)

X_m is magnetic susceptibility and

H is the magnetising field (A m⁻¹).

2.3 Instrumentation

The magnetic data was collected using two Scintrex Envi magnetometers on loan from the Zimbabwe School of Mines. These are proton precession magnetometers and their principle of operation is found in most geophysics textbooks including Reynolds (1997); Parasnis (1979); Telford et al. (1990) and Dobrin and Savit (1988). The instrument is a total field magnetometer and has the following characteristics:

- an operating range of 20 000 to 100 000 nT and an accuracy of +/- 0.5 nT;
- can be optionally used as a gradiometer and has a gradient tolerance of 5 000 nT/m;
- standard operating temperature range of -40° to +60°C;
- does not need any levelling, is not affected by polarity and does not have an instrument drift;
- is fully automated, i.e. it can be tuned to a suitable average ambient magnetic field value, sampling period, station and line spacing. For the

purposes of this survey a sampling rate of 2 seconds and an average ambient magnetic field value of 32 000 nT were used;

- monitors noise and reliable values have noise values between 0 and 1 nT;
- the sensors are mounted on a 2 3 m long non-magnetic aluminium staff in order to reduce the effect of very near the surface magnetic sources;
- the instrument is powered using two 12 V batteries, has a digital readout, and is very light, portable and robust. The batteries were charged overnight.

2.3.1 Field Procedures

A base station was established on Line 14E at station 225S, at relatively safe distances from all magnetic interferences such as power lines and other cultural effects such as automobiles, pipelines and wire fences. All lines were cut starting from line AD on Fig. 1.3. Before taking measurements, it was ensured that the magnetometer operator was free of magnetic materials such as belt buckles, metal buttons and metal spectacle frames. Two separate magnetometers were used: a recording base station magnetometer and the roving field unit. This allowed for direct subtraction of the diurnal variation in the Earth's field from the field data. Therefore the corrections for diurnal variations were adjusted to the same time and applied to all readings. Magnetic measurements of the total field were taken along all the 24 lines at 12.5 m station spacing so as to minimise aliasing. A sensor height of 2 m was used throughout the survey. The line spacing was 50 m and the length of these lines was restricted to the farm boundaries. Their orientation

was in a N-S direction, perpendicular to the strike of the local geology, and was determined by the use of a prismatic compass and ranching rods. At least three readings were taken at each station so as to ensure that the magnetometer was providing valid readings. The measurement was only recorded when the operator was sure of a stable reading.

2.3.2 Problems Encountered

Establishing a magnetic base station was difficult since most of the area is divided into paddocks using a wire fence and there are several power lines and telephone lines on the farm. The wire fence problem was also encountered during data collection. There is also a lot of metallic machinery on the farm especially around the cheese room. All these contributed to cultural effects. There was also a problem of locating stations since most of the wooden pegs demarcating stations that were in the paddock areas were disturbed by cattle and those in the compound areas were tampered with by farm workers. Relocation of the pegs using a measuring tape was therefore necessitated. At the beginning of the survey readings at the base station showed large fluctuations for about 1 hour before they stabilised. This indicated a magnetic storm. The survey had to be stopped until the storm was over.

Chapter 3

Induced Polarisation

3.1 Introduction

This method has been widely used in the search for base metals and disseminated sulphide ores, in contrast to other geophysical methods e.g. self potential which is mainly used in the search for massive sulphide ores (Reynolds, 1997). In this method, the artificial potentials produced by applied fields are of interest. To observe them, either transient or alternating currents must be used (Grant and West, 1965). Several arrays can be used, and these include the pole-dipole array, the Schlumberger array, the gradient array and the dipole-dipole array. The dipole-dipole array (Fig 3.1) was used in this project since it has good resolution and penetration (Sumner, 1976). The parameters in Fig. 3.1 are:

n, is a whole number equal to or greater than one;

x, is the distance between the current electrodes (C_1 and C_2) as well as between the potential electrodes (P_1 and P_2);

nx, is the distance between the inner current and potential electrodes.

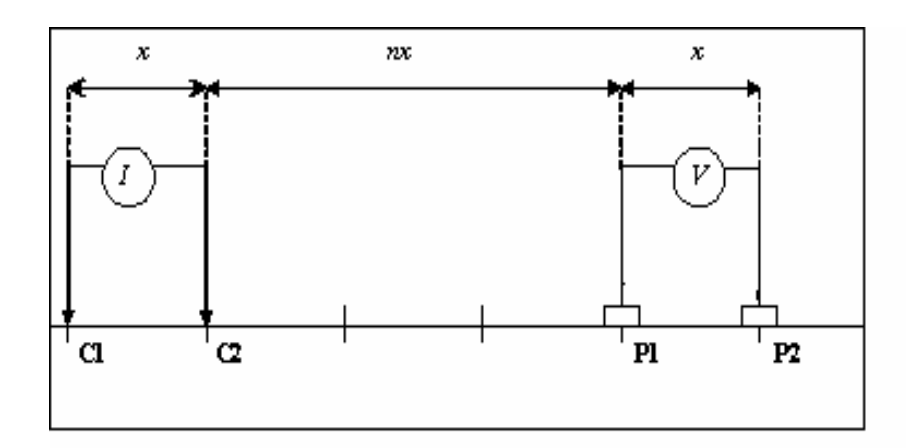


Fig. 3.1 The dipole-dipole array. I is the current source (i.e. the IP generator).

3.2 Theory

The induced polarisation method is based on a resistive blocking action or electrical polarisation in earth materials (Sumner, 1976). When an electric current passing into the earth through the ground is suddenly interrupted, a potential can be measured between nearby electrodes for some time after the current stops (Fig 3.1). The primary voltage, V_p observed between the two potential electrodes drops almost instantly to the overvoltage, V_o and then decays almost exponentially with time to zero after the interruption (Fig. 3.2). Membrane (electrolytic) and electrode polarisation are the two main mechanisms of rock polarization.

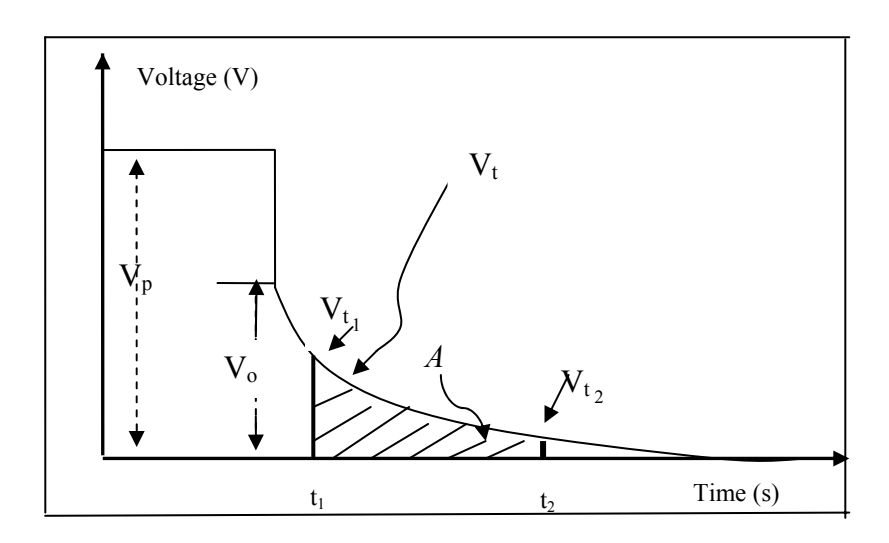


Fig. 3.2 Variation of observed voltage with time.

3.2.1 Electrode Polarization

Electrode polarization (Fig. 3.3) arises wherever electronically-conducting minerals are in contact with ground water. The degree of polarisation is determined by areas of contact between minerals and electrolytes and is independent of the mass of the mineral involved (Milsom, 1989). Current is conducted through a rock mass by the movement of ions within ground water, passing through interconnected pores or through the fractures within the rock. When an electronically conducting grain (e.g. a metal sulphide) blocks a flow channel, charge builds up opposing current flow and the grain becomes polarised, thereby creating a potential difference across the grain. On switching off the applied voltage, the ions diffuse back through the electrolytic medium and the potential difference across the grain reduces to zero in a finite time, giving the characteristic overvoltage decay measured in time domain (Reynolds, 1997).

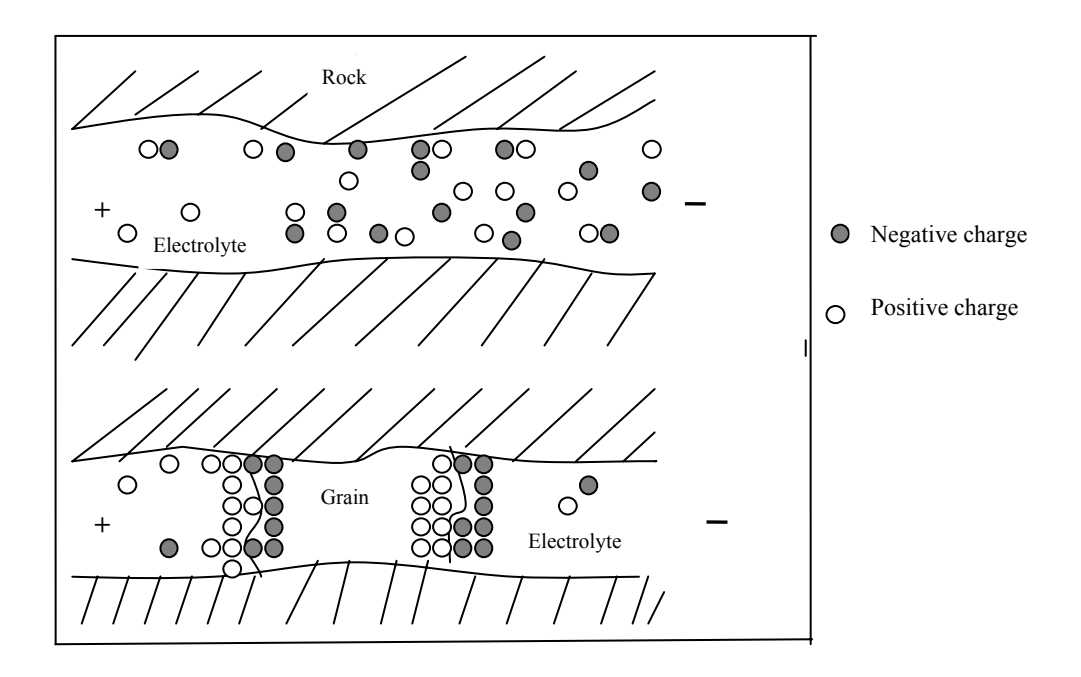


Fig. 3.3. Electrode polarization. There is electric flow in the upper channel and electrode polarization in the lower channel. After Reynolds (1997).

3.2.2 Membrane Polarization

Membrane polarisation can be present in the absence of current flow when negative charges in clays or on cleavage surfaces or edges of layered and fibrous minerals attract a diffuse cloud of positive ions. These mobile ions can block pore passages and will migrate and accumulate in the presence of an electric field (Fig. 3.4). The capillary pores of a rock also appear to sort electrolyte ions according to size and charge, some rocks behaving like an ion diffusion membrane. Membrane polarisation is found under conditions where there is variation in ion mobility causing a pile up of charge at

boundaries between regions where ion mobility varies. The ion concentration gradients thus developed oppose current flow and cause a polarising effect (Sumner, 1976).

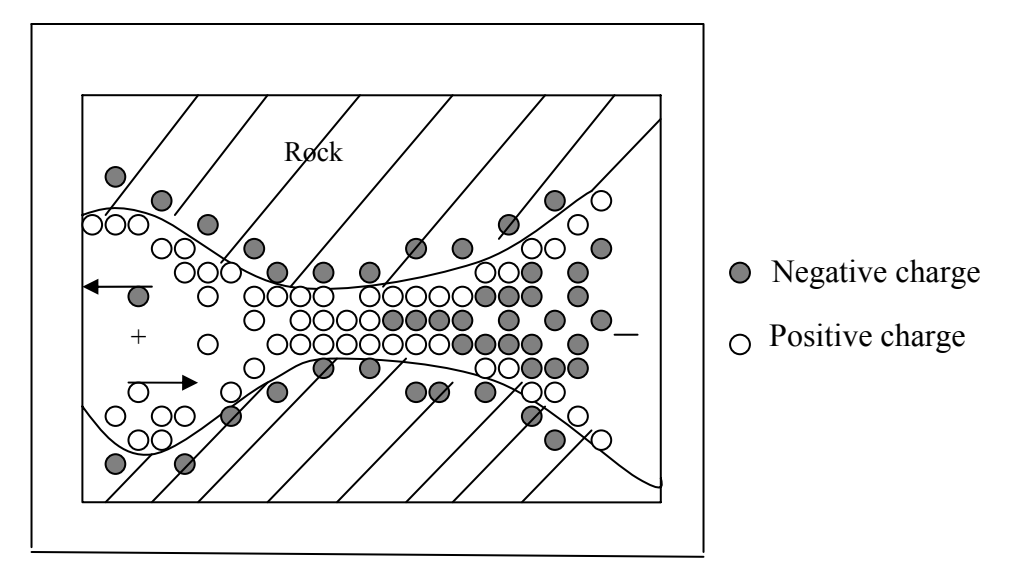


Fig. 3.4 Membrane polarisation associated with a constriction within a channel, between mineral grains. After Reynolds (1997).

3.2.3 Chargeability

Chargeability in terms of Fig. 3.2, is defined as the ratio of V_t to V_p . It has units of millivolts per volt (mV/V). The V_t/V_p ratio cannot be measured directly since electromagnetic transients are dominant in the first tenth of a second. Time domain chargeability is thus defined in terms of the decay curve at a later time, as the area A beneath the decay curve over a certain time interval $(t_1 - t_2)$ normalised by the steady state potential difference, V_p (Milsom, 1989). The area A is determined within the measuring apparatus by analogue integration.

$$M = \frac{A}{V_p} = \int_{t_1}^{t_2} \frac{V_t}{V_P} dt$$
 3.1

The units are seconds or milliseconds.

Measurements can be done in the time or frequency domain. Only time domain is discussed here since it was the one applied. Theory on the frequency domain can be found in many geophysical textbooks including Reynolds (1997), Milsom (1989) and Parasnis (1986).

3.2.4 Resistivity

The apparent resistivity for any four electrode array (Fig. 3.1) is given by

$$\rho_a = \frac{2\pi\Delta V}{IG} \tag{3.2}$$

where G =
$$\frac{1}{C_1 P_1} - \frac{1}{C_1 P_2} - \frac{1}{C_2 P_1} + \frac{1}{C_2 P_2}$$
 3.3

 ΔV is the potential difference between the potential electrodes, I is the current flowing between the current electrodes and G is a geometric factor (Parasnis, 1986). For the dipole-dipole array, the apparent resistivity is given by

$$\rho_a = \pi n(n+1)(n+2)x\frac{\Delta V}{I}.$$
3.4

and it can be calculated from field measurements. Its units are Ω m.

3.2.5 Negative IP and Masking

Negative IP effects can be caused by power lines or telephone cables. They can also arise from lateral inhomogeneities. Layering can also produce negative values or mask deeper sources more readily if both the surface and target layers are more conductive than the rocks in between (Milsom, 1989). When polarisable minerals lie in the same plane of the array or near the surveying electrodes, peculiar IP effects are encountered, particularly negative IP effects, which complicate the interpretation of subsurface data (Sumner, 1976).

3.3 Instrumentation

The equipment used consisted of:

- an IPC-7/2.5 kW transmitter unit designed for time domain induced polarization or automatic commutated D.C. resistivity. This had a maximum output current of 10 A and output voltage of 1210 V D.C., an automated cycle timing, polarity change and switch selectable pulse duration which was set at 2 seconds. It had an operating temperature range of -30 to +55 °C;
- a 2.5 kW single phase, motor-generator which was used as the power source for the IPC -7 transmitter. The motor was a four stroke, 8 hp Briggs & Stratton model. A voltage of 110 V was used;
- potential and current electrodes and wire cables and

• a dummy load which was mounted on the cover of the console. Its purpose is to take the load going into the transformer during the time that the transmitter is in the off position of the cycle. This balances the load on the motor so that it will run smoothly. The dummy load has a maximum capacity of 2.5 kW A.C.

3.3.1 Field Procedures

The dipole-dipole array, Fig. 3.1, was used on all the 24 lines in this survey because it has got a good resolution. This is sometimes known as the reciprocal array because it gives the same results if the current electrodes (C1 and C2) and potential electrodes (P1 and P2) are interchanged. Porous pots were used as potential electrodes. These were filled with concentrated copper sulphate solution, a strong electrolyte, so as to facilitate easy flow of current and good contact between the electrodes and the ground. Small holes were dug in the ground and moistened with salty water (in order to provide good electrical contact with the ground), before the potential electrodes were placed in them. The distance between the current and potential electrodes, x, was set at 25 m so as to get a better resolution of sub-surface bodies. Six investigation depths (i.e. n = 1 up to n = 6) were probed so as to locate both shallow and deeper sources.

3.3.2 Precautions

Each time before starting the survey, it was ensured the transmitter console was well grounded. It was also ensured that there was good voice communication between all members of the crew through the use of portable radios. The high voltage toggle switch on the transmitter was switched off each time the high voltage selection switch or the primary voltage multiplier switch was moved so as to avoid high voltage discharge. Current and voltage cables were laid parallel to each other, at least 1 m apart to avoid electromagnetic induction effects.

3.3.3 Problems Encountered

As mentioned before, some of the wooden station pegs especially in the paddock areas were disturbed by cattle. If unmonitored, sometimes the cattle chewed the cables, thereby creating open circuits. Also, people passing by and children playing disturbed cables and some removed lids of the porous pots that were used as potential electrodes. Shortage of manpower was another major setback.

Chapter 4

Magnetics Data Processing, Presentation and Results

4.1 Data Processing and Presentation

4.1.1 Introduction

Apart from the removal of diurnal effects, the reductions required for magnetic data are insignificant. The vertical gradient varies from approximately 0.03 nT/m at the poles, to 0.01 nT/m at the magnetic equator. The latitude variation is rarely greater than 6 nT/km. Thus elevation and latitude corrections are generally unnecessary (Telford et al., 1990).

The Earth's magnetic field is dipolar, which means that a single anomaly can have the form of a positive peak only, a negative peak only, or a doublet consisting of both positive and negative peaks (Reynolds, 1997).

4.1.2 Magnetic Signatures of Rocks, Structures and Ore Environments

A magnetic signature is a complex combination of magnetic responses. Some explanations of the magnetic signatures used in qualitative interpretation are summarised in Table 4.1. Segments of a profile map (Fig. 4.1) with little variation are termed magnetically quiet and are associated with rocks with low susceptibilities. Segments showing considerable variation are called magnetically noisy and indicate magnetic sources in the subsurface. The relative amplitude of any magnetic anomaly (both positive and negative) and the local magnetic gradients can help to provide an indication of the subsurface (Reynolds, 1997). In general, the amplitude of an anomaly is related to the strength of magnetisation and depth of the source. Shallow sources give short wavelength anomalies (e.g. ~ 100 m) and deeper sources give long wavelength anomalies (e.g. ~ 500 m).

Table 4.1 Magnetic signatures. After Reynolds (1997).

Applies	Magnetic character	Possible cause
to:		
Segments	Magnetically quiet	Low susceptibility rocks.
of a	Magnetically noisy	High susceptibility rocks, near surface.
profile		
Anomaly	Wavelength	Short – near surface feature.
		Long – deep seated feature.
	+/- Amplitude	Indicative of intensity of magnetisation.
Profile	Anomaly structure and	Indicates possible dip and dip direction.
	shape	Induced magnetisation caused by positive to north and negative
		to south in southern hemisphere otherwise it implies remanent
		magnetisation.
Maps	Linearity in anomaly	Indicates possible strike of magnetic feature.
Maps	Dislocation of contours	Lateral offset by fault.
Maps	Broadening of contour	Downthrow of magnetic rocks.
	interval	

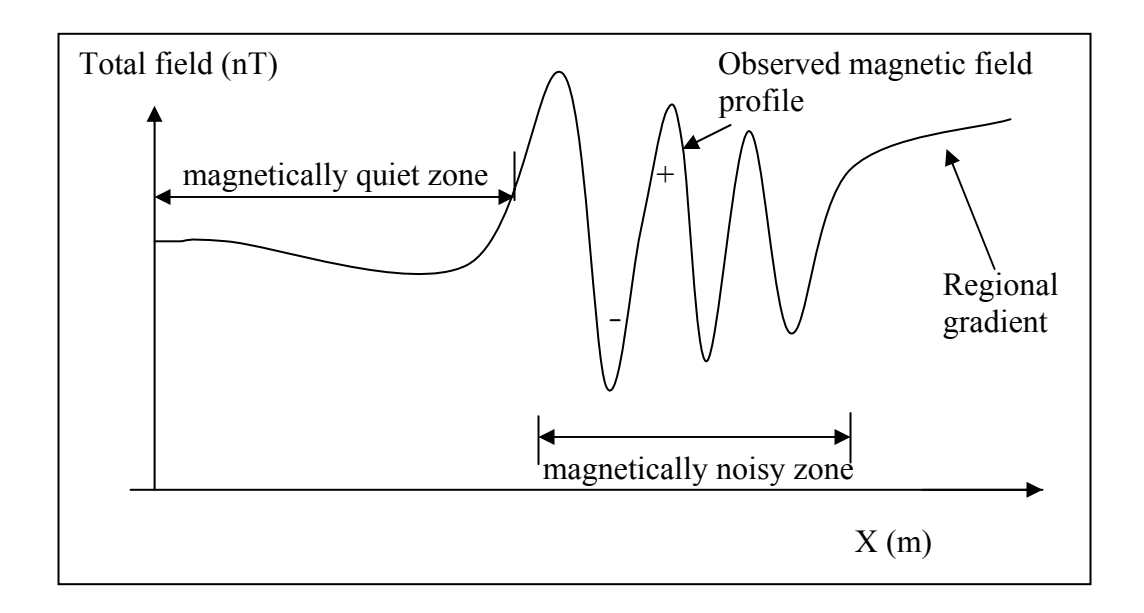


Fig. 4.1 The regional gradient, magnetically quiet zone and magnetically noisy zone. After Reynolds (1997).

4.1.3 Depth Estimations

The depth to a magnetic body can be estimated from a magnetic profile using the shape of the anomaly. Slope methods have been widely used especially for aeromagnetic interpretation. In Fig 4.2, S is the horizontal extent of the portion of the curve that is nearly linear at the maximum slope. Two additional line segments can be drawn as tangents to the profile at half the maximum slope; the horizontal distance between the points of tangency is P. The depth of the source, h, beneath these portions of the curve is given by:

$$h = k_1 S$$
 1.67 $\leq k_1 \leq 2.00$ (generally $k_1 \sim 1.82$).....(4.1)

$$h = k_2 P$$
 (generally $k_2 \sim 0.63$).....(4.2)

The empirical factors k_1 and k_2 will vary for different shapes of sources, e.g. sphere, cylinder, dyke, dipping dyke, etc. This method is much simpler and faster and provides more depth estimates than analysis by model fitting (Telford et al., 1990). It produces more depth estimates in the sense that it can be carried out on original field profiles and so there is no need to wait for map preparation. Peter's half slope method assumes the horizontal distance between half maximum slopes to be equal to 1.6*S*. Other methods of estimating depth include the use of the step model and the ribbon model, and they are explained in geophysical textbooks including Grant and West (1965), Parasnis (1986) and Telford et al. (1990). There is also the Parasnis method of determining the depth to the top of a thin sheet, which is fully explained in Parasnis (1986).

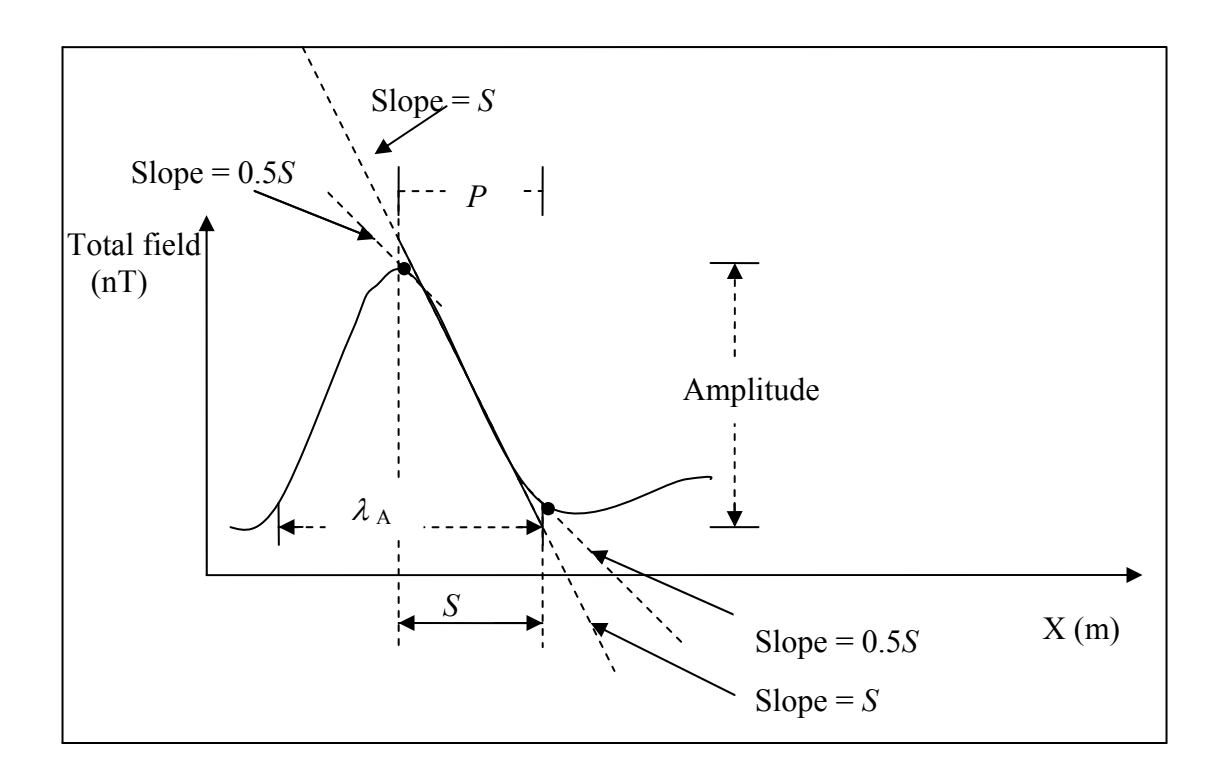


Fig. 4.2 Depth estimation using the straight slope method. After Telford et al. (1990).

The energy/power spectrum map can also be used to estimate the average depths to the deep and shallow sources. Its use is explained in section 4.1.5.4 below.

4.1.4 Diurnal Corrections

Drift curves for all the 24 lines were drawn manually on graph paper (using raw base station data) to correct for the time variations. The variation of base station readings with time for the two days in which the magnetic survey was completed is shown in Fig. 4.3 and Fig. 4.4 below. On the first day (Fig. 4.3) field data was collected between 14:40 and 16:15 hours after the magnetic storm (Fig. B-25) that was experienced during the first hour of the survey had subsided. Field data was only collected between 10:00 and 17:00 hours on the second day (Fig. 4.4). Fig. 4.3 shows that the base station readings are oscillating and Fig. 4.4 is showing an oscillating and downward trend in the readings. The diurnal variation on Fig. 4.3 ranges from 1 nT to 8 nT in amplitude and that on Fig. 4.4 ranges between 1 nT and 10 nT. These curves were used to correct the total field readings for diurnal variations. All the measured magnetic field data of the roving magnetometer were corrected for the diurnal changes observed at the base station.

.

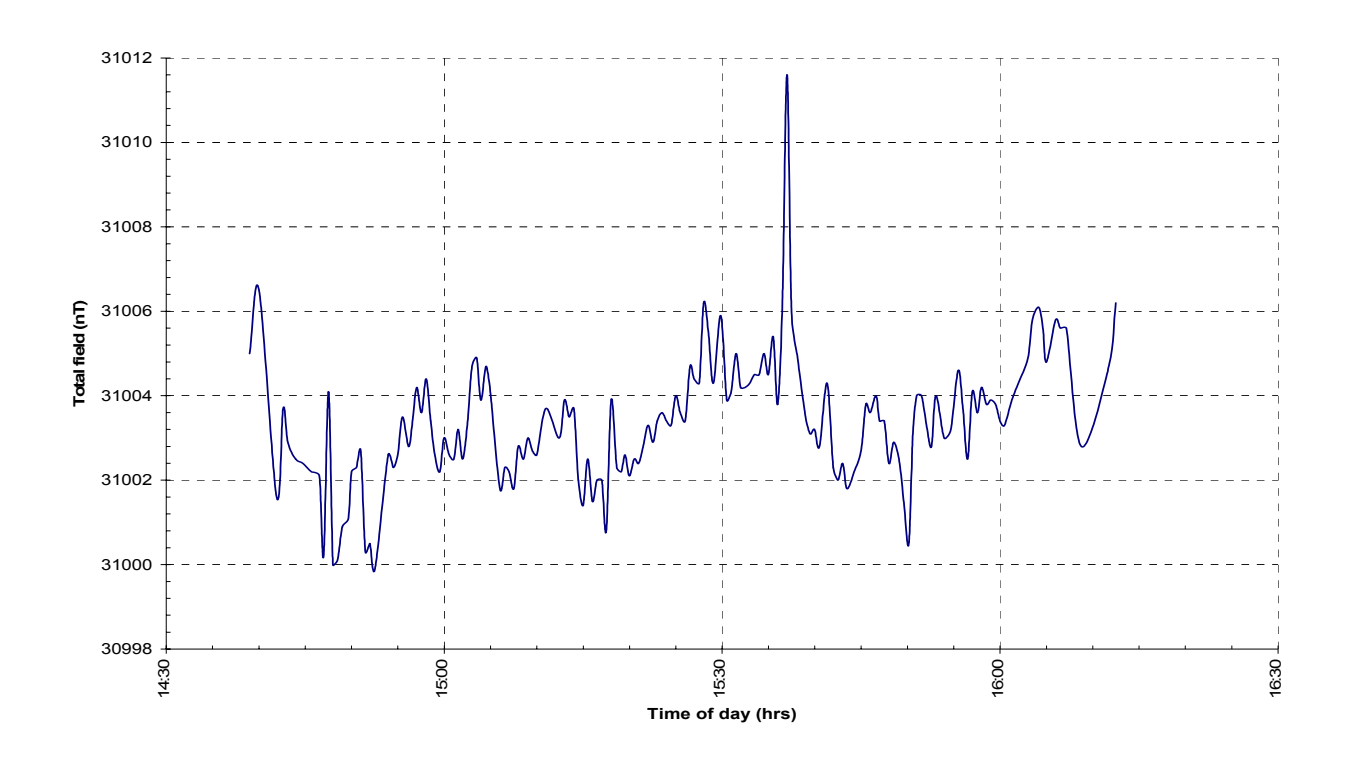


Fig. 4.3 Variation of base station readings with time for day 1 (27 June 2006).

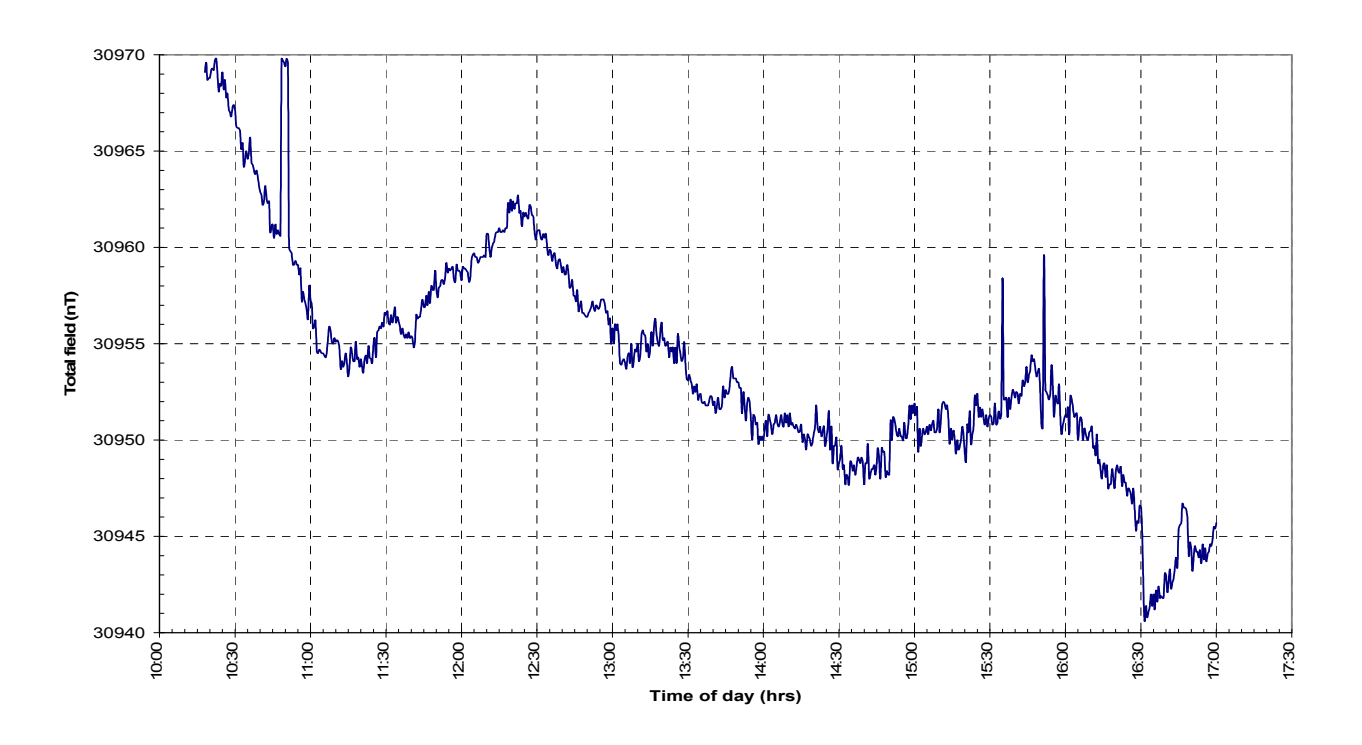


Fig. 4.4 Variation of base station readings with time for day 2 (28 June 2006).

4.1.5 Magnetic Maps

All the magnetic maps were produced using Geosoft software. The magnetic data were entered in an XYZ file, edited and reduced using the MAPPING AND PROCESSING system of the software. Bi-directional gridding was done to the magnetic data, at a cell size of 12.5 m. This is a process of interpolating the line data to establish values at the nodes of a regularly spaced grid prior to contouring.

4.1.5.1 The Magnetic Profile Map

A profile map (i.e a collection of profiles for all the lines on the surveyed grid) is the simplest way of presenting magnetic results, which helps to identify zones with different magnetic characteristics. The advantages of a magnetic profile map are:

- it shows all the recorded information without distortion or omission on the map sheet,
- it does not suffer aliasing which can occur when profile data is re-sampled to produce a contour map and
- the human eye can easily pick trends on such a map.

The techniques which are used to get important information of the sub-surface, e.g. depth to the causative body, from a magnetic profile which are explained in sections 4.1.2 and 4.1.3 above could then be applied.

4.1.5.2 The Reduction to the Pole Map

Reduction to the pole assumes that there is no remanent magnetisation. Purely induced anomalies are centred over the causative bodies at the magnetic pole. Away from the magnetic pole, this is not true as the anomalies have positive and negative lobes, therefore it is necessary to reduce the magnetic data to the pole. Reduction to the pole shifts the anomalies laterally to be located over their respective sources and alters their shape so that symmetrical sources cause symmetrical anomalies (Blakely, 1996).

4.1.5.3 The Analytic Signal Map

The so-called analytic signal is formed from a combination of the horizontal and vertical gradients of a magnetic anomaly. It is calculated using the formula:

$$|A(x,y)| = \sqrt{\left[\left(\frac{\partial F}{\partial x}\right)^2 + \left(\frac{\partial F}{\partial y}\right)^2 + \left(\frac{\partial F}{\partial z}\right)^2\right]}$$
(4.1)

where A is the analytic signal function, F is the total field, and the three gradients are: $\frac{\partial F}{\partial x}$, $\frac{\partial F}{\partial y}$ and $\frac{\partial F}{\partial z}$. The three gradients were calculated from total field point values using the Geosoft Mapping and Processing system. The program then combines them through Boolean operations to give the analytic signal. The advantage of constructing an analytic

signal map is that the analytic signal function is independent of the direction of magnetisation, the geological dip and the direction of the Earth's field but is dependent on the location of causative bodies. The peaks of analytic signal functions are symmetrical and occur directly over the edges of wide bodies and directly over the centres of narrow bodies, thus indicating the magnetic source geometry (Milligan and Gunn, 1997).

4.1.5.4 The Power Spectrum Map

The power spectrum depends on a 2-D spectral analysis of a given magnetic map. It is a radially averaged plot of $\ln E$ (energy) versus γ (the radial wavenumber). Its physical basis is that the magnetic map represents the effect of a group of magnetic sources. Each magnetic source at a given depth gives rise to a magnetic response whose shape can be described by an amplitude (A) and a wavelength (λ). A magnetic anomaly map can thus be considered as a summation of different wavelengths due to sources at different depths.

 α and β are horizontal wavenumbers in cycles per unit length. λ_x and λ_y are wavelengths in the x and y directions respectively.

spectrum map as illustrated in Fig. 4.5.

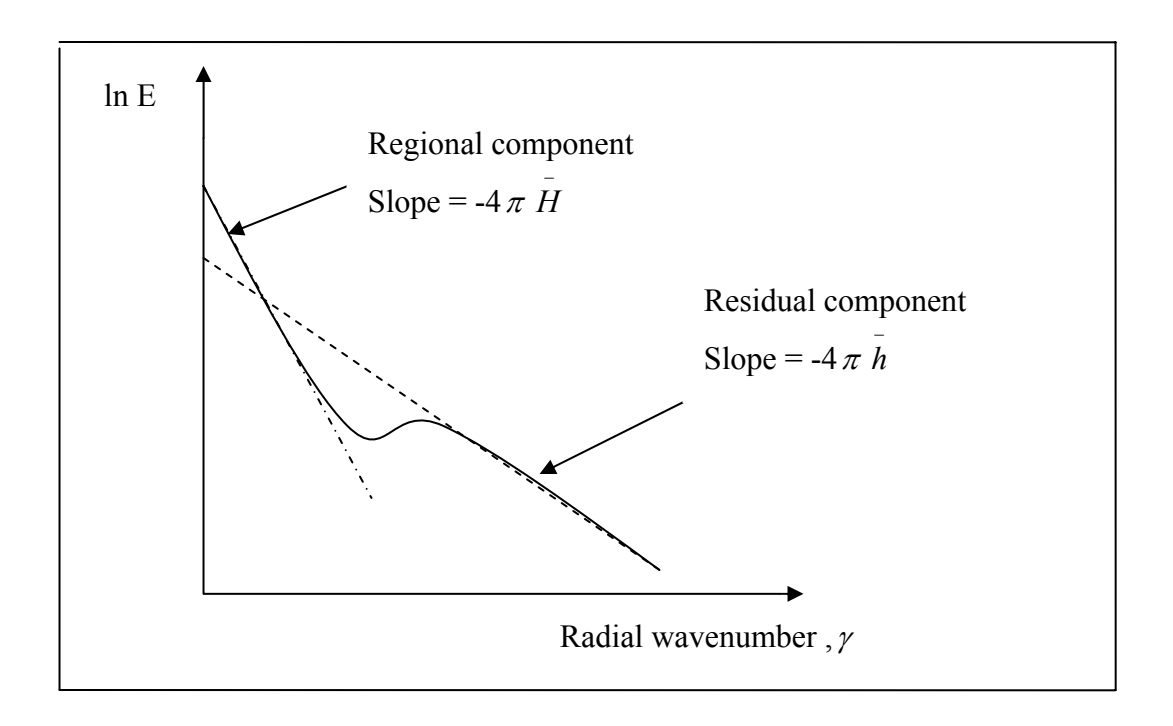


Fig. 4.5 Depth estimation using a radially averaged power spectrum.

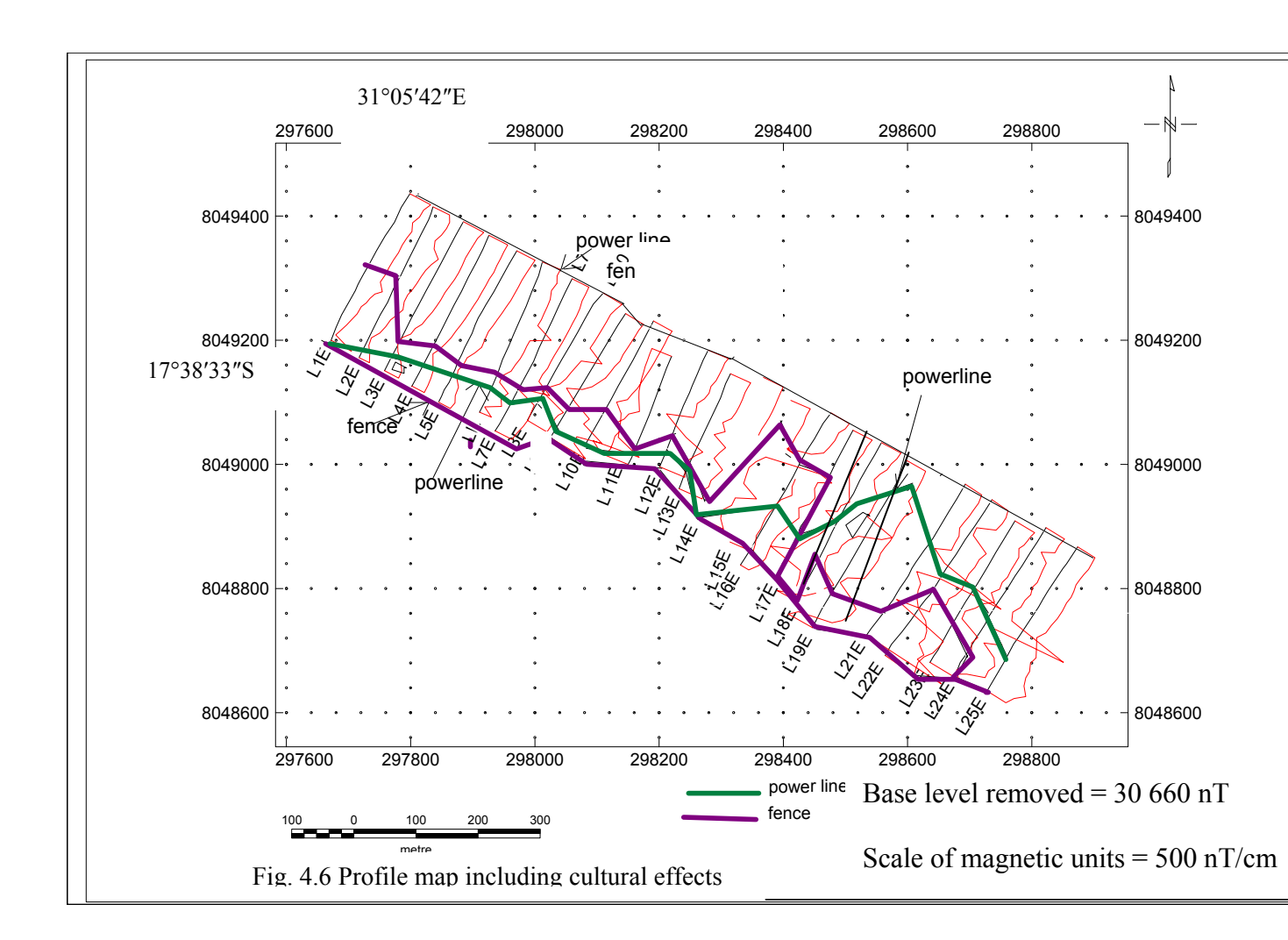
4.2 Results

The field data is in Appendix A. This survey covered the whole farm. Readings were not taken for Line 20E since this line passed through a lot of obstructions such as a farm compound, paddock and the main house. The length of the lines was restricted to the farm boundaries and therefore ranged between 225 m and 325 m. These lines are not parallel because the rugged terrain obscured the ranging (sighting) rods especially in areas around the conical hill. The results of the magnetic storm encountered on the first day of the survey are presented in Fig. B-25 in Appendix B. The figure shows that with

respect to the first reading of 25 572.5 nT, there are fluctuations ranging from +461 nT and -6 837 nT.

4.2.1 The Magnetic Profile Map

All the profiles for the surveyed grid are in Appendix B. A profile map of the total field is shown in Fig 4.6. The profiles show a magnetically anomalous area having a pronounced NW – SE trend between stations 100S and 250S on the majority of the lines. Using the slope method, whose calculations are as explained in section 4.1.3 above, the profiles for Lines 11E, 13E, and 16E give a depth to the anomalous body as approximately 10 m. On Line 18E the depth to the anomalous body is estimated to be 24 m. Both Lines 21E and 25E give a depth to the body of approximately 9 m. Amplitudes of the anomaly ranged from 80 nT to 4 200 nT. Peaks on most of the profiles are not coinciding with the power lines and the fences except for the peaks on Lines 6E, 7E, 8E and 24E as shown in Appendix B. Hence there is no obvious correlation between the magnetic highs and fences or power lines. Power lines carry AC and they cause a magnetic field that reverses 50 times a second, which affects the magnetometer because it is alternating. Therefore the magnetometer will not give a steady and repeatable reading. However since there is no obvious correlation between the magnetic highs and fences or power lines the anomalies cannot be attributed to these cultural effects but to other causes such as magnetite.

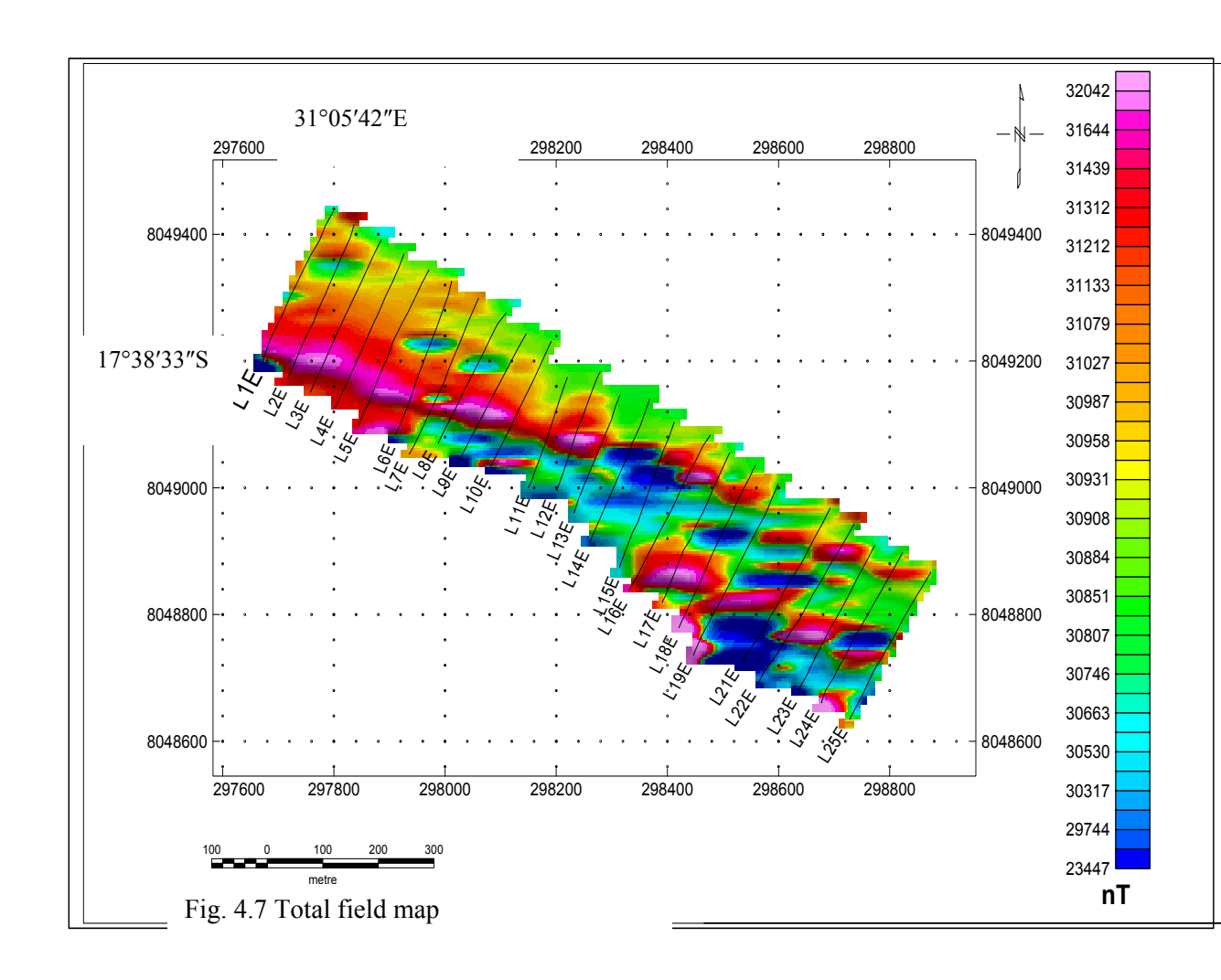


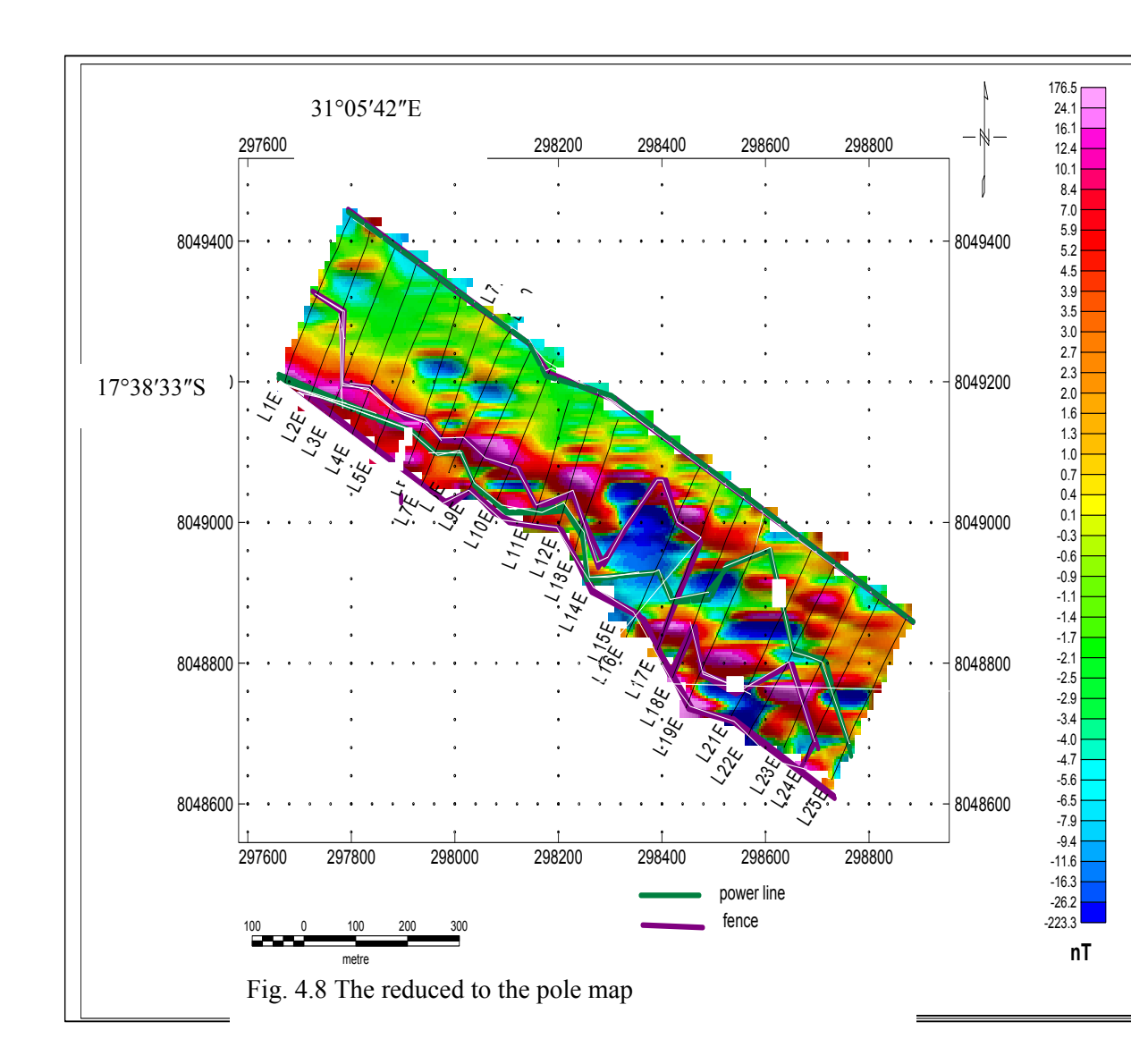
4.2.2 The Total Field Magnetic Anomaly Map

On the total field map (Fig 4.7) there are two magnetic high trends. The first magnetic high trend is in the north western part, trending WNW - ESE, starting from Line 1E and stretching up to Line 18E. The second trend is also in a WNW - ESE direction and is stretching between Lines 16E (station 125S) up to Line 23E (station 100S). There is a magnetic low trend starting from the middle up to the eastern end of the survey area.

4.2.3 The Reduced to the Pole Map

Using Geosoft software the total field map was reduced to the pole using a declination, D = -11.5° and an inclination $I = -60^{\circ}$ (Fig. 4.8). On this map, the magnetic high and magnetic low anomalies are clearly separated and anomalies are centred directly above the causative bodies (as if the area is at the North pole). The anomaly on Line 22E between stations 100S and 150S is now clear and two small patches of magnetic highs can be seen to its west between Lines 19E and 21E, which were not seen on the total field map. The magnetic high anomaly on Line 12E is found to be stretching up to Line 13E on the reduced to the pole map. A small magnetic high anomaly that was not visible on the total field map can now be identified between Lines 16E and 17E. In addition, a cluster of small magnetic high anomalies which were not seen on the total field map is shown to exist between the end of Lines 8E and 11E.





4.2.4 The Power Spectrum Map

Depth estimates for the anomalous zones in the survey area were made from the power spectrum map (Fig 4.9) and the depths to the deep sources and to the shallow sources were estimated to be 32 +/- 2 m and 8 +/- 1 m respectively. These estimations apply to the whole surveyed grid.

4.2.5 The Analytic Signal Map

The analytic signal map (Fig. 4.10) clearly outlines the symmetry of the causative bodies. On this map the causative bodies are outlined as globular clusters, with a similar trend to that shown on the total field map (Fig. 4.7).

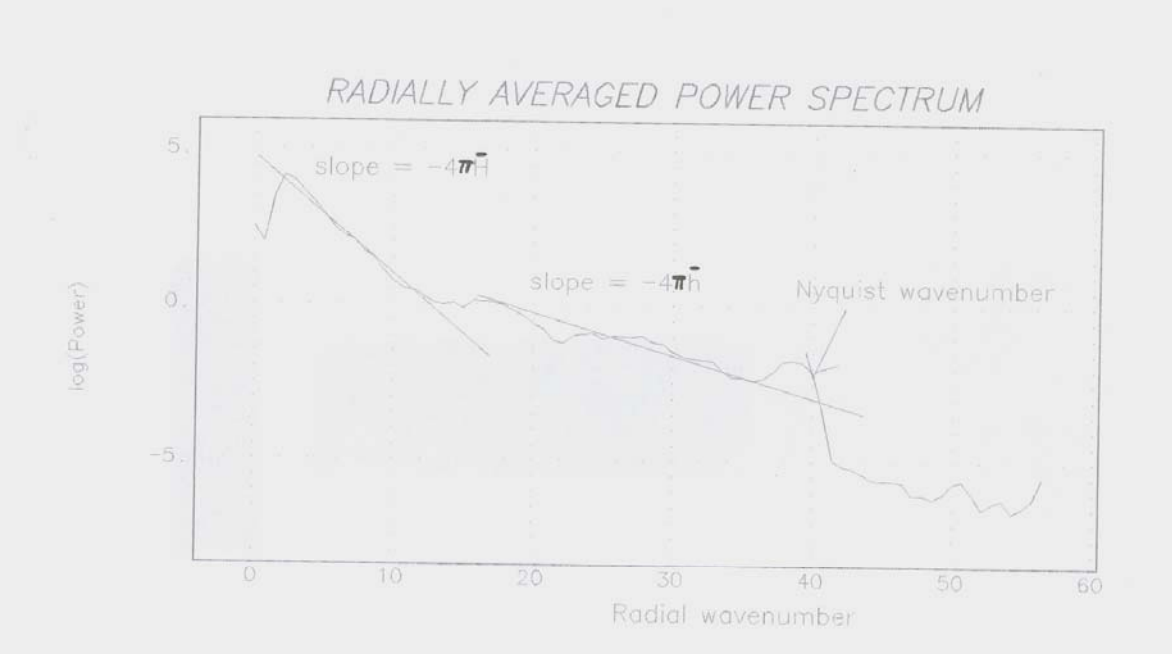
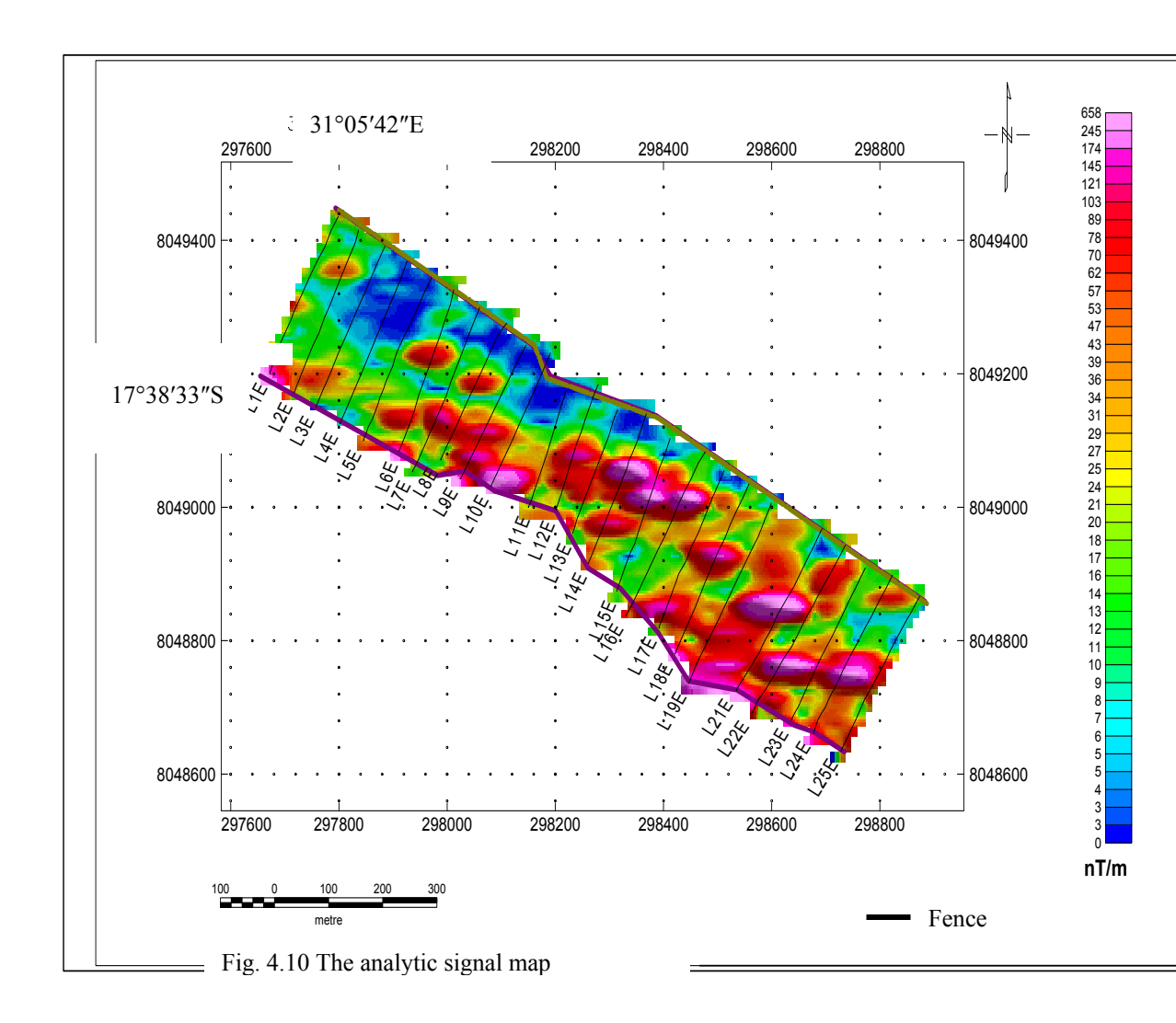


Fig. 4.9 The power spectrum map



Chapter 5

Induced Polarisation Data Processing,

Presentation and Results

5.1 Data Processing

The IP field data is given in Appendix C. Processing of all the IP data for the 24 lines was done using Geosoft Oasis Montaj43 software. Geosoft software is able to create and store an XYZ file for the data and reduce it once it is entered properly. The software was used to produce all the contour maps and pseudosections for the chargeability and resistivity values.

5.2 Data Presentation: Pseudosections

A pseudosection conveys the variation of some parameter e.g. resistivity, with location and penetration depth (Sheriff, 1984). A diagram obtained in this manner is qualitatively regarded as representing an 'electrical vertical section'. Quantitative estimates of depth and dip are extremely difficult to make from IP anomalies since the chargeability of the medium depends upon the distribution of the mineral particles (Parasnis, 1986). Depth of investigation for a dipole-dipole array is roughly given by (n + 1) x/2 (Bertin, 1976).

For the dipole-dipole electrode configuration, the data are plotted at the intersections of 45° diagonals from the centres of the dipoles (Fig. 5.1). The depth of investigation increases with an increase in the value of n (Fig. 3.1) and/or x, where x is the distance between the current and the potential electrodes.

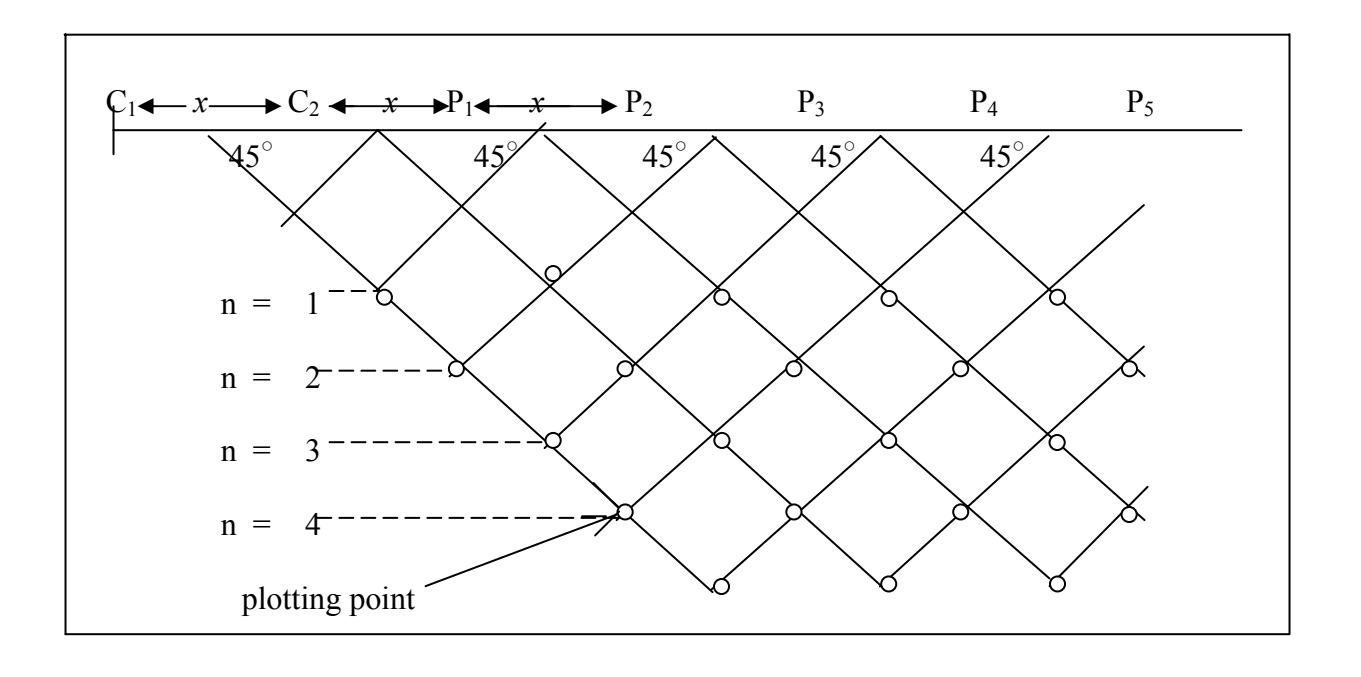


Fig. 5.1 Pseudosection plot for a dipole-dipole array.

5.3 Results

5.3.1 Introduction

Resistivity data are more closely related to the subsurface geology, including porosity, fracturing, structure and rock type than are the chargeability data. The IP data give a representation of the distribution of metallic mineralization in the subsurface while resistivity pseudosections can give the thickness of overburden or depth of oxidation (Sumner, 1976). Most potentially mineralized areas have lateral variations in subsurface electrical properties and these are displayed on the plotted IP pseudosections.

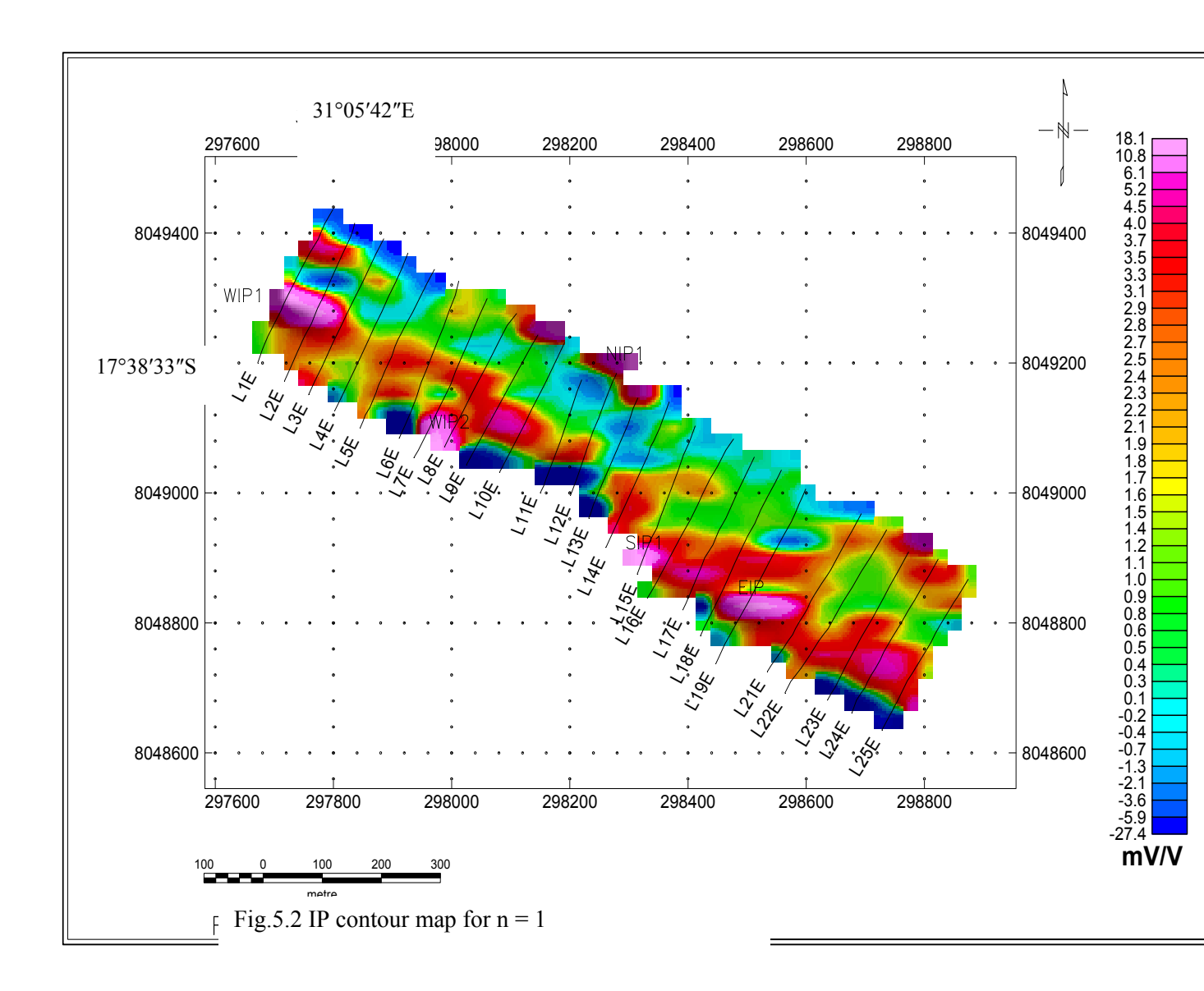
In this report the units of chargeability are quoted in mV/V and those of resistivity are quoted in Ω m. The chargeability values obtained ranged between -17 and +30 mV/V. Resistivity values ranged between 3 and 7163 Ω m. Since the lines were very short, it was difficult to establish the background values. However, chargeabilities below 2.5 mV/V and resistivities below 80 Ω m were taken as background values.

Negative IP values were found on almost all the lines, except on Lines 1E, 14E and 25E. When polarisable minerals lie in the same plane of the array or near the surveying electrodes, peculiar IP effects are encountered, particularly negative IP effects, which complicate the interpretation of the subsurface data (Sumner, 1976).

5.3.2 Contour Maps

Chargeability values (whose calculations are explained in section 3.2.3) for the different depths of investigation were plotted and contoured on a grid map of the study area (Figs. 5.2 - 5.7). Contour maps are a useful tool in delineating anomalies. Resistivity contour maps were not plotted in this case although they are a useful tool during interpretation.

The contour map for n = 1 (Fig. 5.2) shows a highly chargeable zone in the west of the survey area stretching across Line 1E up to Line 3E, located between stations 112.5S and 212.5S. This anomaly trends almost E-W and is referred to as the Western IP anomaly 1 (WIP1). A second highly chargeable zone stretches across Lines 7E and 8E, near the

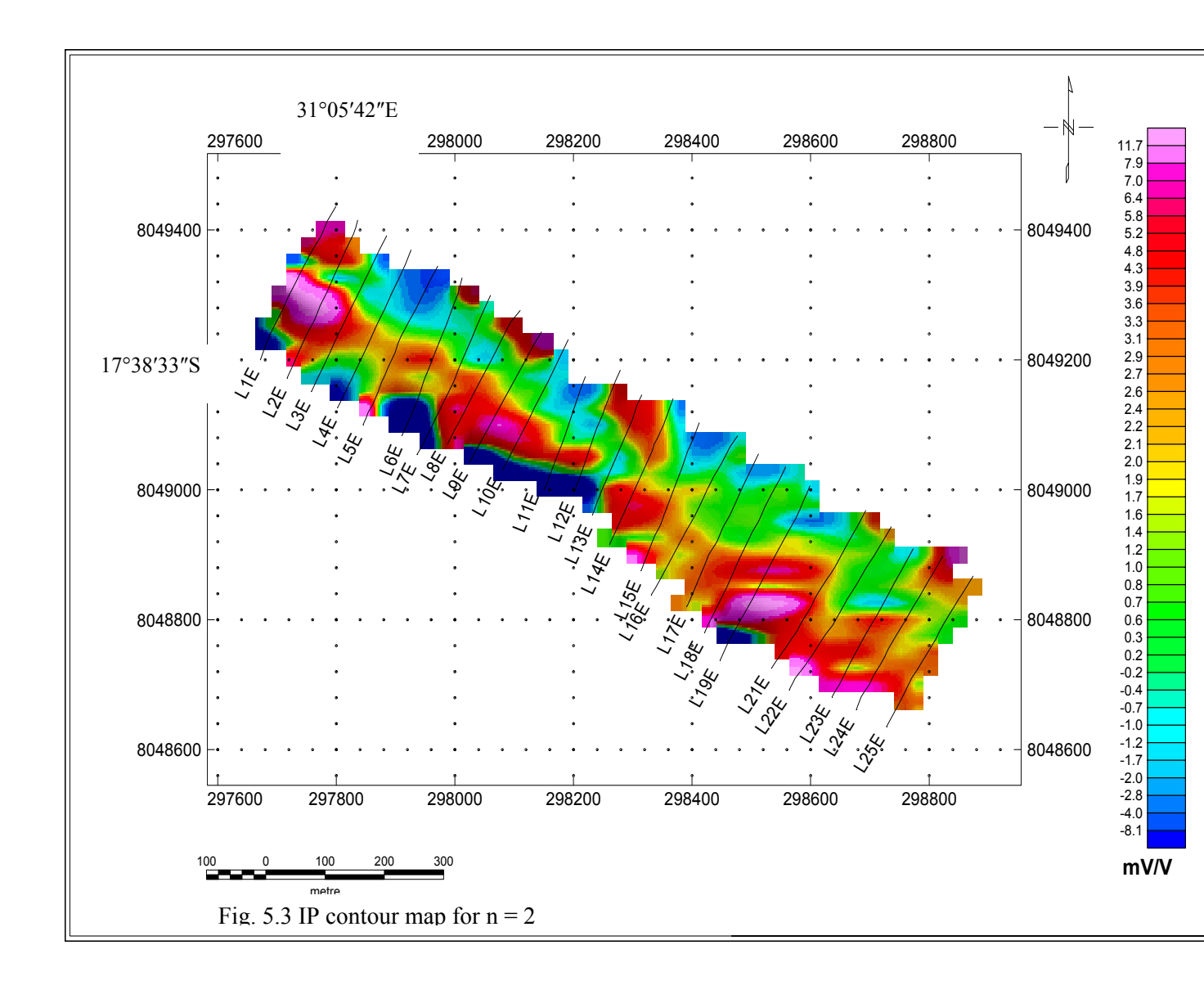


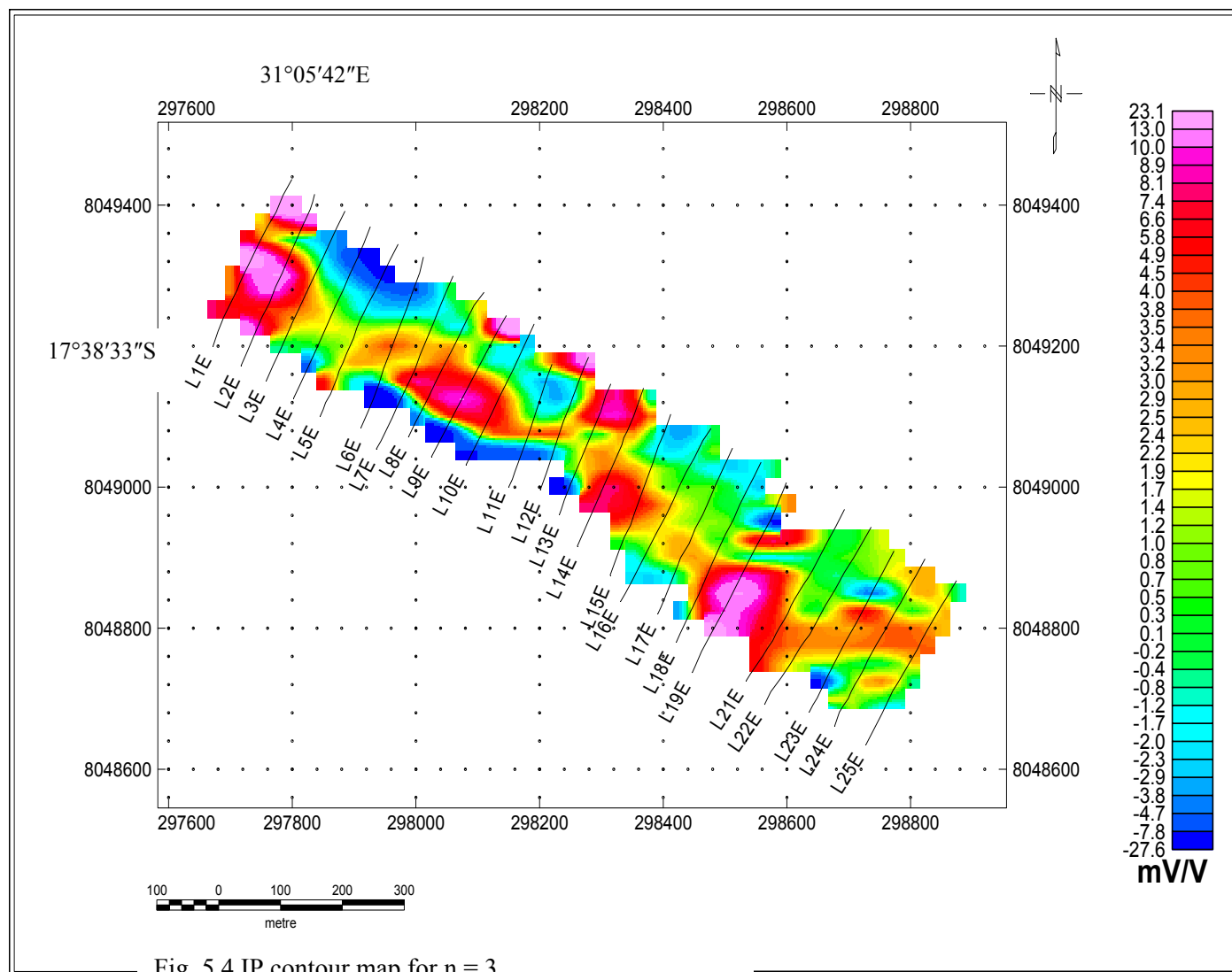
southern end of the lines. This anomalous zone is referred to as the Western IP anomaly 2 (WIP2). Towards the southern end of Line 15E there exists a small chargeable patch referred to as the Southern IP anomaly 1 (SIP1). A fourth chargeable zone appears between Lines 18E and 21E and it is referred to as the Eastern IP anomaly (EIP1).

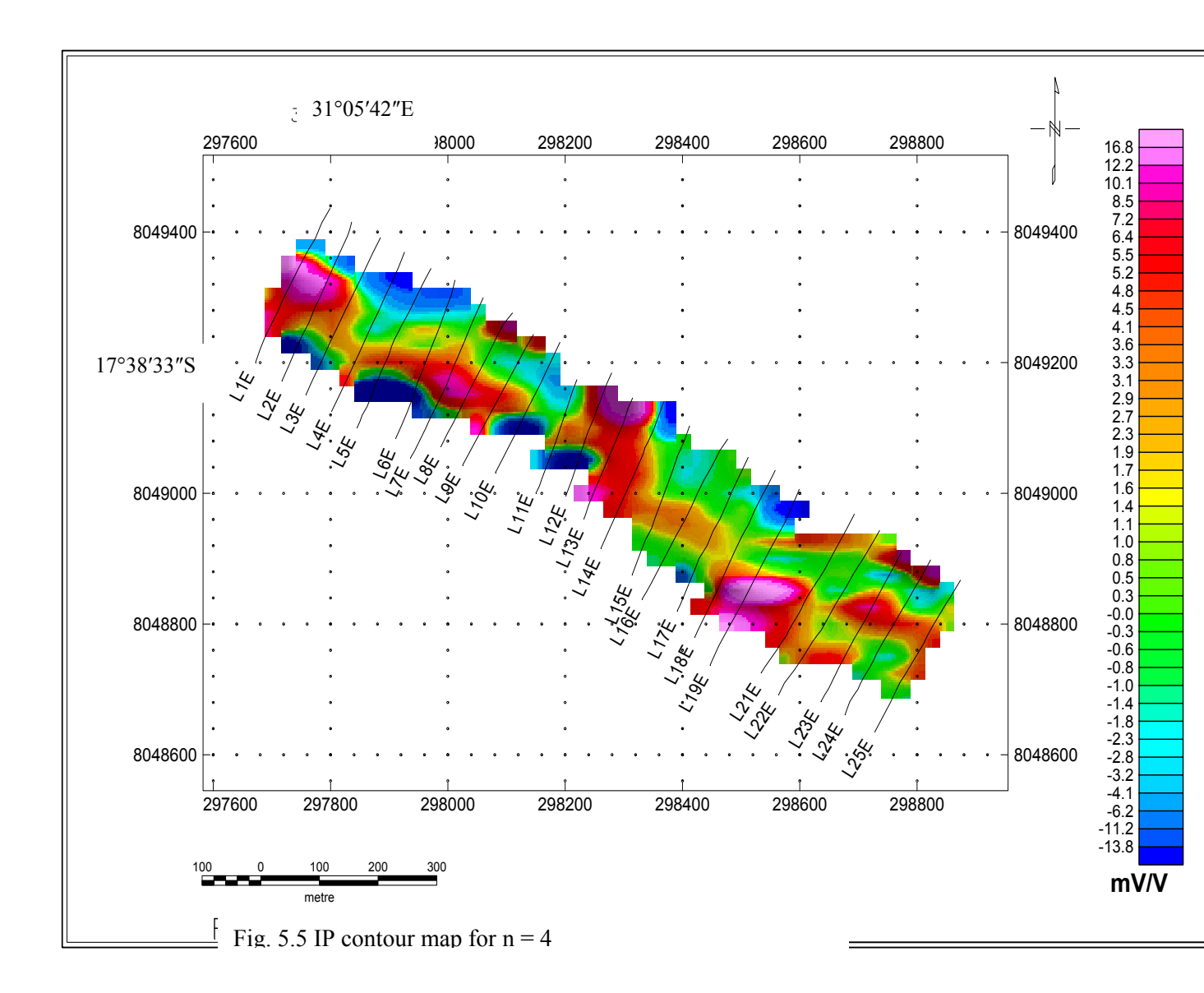
The Western IP1, SIP1 and Eastern IP1 anomalies appear on the contour map for n = 2, suggesting that they might be deep-seated (Fig. 5.3). The Western IP2 anomaly vanishes on the n = 2 map, which suggests that it is a near surface feature. There is now a chargeability high at the southern end of Line 22E.

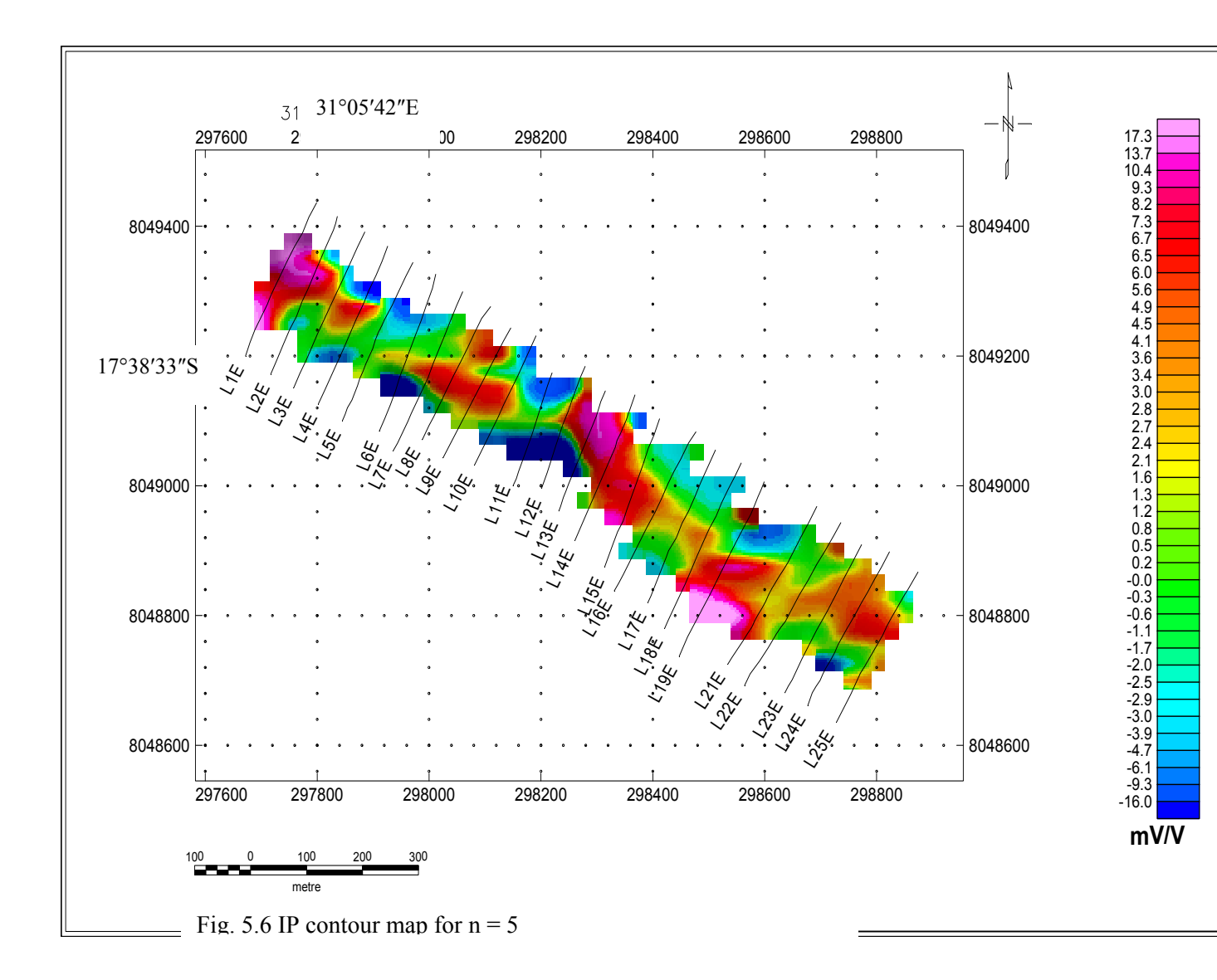
The contour map for n=3 reveals a small anomalous zone at the beginning of Lines 1E and 2E, to the north of the Western IP anomaly 1 (Fig. 5.4). This anomaly also exists on the n=1 and n=2 contour maps. A small chargeable patch is also revealed on Line 9E. There is broadening of the Eastern IP1 anomaly and this suggests that it is deep-seated. The Western IP anomaly 1 is also still appearing on this contour map.

The contour map for n = 4 (Fig. 5.5) shows that the Western IP anomaly 1 is weakening to the east. The Line 9E IP anomaly no longer appears on this contour map. This suggests that it is a small chargeable body. The contour map reveals yet another anomalous zone at the northern edge of the grid. It is located at the beginning of Lines 12E and 13E. This anomaly shall be referred to as the Northern IP anomaly 1 (NIP1). The Eastern IP1 anomaly is still easily visible, suggesting that it is deep-seated.









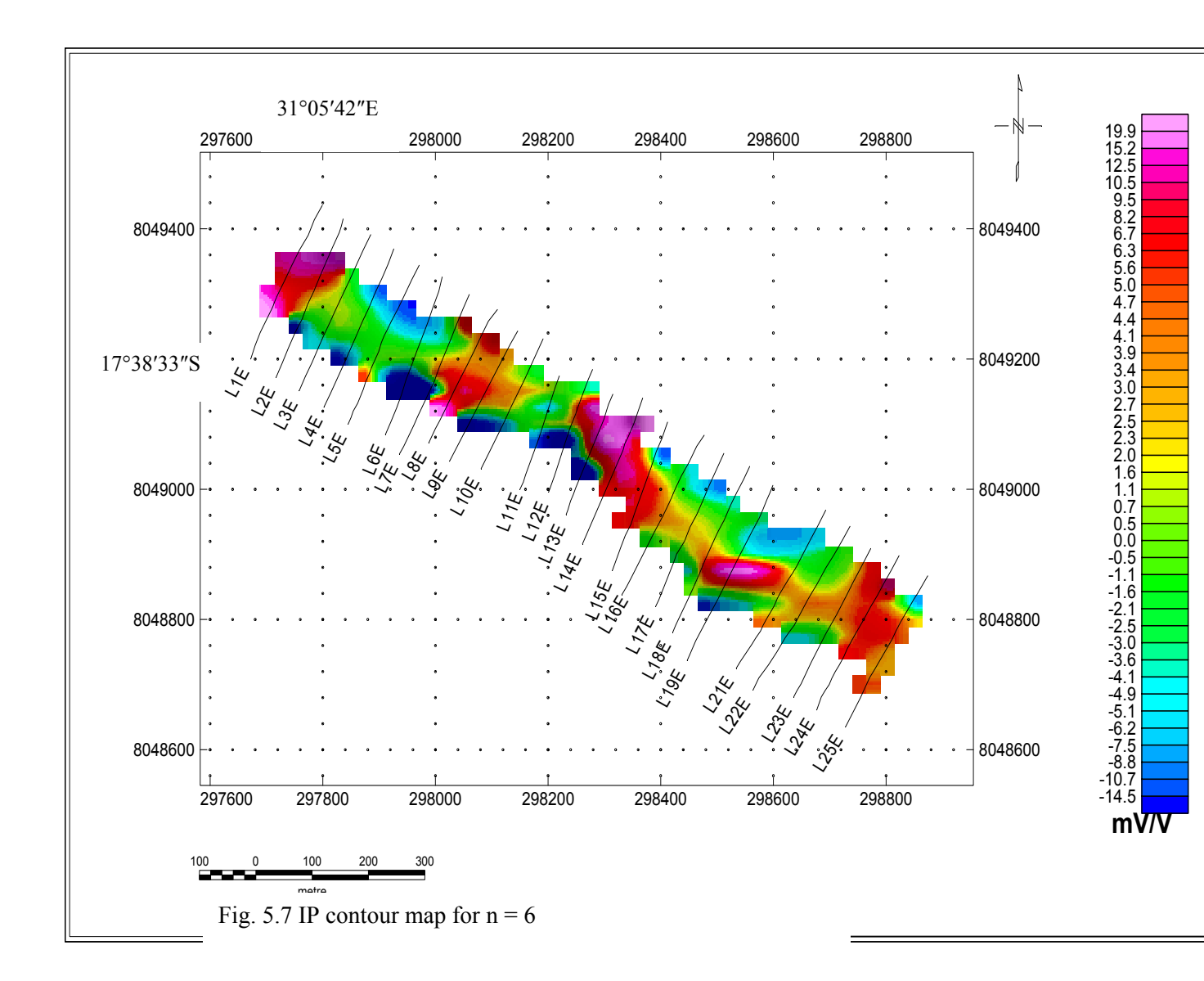
On the contour map for n = 5, the Northern IP anomaly 1 (NIP1) is weakening suggesting that it is due to a small chargeable body (Fig. 5.6). The Western IP1 is also weakening to the east and the Eastern IP1 anomaly is still dominant but is weakening to the north and stretching to the east. Another small chargeable zone appears to the south of the Western IP anomaly 1.

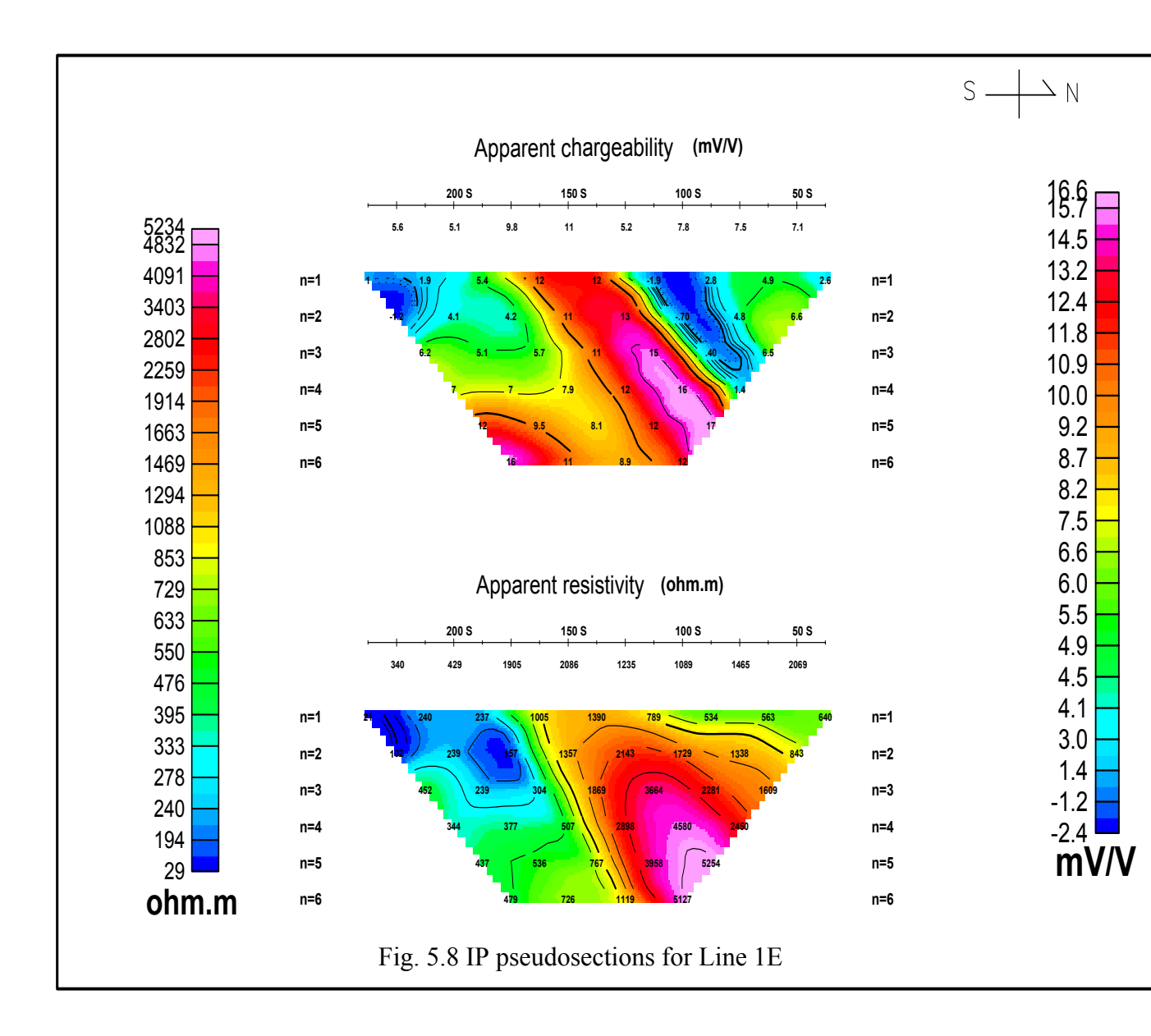
The Eastern IP1 anomaly disappears on the contour map for n = 6, and yet another small chargeable patch appears to the south of the Eastern IP1 anomaly (Fig. 5.7). The Western IP anomaly 1 is stretching to the east and the South West IP anomaly is becoming broader, which suggests that it is deep-seated.

5.3.3 Pseudosections

5.3.3.1 Line 1E

The chargeability plot (Fig. 5.8) shows a small peak at n = 6 around station 187.5S (part of the WIP1). This anomaly has a maximum chargeability of 16 mV/V and a resistivity of 479 Ω m. A broad anomalous zone, also part of the WIP1 is shown on the chargeability plot to be running between stations 87.5S and 175S. It starts from n = 1 and extends down to n = 6. It has the highest chargeability of 17 mV/V at n = 5, suggesting a body which extends to depth. The anomaly is very resistive at depth, being associated with the highest resistivity of 5 254 Ω m found on the line.





5.3.3.2 Line 2E

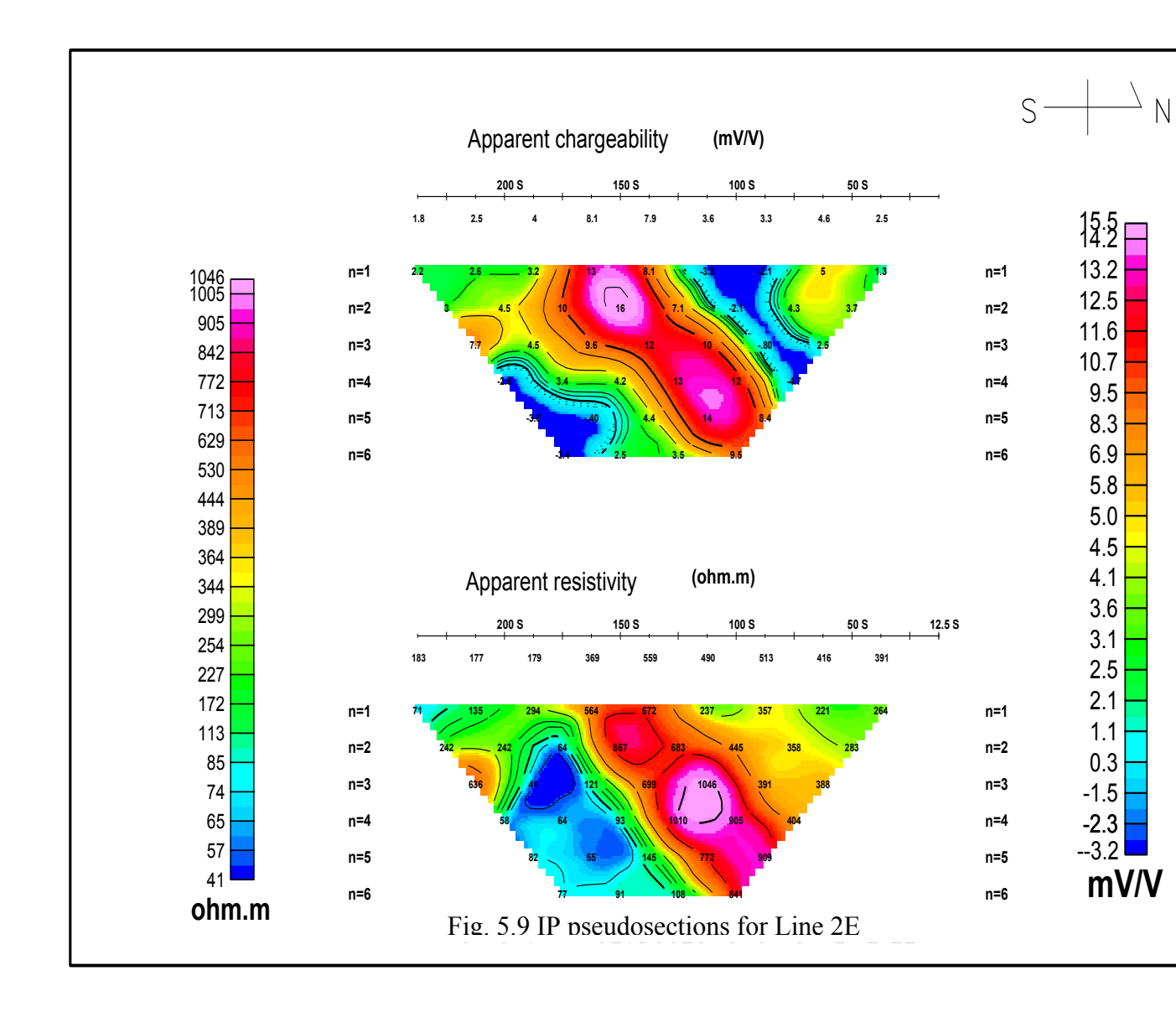
Two chargeability highs can be identified at n=2 and n=5, as part of the Western IP anomaly 1 (Fig. 5.9). This suggests that the peaks are due to a shallow and a deep-seated body respectively. The first peak has its highest chargeability of 16 mV/V and highest resistivity of 867 Ω m, and the second peak has its highest chargeability of 14 mV/V and highest resistivity of 772 Ω m. One smallish peak centred on station 212.5S, which has a chargeability value of 7.7 mV/V at n=3 is also revealed on the line. Negative chargeability values surround the WIP1 anomaly, both on its western and eastern sides.

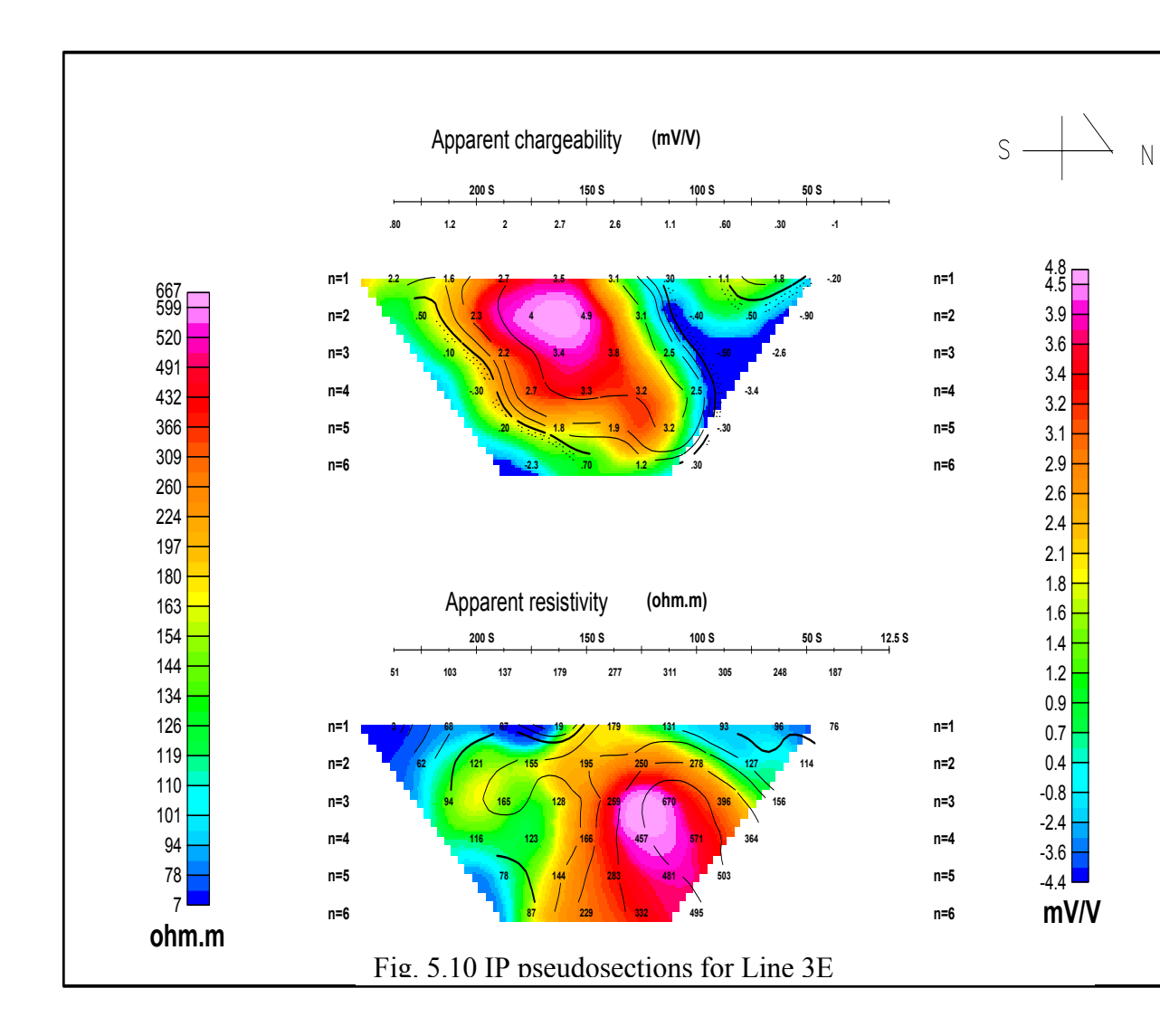
5.3.3.3 Line 3E

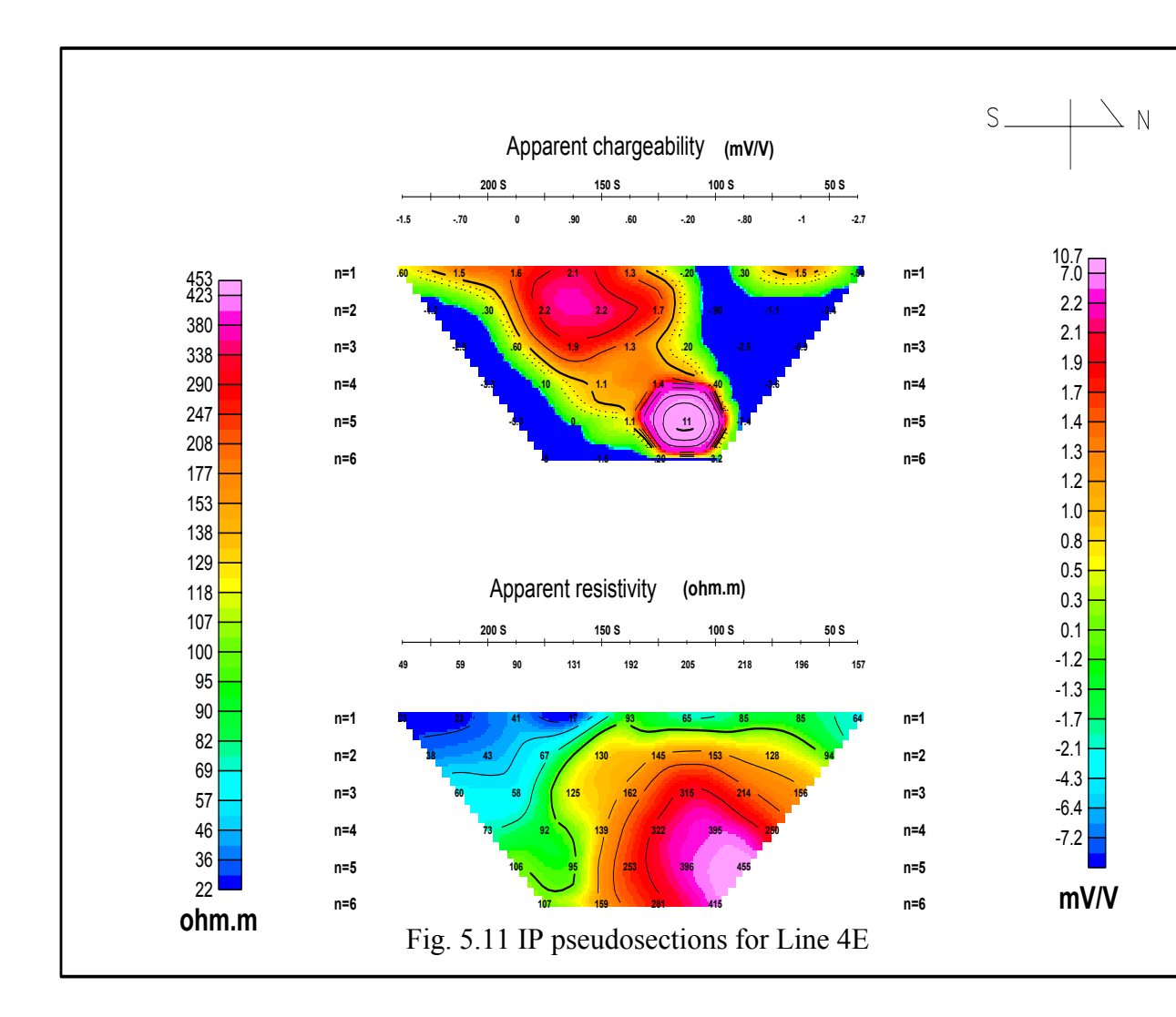
One anomaly is apparent (part of the WIP1 anomaly) centred on station 150S (Fig. 5.10). It has its highest chargeability of 4.9 mV/V on the n = 2 section. The anomaly extends to depth from the surface and is associated with moderate to high resistivities. The negative IP values are still apparent on both sides of the anomaly.

5.3.3.4 Line 4E

This line (Fig. 5.11) shows a deep anomalous zone between stations 87.5S and 137.5S (part of the WIP1 anomaly). Centred on station 162.5S is a weakly chargeable shallow patch (since chargeabilities are around 2.2 mV/V), which starts from the surface and extends down to the n = 3 section. A second anomaly which has its highest chargeability







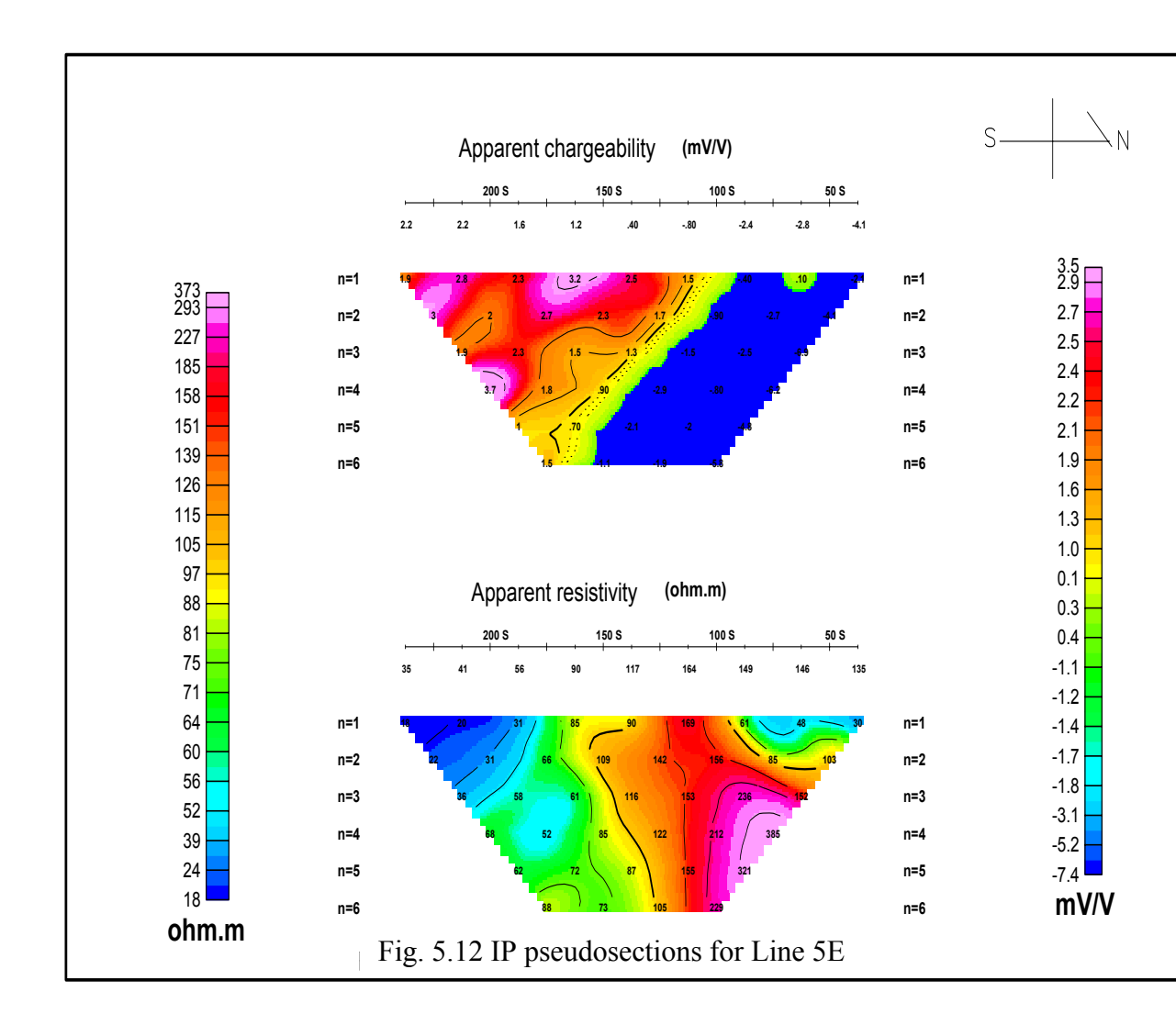
of 11 mV/V is at the n = 5 to 6 section, suggesting a deep-seated feature. These two anomalies are possibly due to a single highly resistive body as indicated from the resistivity section.

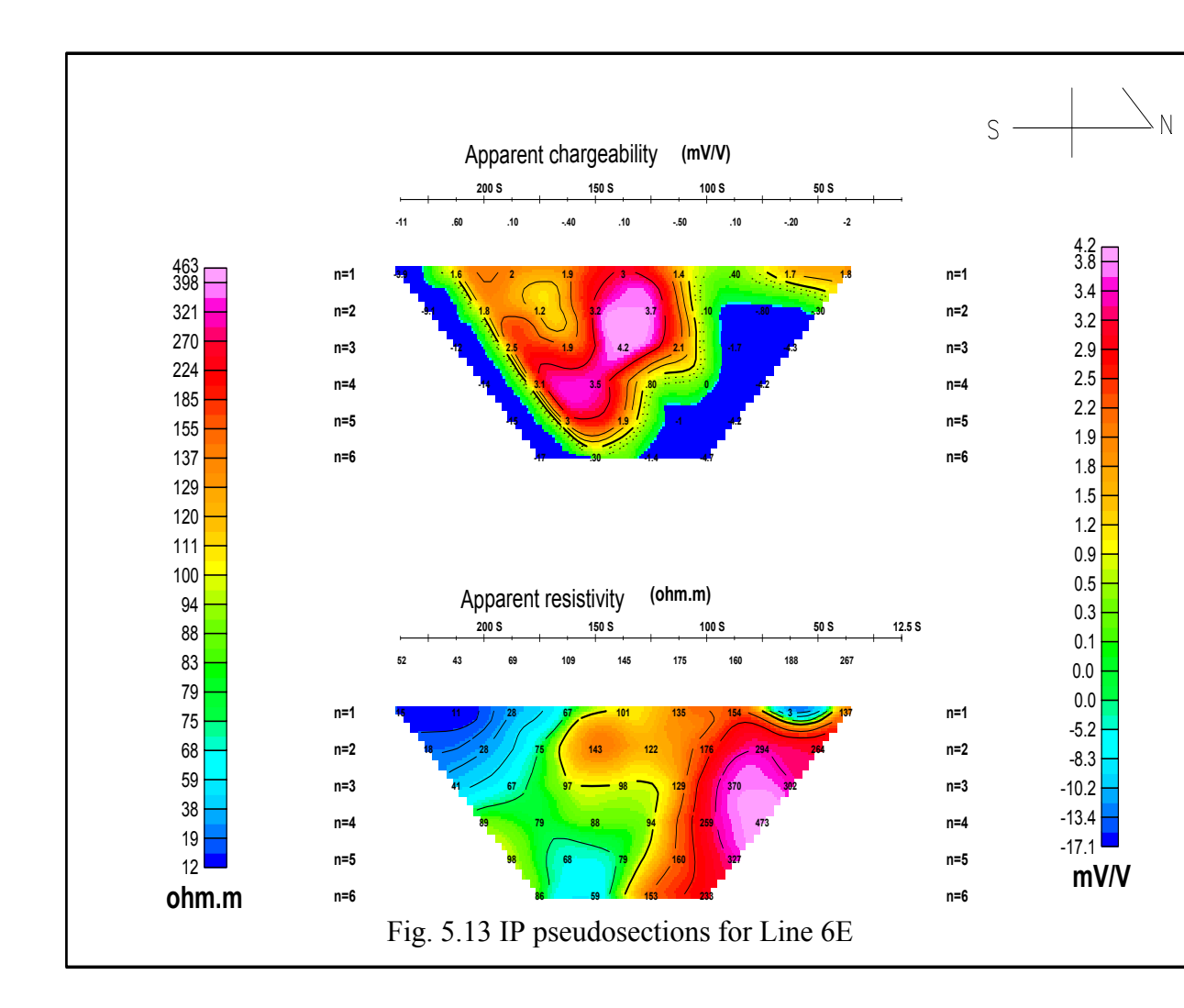
5.3.3.5 Line 5E

The northern end of the chargeability pseudosection (from station 35S up to 100S) is a negative IP zone (Fig. 5.12). The resistivity pseudosection shows that there exists a fairly resistive patch centred at 112.5S on surface and extending to n = 6. From the middle of the line, up to its southern end there is an anomalous zone (part of the WIP1 anomaly) in which three peaks can be identified. Two smallish ones centred on stations 200S and 225S, have their highest chargeabilities on the n = 4 and n = 2 respectively. The broader anomaly starts from the surface down to the n = 3 section. They are all associated with low chargeabilities and fairly low resistivities.

5.3.3.6 Line 6E

The chargeability section reveals one major anomaly, interpreted to be part of the WIP2 anomaly (Fig. 5.13). The broad anomaly stretches between stations 112.5S and 187.5S and is associated with moderate resistivities (e.g. $\sim 100~\Omega$ m) and it is surrounded by negative IP values on either side. The fairly resistive patch on the northern side which is coinciding with the negative chargeability zone is broadening to the north.



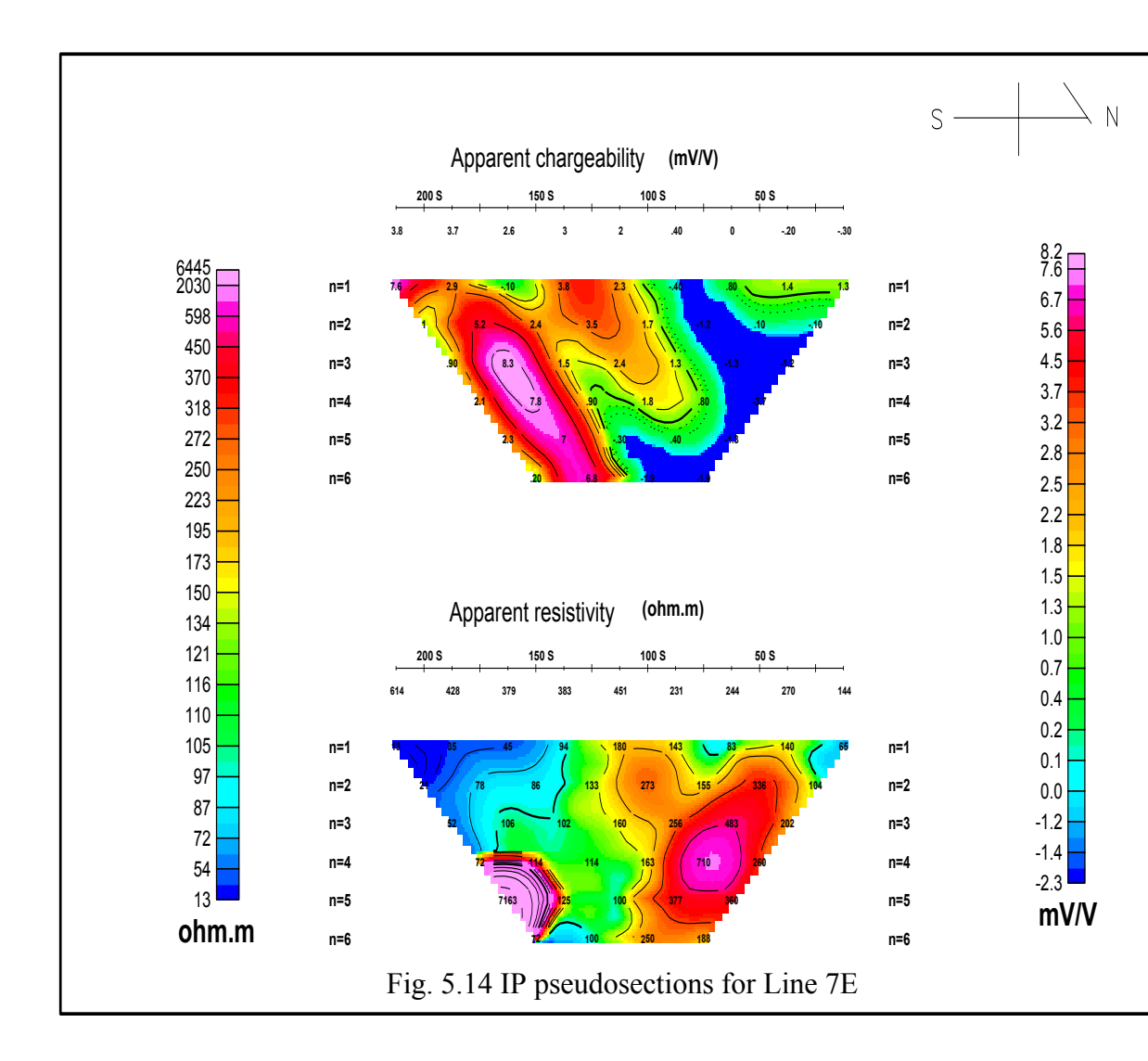


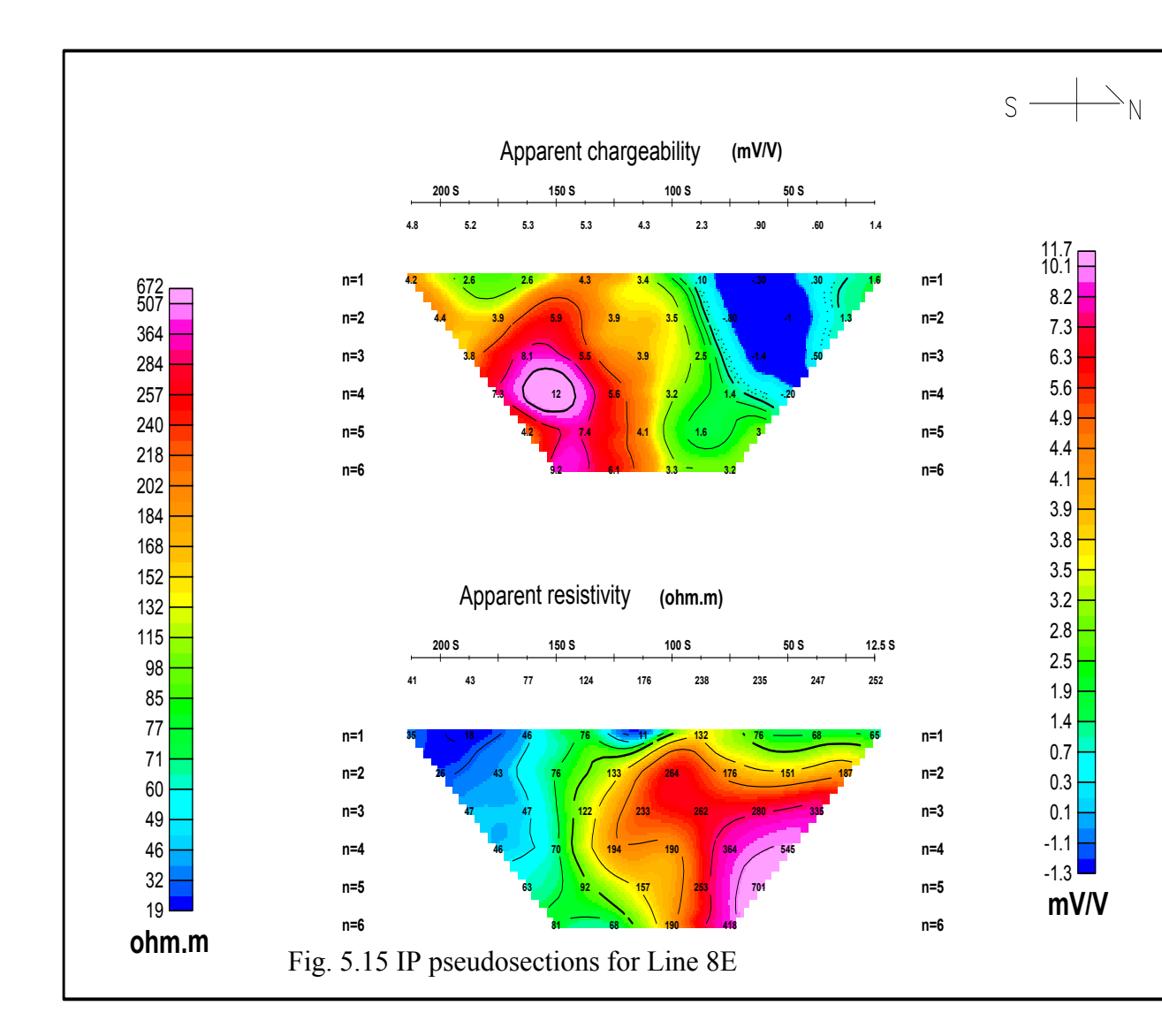
5.3.3.7 Line 7E

The chargeability pseudosection shows two anomalous zones which extend from station 112.5S to station 187.5S (Fig 5.14). The southernmost one starts from n = 1 down to n = 6 and its highest chargeability of 8.3 mV/V occurs at n = 3, suggesting that it is a deep-seated body. The highly chargeable parts are associated with moderate resistivities, which suggest that it is a moderately conductive body. A small peak is also apparent at the end of the line. It is shallow and is associated with very low resistivities. Another chargeable, shallow seated patch centred on 125S is apparent and this is associated with moderate to high resistivities. The negative IP values on the northern end of the line are still apparent and these coincide with high resistivity values.

5.3.3.8 Line 8E

This line has an anomalous zone which starts from n = 1 extending with depth and it is part of WIP2 (Fig. 5.15). It has its highest chargeability of 12 mV/V at n = 4, suggesting a body extending to depth. The highly chargeable parts are associated with fairly low to moderate resistivities of 47 to 70 Ω m. High resistivity values of about 194 Ω m are apparent to the north of the anomaly.





5.3.3.9 Line 9E

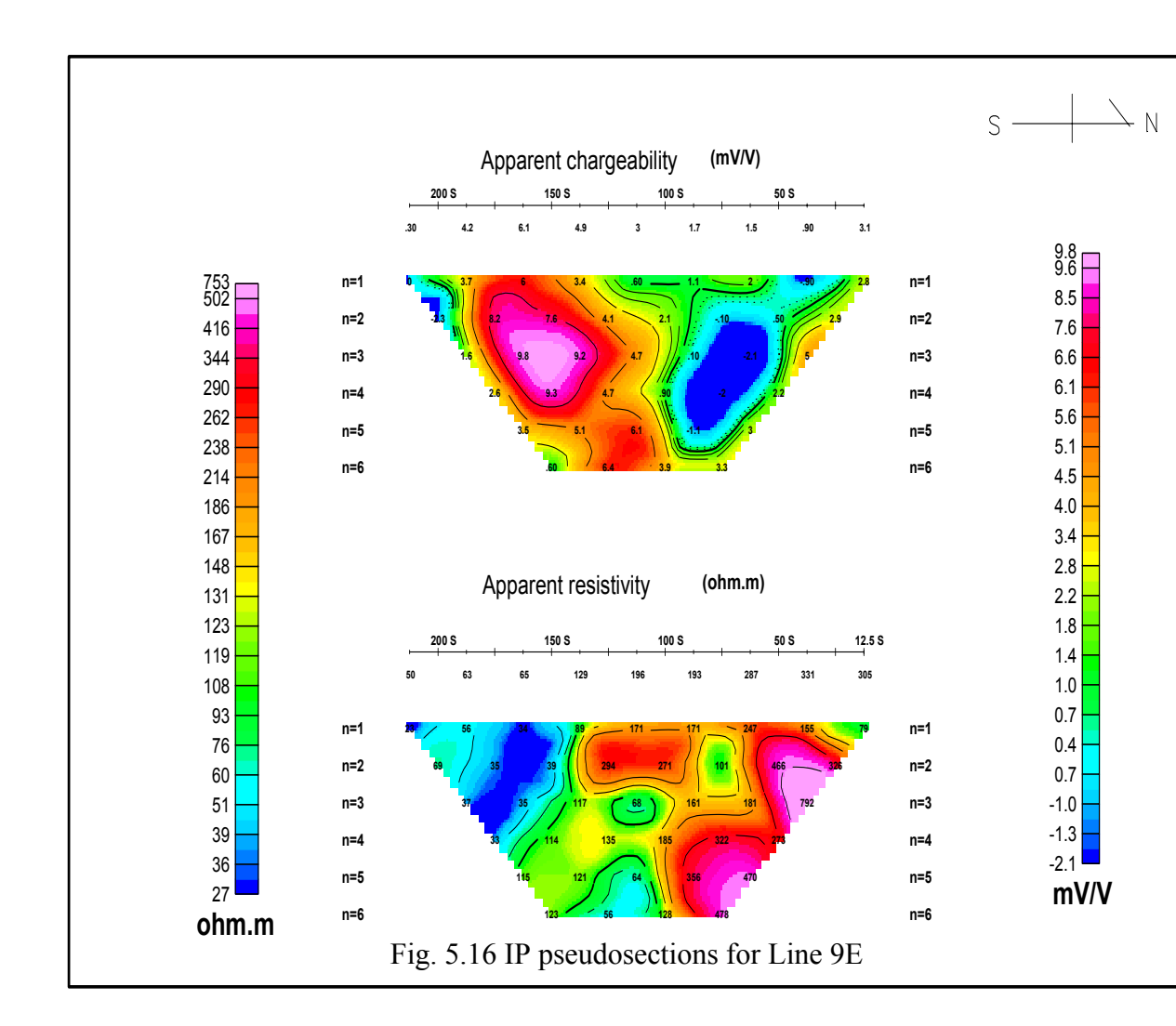
The chargeability pseudosection shows an anomalous body, part of WIP2, which starts from the surface and extends down to n = 5 section (Fig. 5.16). It is centred on station 162.5S and has its highest chargeability at n = 3. It starts from n = 1 and extends to depth. The anomaly is associated with very low resistivities 35 Ω m, which suggests that it is conductive. Negative chargeability values on the northern side of the line are still apparent and these are associated with high resistivity values.

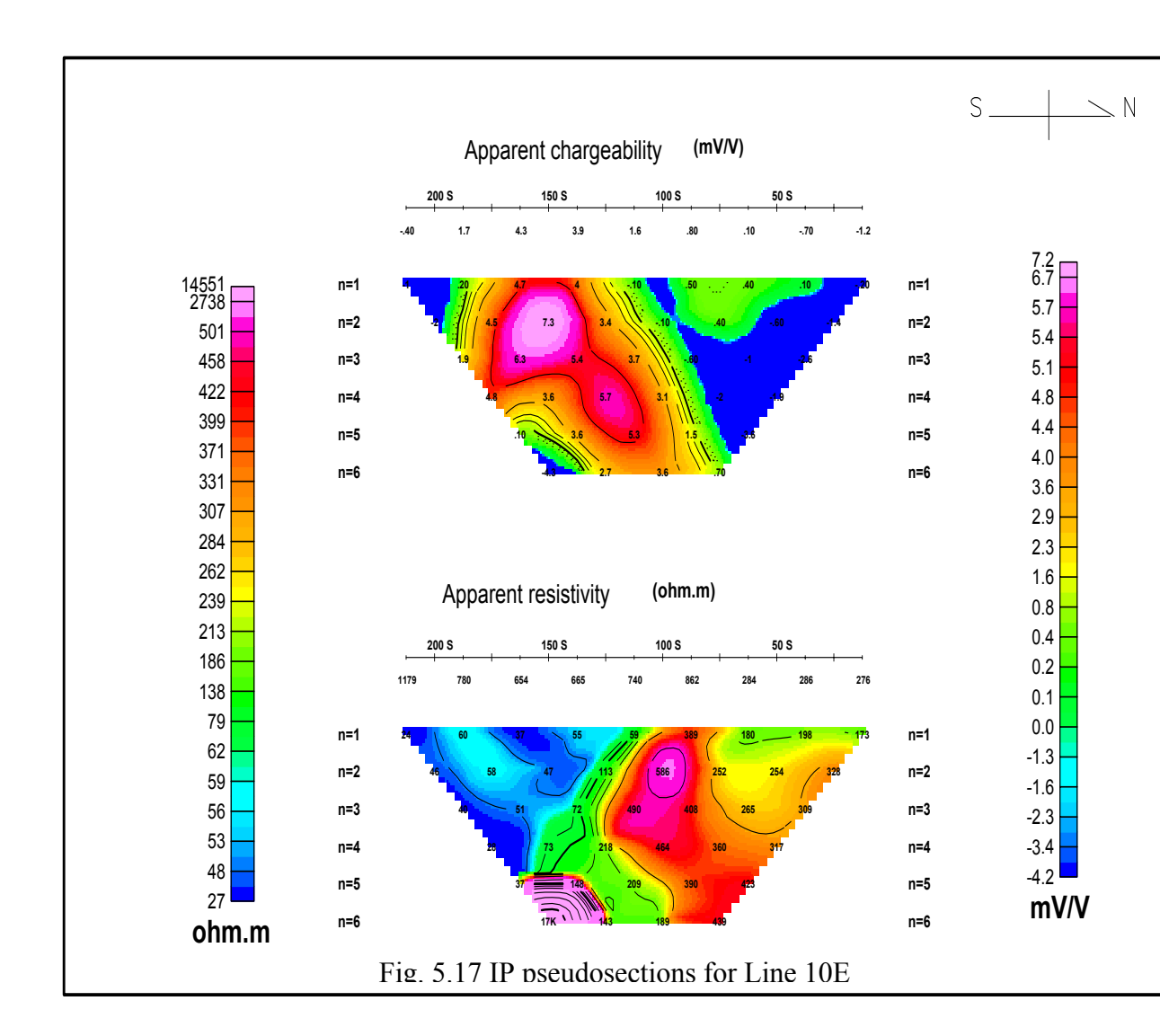
5.3.3.10 Line 10E

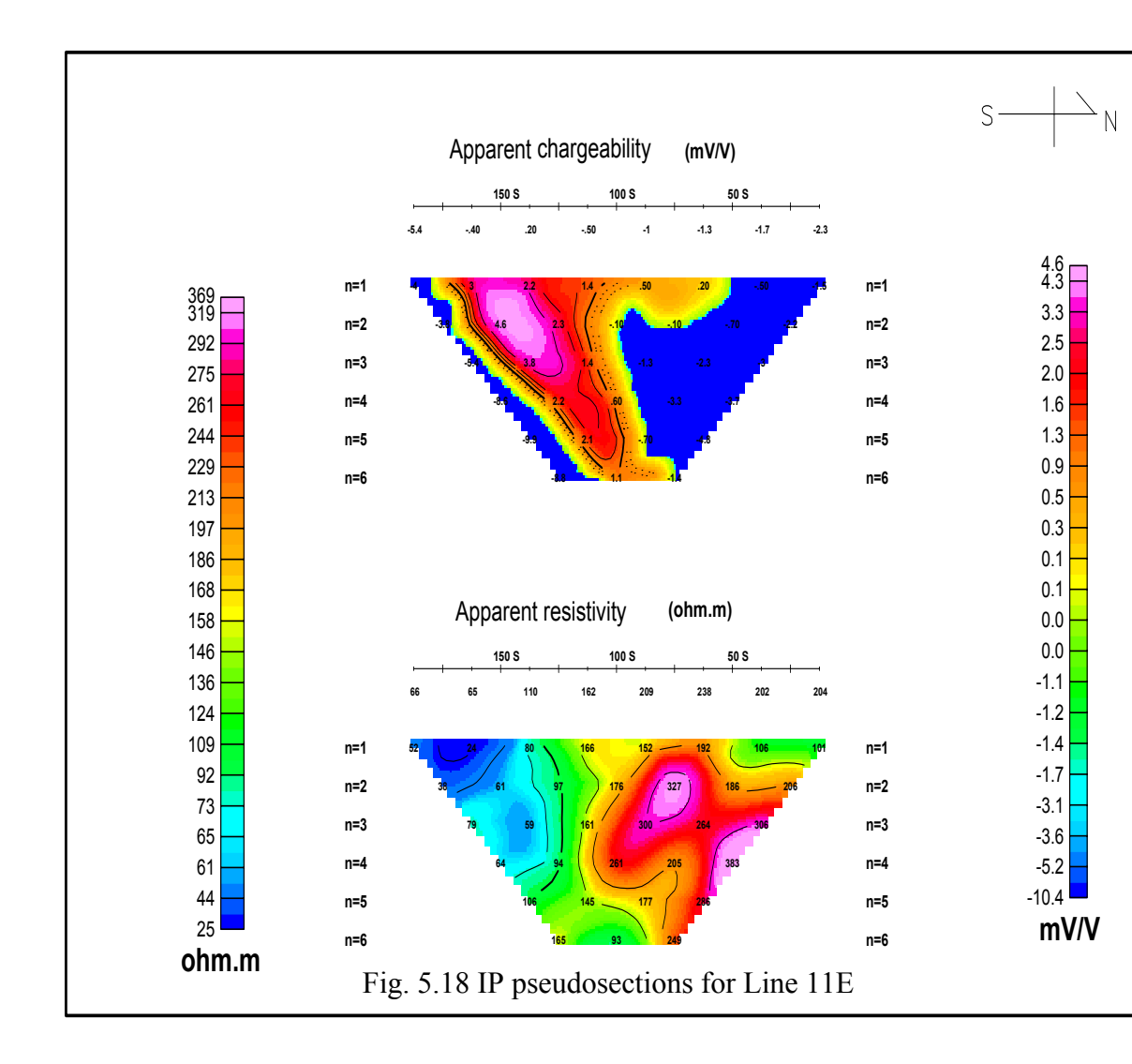
Besides the negative chargeability zone, on the northern end of the chargeability pseudosection, there exists a broad anomaly, in which two peaks are identified to be centred on stations 125S and 150S (Fig 5.17). The anomaly is associated with low resistivity values suggesting a conductive layer. There exists a very highly resistive structure underneath this conductive layer.

5.3.3.11 Line 11E

The southern end of the line shows an anomalous zone, which is part of the SIP1 (Fig. 5.18). It starts from the surface and extends down to a depth of n = 5. The anomaly has its highest chargeability at n = 2 suggesting a near surface feature. It is also associated with low resistivities and is surrounded by a negative chargeability zone.







5.3.3.12 Line 12E

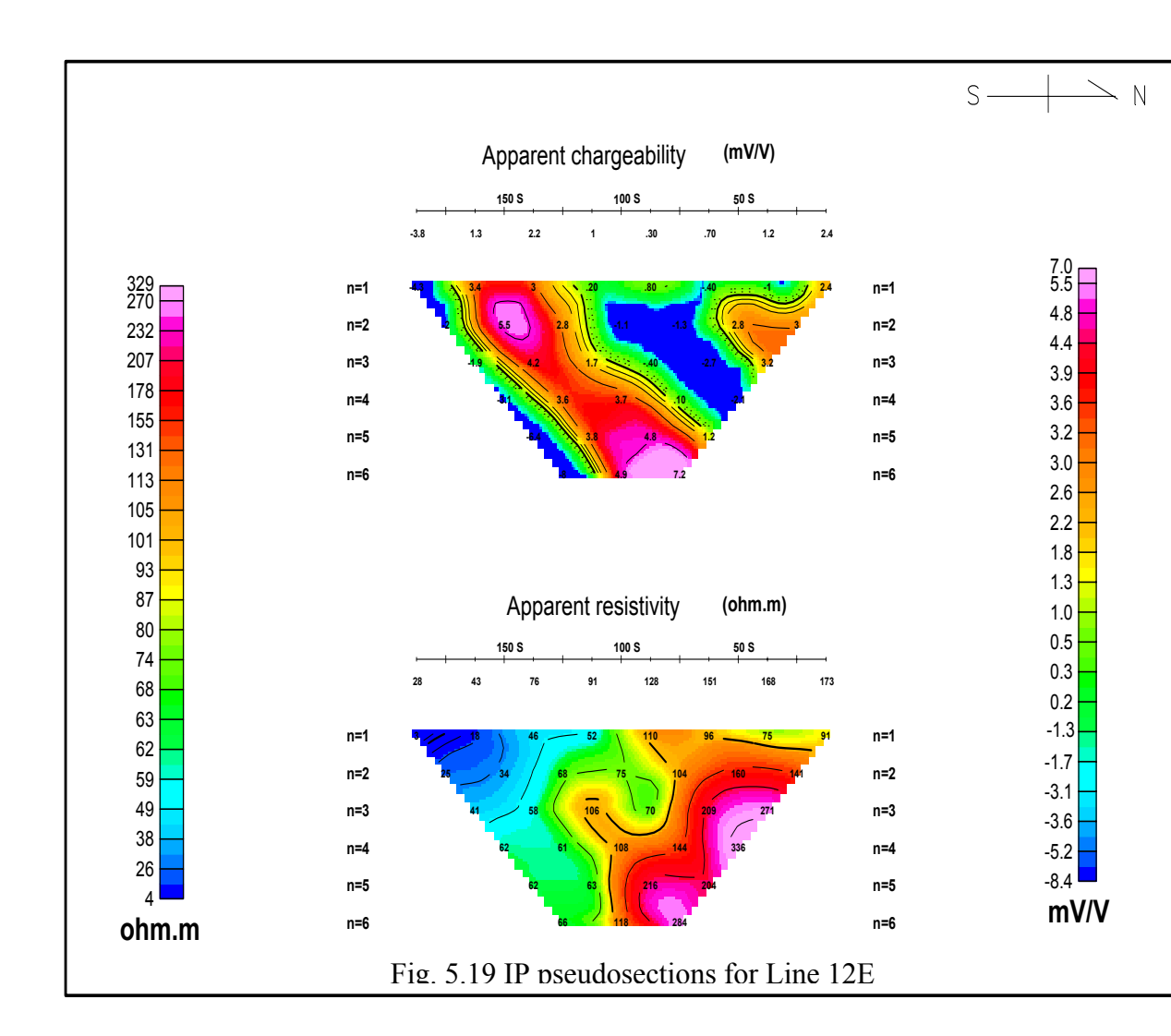
Two peaks are revealed on the chargeability pseudosection, which is also part of the SIP1 (Fig. 5.19). These are centred at 75S and 150S and have their highest chargeability values at n=6 and n=2 respectively. This suggests a deep-seated and a shallow body respectively. The second one is associated with very low resistivities of 34 Ω m and the first one is associated with a fairly moderate resistivity value of 284 Ω m. The section also shows a small chargeable zone centred on station 37.5S which is associated with fairly moderate resistivity values of about 336 Ω m.

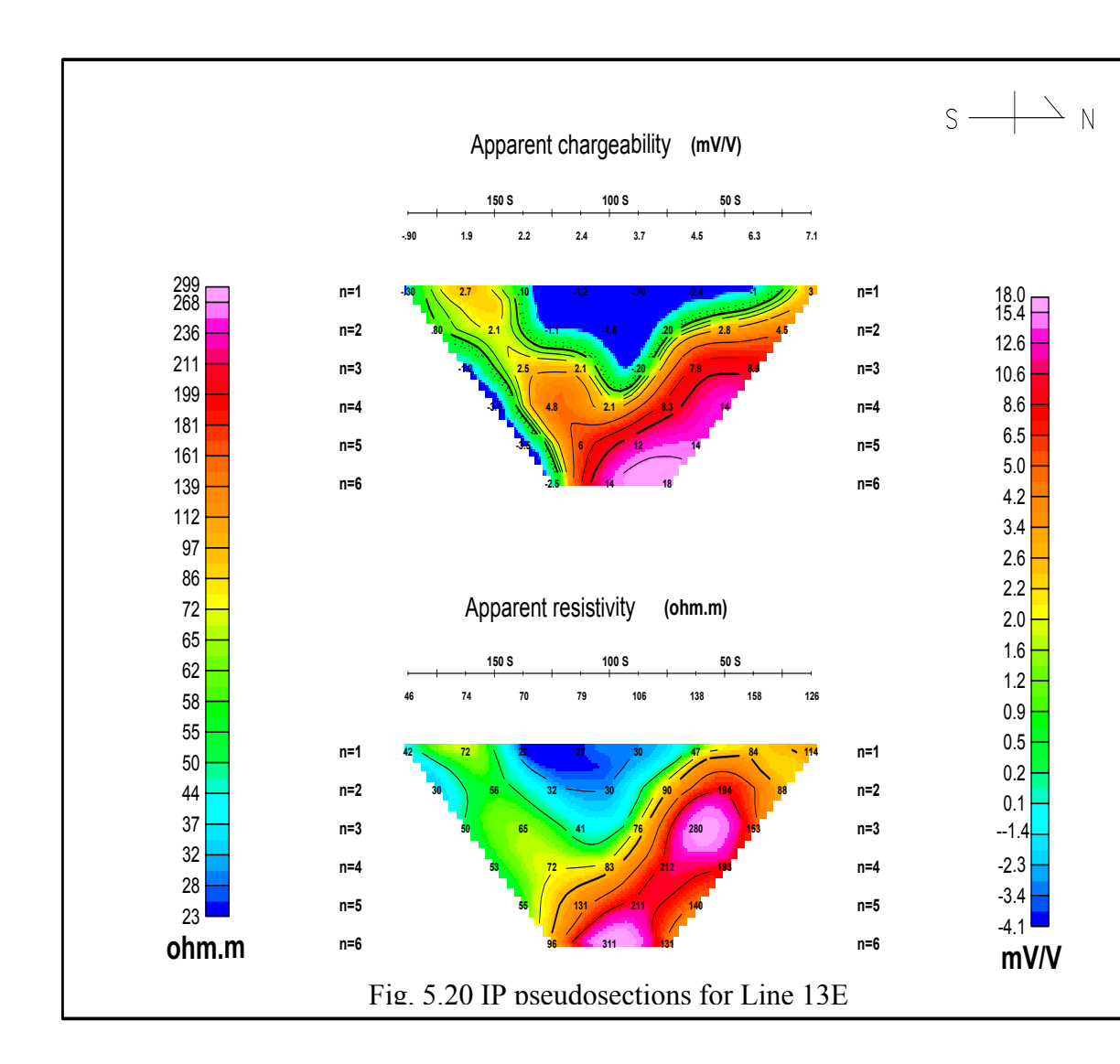
5.3.3.13 Line 13E

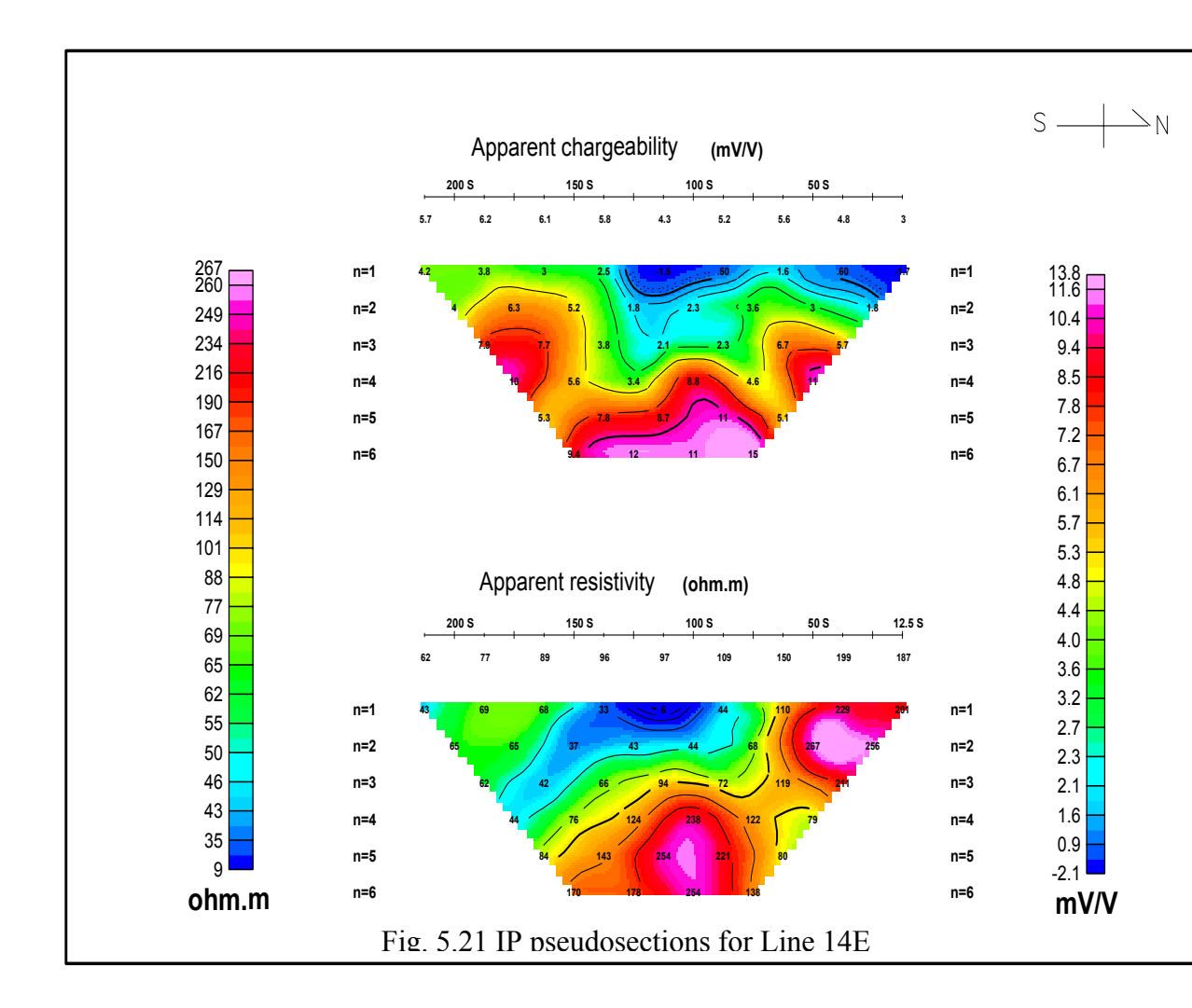
A moderately resistive anomaly which starts from n=1 on the northern side and extends to depth, stretches between stations 37.5S and 112.5S (Fig. 5.20). It is part of the SIP1 and its highest chargeability value of 18 mV/V occurs on the n=6 level, with a resistivity of 311 Ω m. There is also another weakly chargeable arm centred on station 150S which is associated with resistivity values of about 65 Ω m.

5.3.3.14 Line 14E

Three anomalous zones can be identified on the chargeability pseudosection (Fig. 5.21). Two of them are small and are centred on stations 50S and 175S. Both of them are associated with resistivity values of about 79 and 41 Ω m respectively. The major







anomaly is associated with moderate resistivities of 254 Ω m. It starts on the n = 4 section and extends with depth. It is part of the SIP1 and NIP1 anomalies.

5.3.3.15 Line 15E

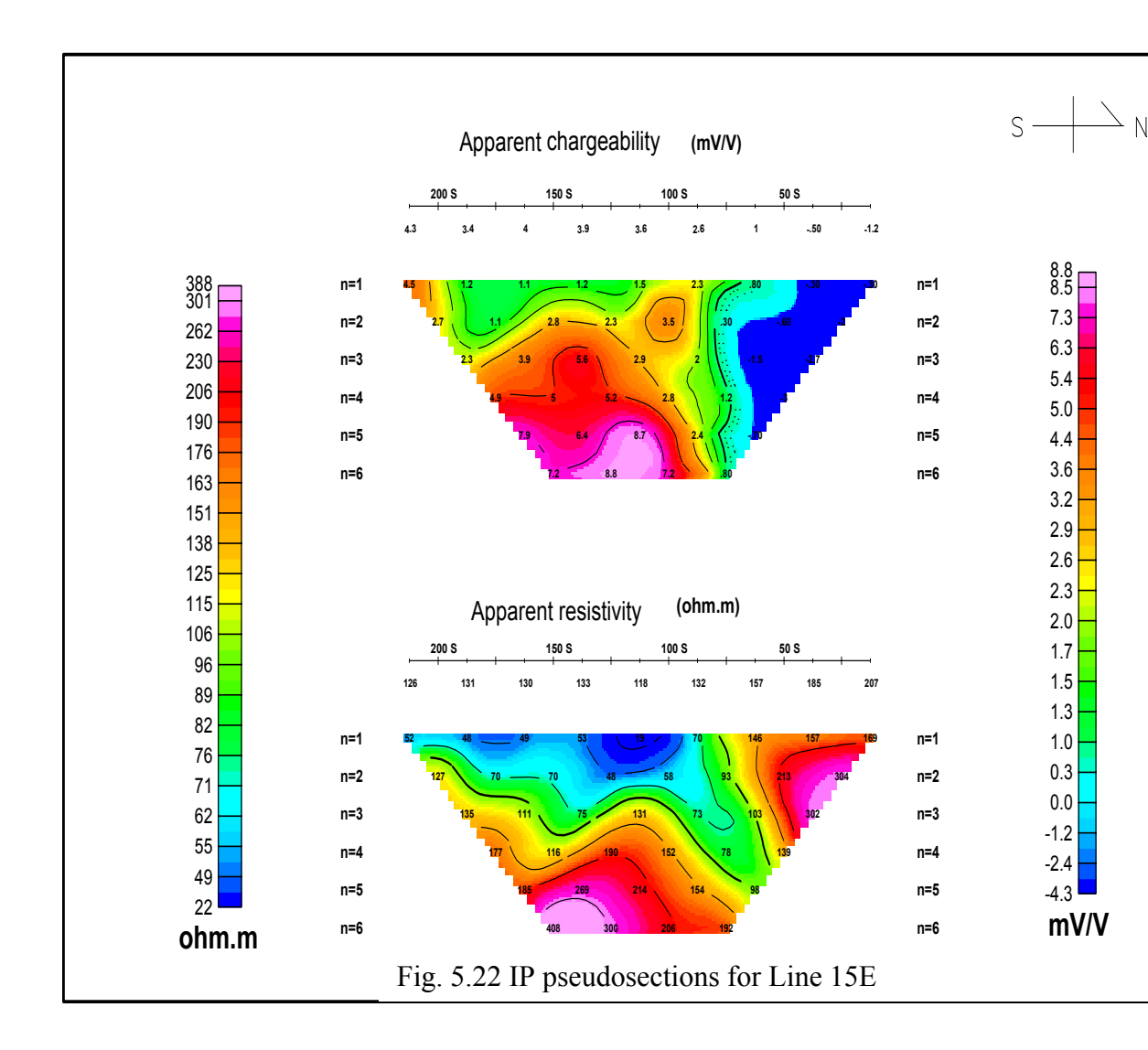
The line reveals part of NIP1 between stations 87.5S and 187.5S starting from n = 3 and extending with depth (Fig. 5.22). It has moderate to high resistivity values and has its highest chargeability at n = 6 suggesting a body which extends to depth. The northern end of the line (from station 12.5S up to station 75S) shows a zone of low chargeability values which are associated with high resistivity values.

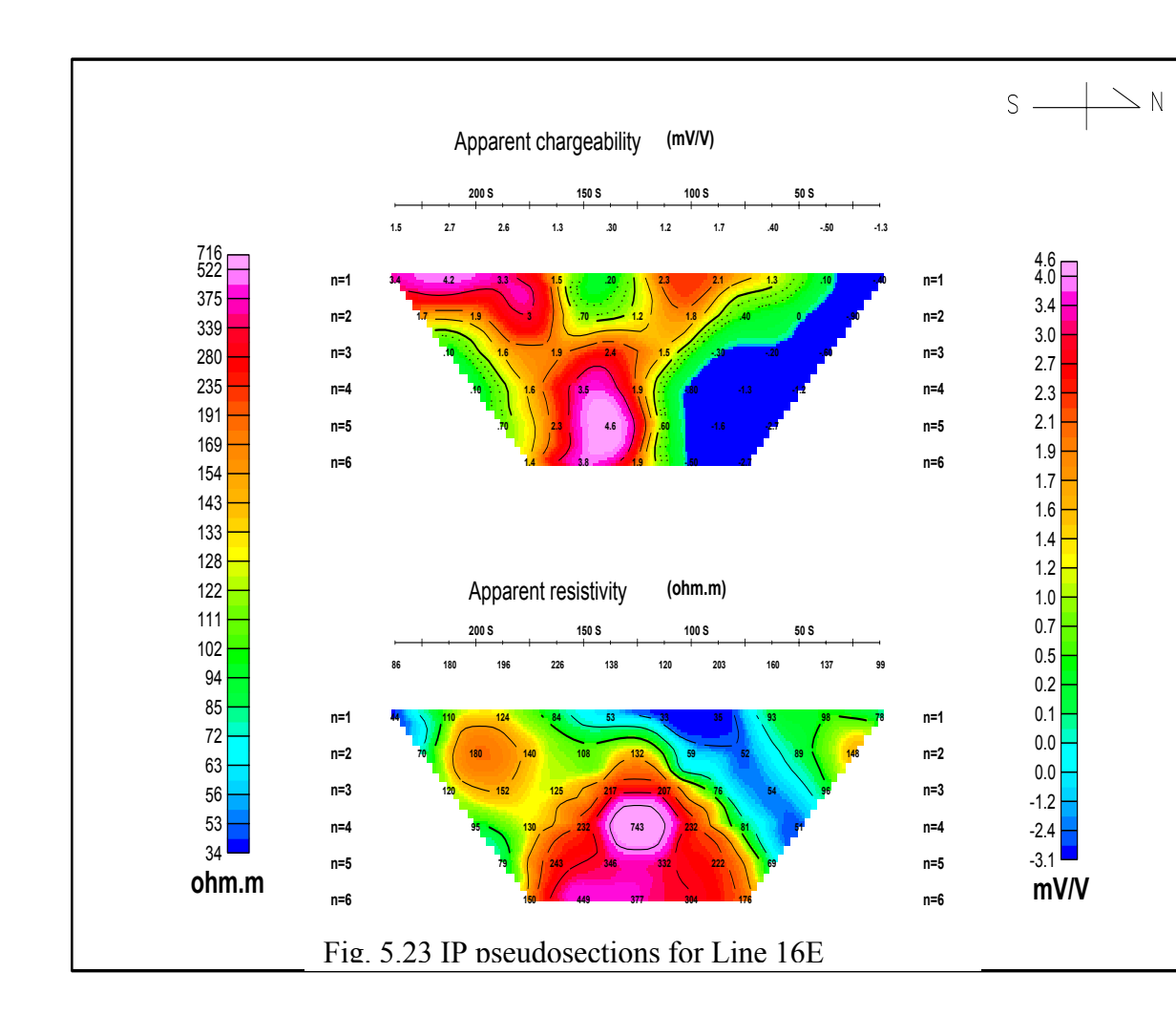
5.3.3.16 Line 16E

The southern side of the line shows two anomalous zones (Fig. 5.23). The first one is deep-seated and has moderate to high resistivities. It is located between stations 125S and 175S. The second anomaly is situated between stations 125S and 287.5S and it starts from the surface down to n = 3. Its highest chargeability value of 4.2 mV/V occurs at n = 1 implying a shallow feature.

5.3.3.17 Line 17E

The chargeability pseudosection reveals an anomalous zone, part of the EIP1, between stations 150S and 287.5S (Fig. 5.24). It stretches between n = 1 and n = 3 and has the





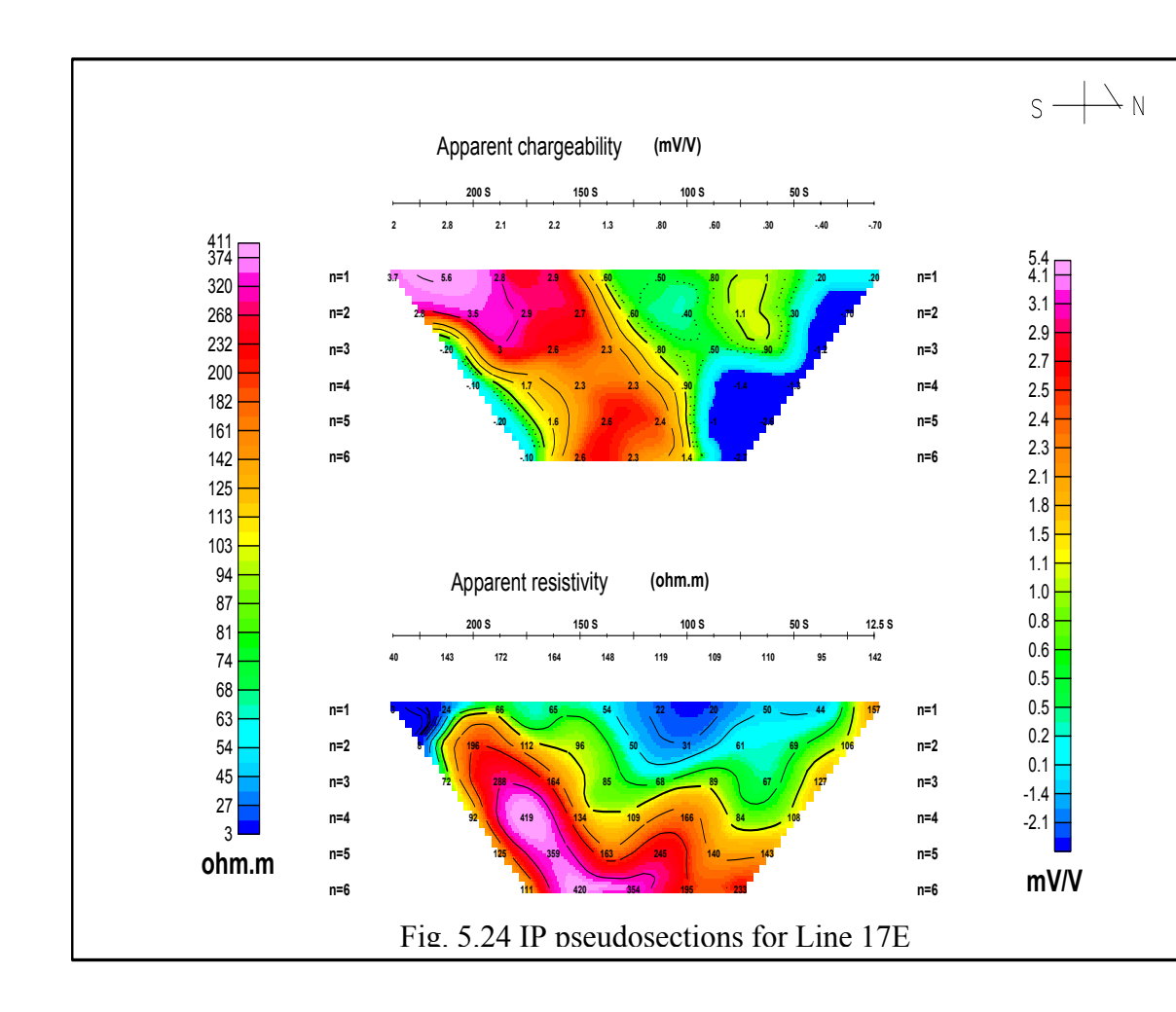
lowest resistivity of 3 Ω m. This suggests that it is a conductive body. There exists a second anomalous zone between stations 100S and 125S which seems to merge into the EIP1 anomaly. It is associated with moderate resistivity values of about 354 Ω m.

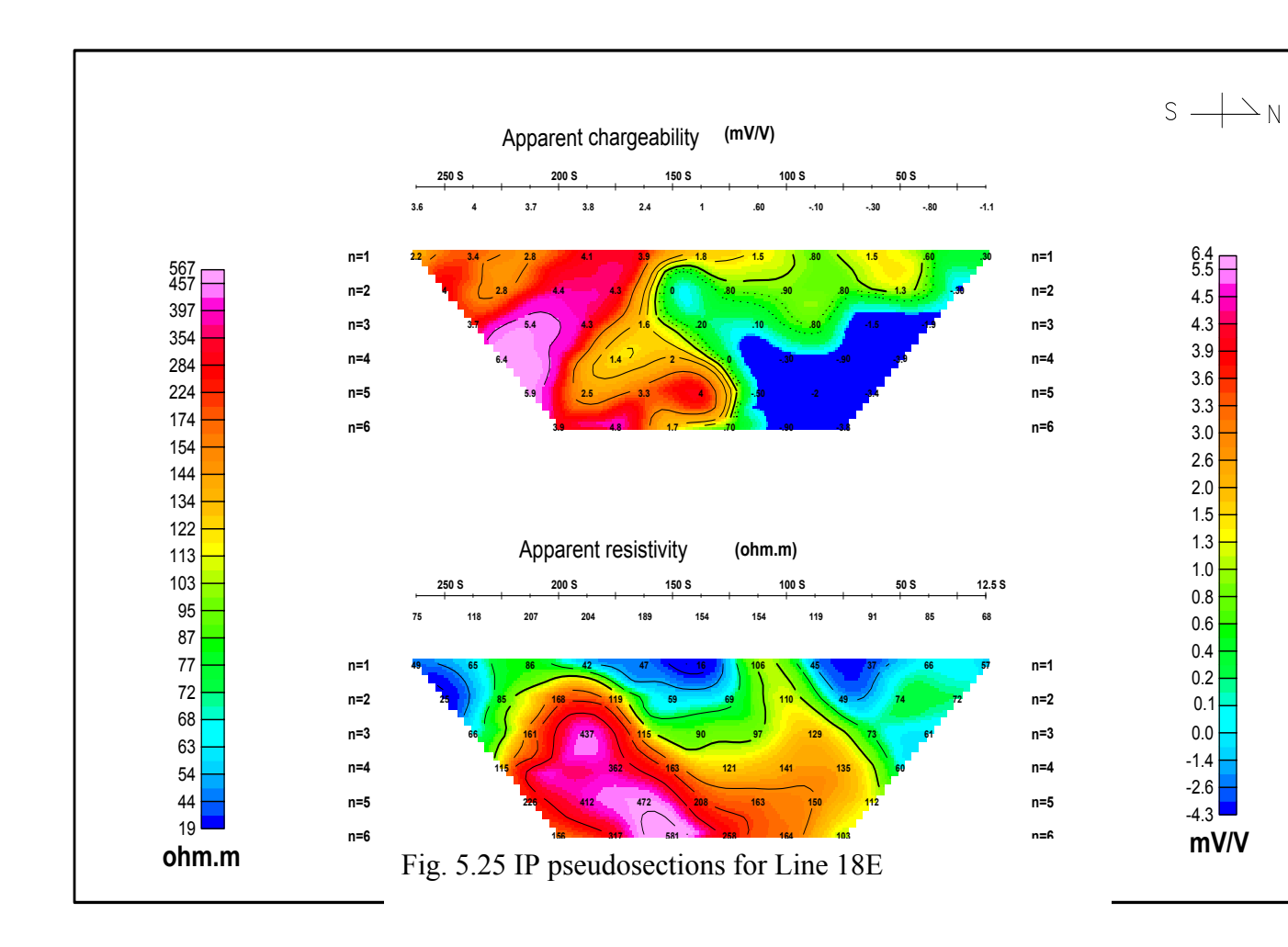
5.3.3.18 Line 18E

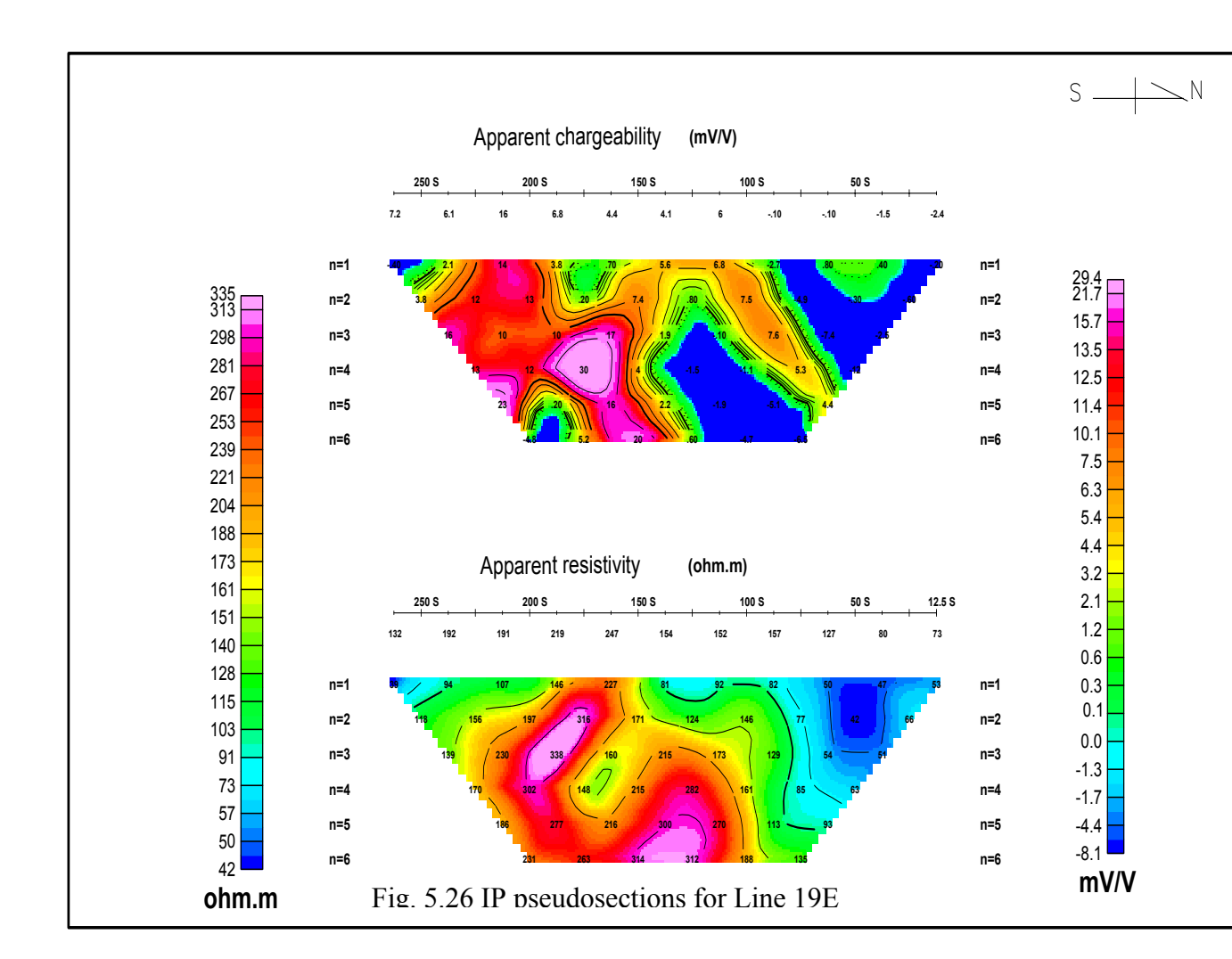
Line 18E shows a broad and resistive anomalous zone located between stations 137.5S and 225S, part of EIP1 (Fig. 5.25). It stretches from the surface down to n = 6. Several peaks can be identified in this zone. These are centred on stations 137.5S, 175S and 225S. The northern side of the anomaly is a negative chargeability zone, associated with moderate resistivity values of about 112 Ω m.

5.3.3.19 Line 19E

One highly chargeable zone (part of EIP1) is revealed between stations 137.5S and 250S (Fig. 5.26). Within this zone, two small peaks can be identified. These are centred on stations 150S and 225S. There is also a broader peak which stretches from 150S up to 200S. The broader anomaly has its highest chargeability of 30 mV/V, occurring at n=4, suggesting that it is deep-seated. It is associated with moderate resistivities (of about 148 Ω m) suggesting that it is a conductive layer. Centred on stations 125S is a fairly chargeable patch which starts from the surface and stretches down to the n=4 section.







5.3.3.20 Line 21E

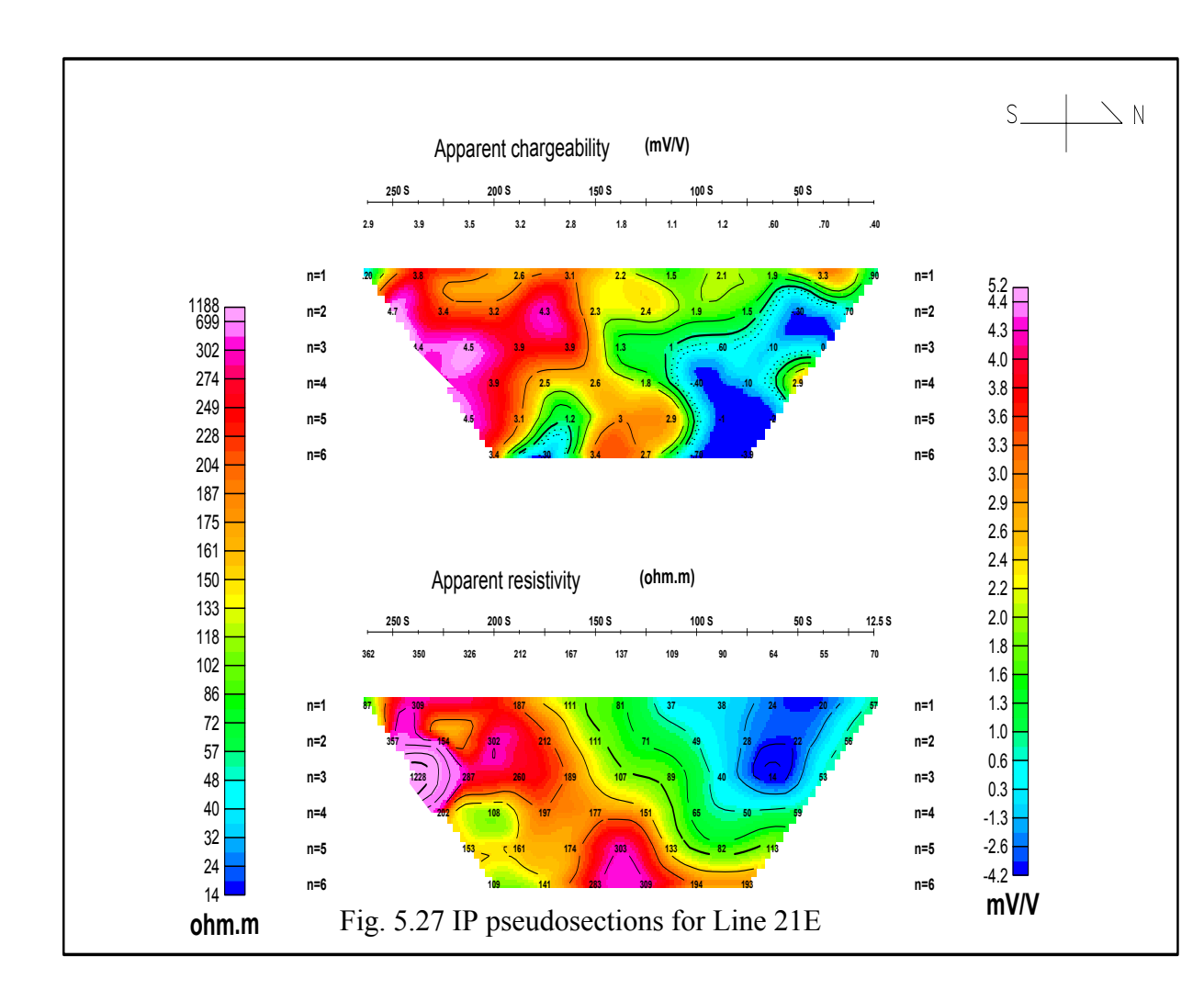
The line reveals part of the EIP1 from station 162.5S up to the southern end of the line (Fig. 5.27). It starts from the surface and stretches down to n = 6. It is a fairly resistive zone, having a maximum resistivity of 1 226 Ω m, which is the highest resistivity found on the line.

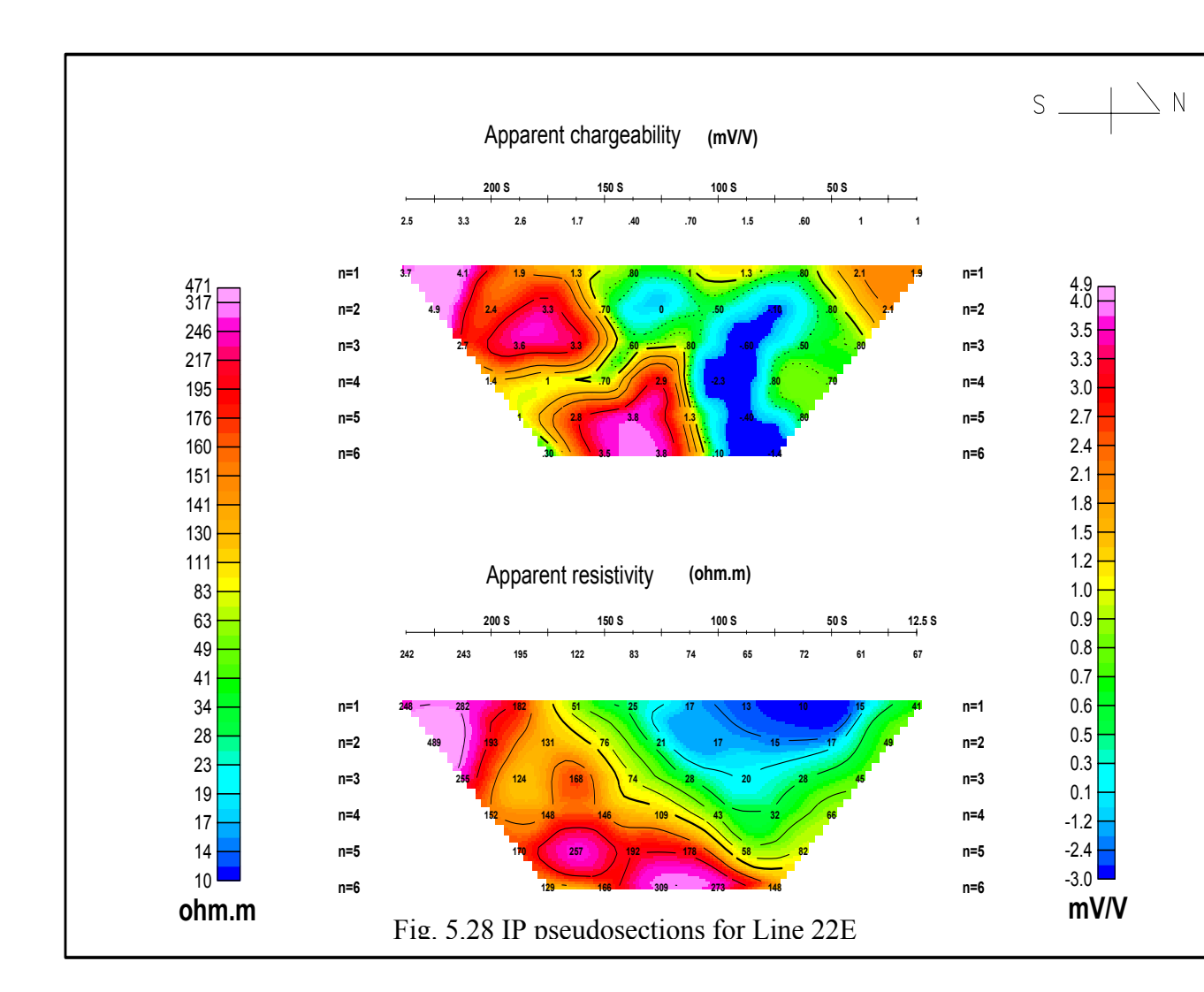
5.3.3.21 Line 22E

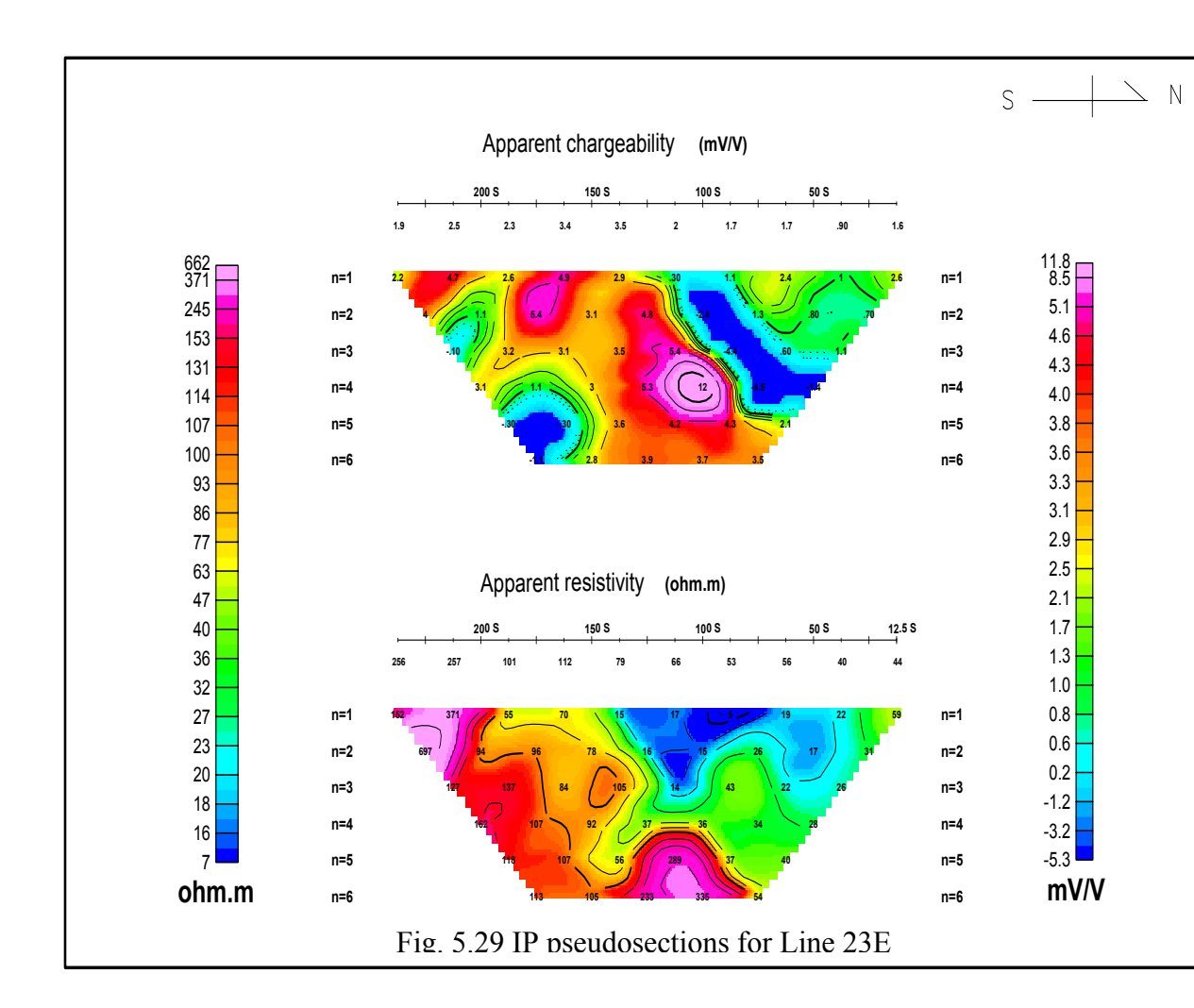
A broad anomalous zone is revealed on this line, part of the EIP1 (Fig. 5.28). Within this zone, three peaks can be identified. The first one is resistive and it stretches between stations 112.5S and 175S. It is deep-seated, being located between the n=4 and n=6 sections and having its highest resistivity value of 369 Ω m occurring at n=6. The second peak stretches between stations 150S and 200S. It has its highest chargeability of 3.5 mV/V at n=3. The third peak is located between stations 200S and 287.5S. It is resistive and near the surface.

5.3.3.22 Line 23E

A small and fairly chargeable patch is revealed between stations 87.5S and 125S (Fig. 5.29). It has low to moderate resistivities and its highest chargeability value of 12 mV/V occurs at n = 4, which suggests that it is a conductive and deep-seated body.





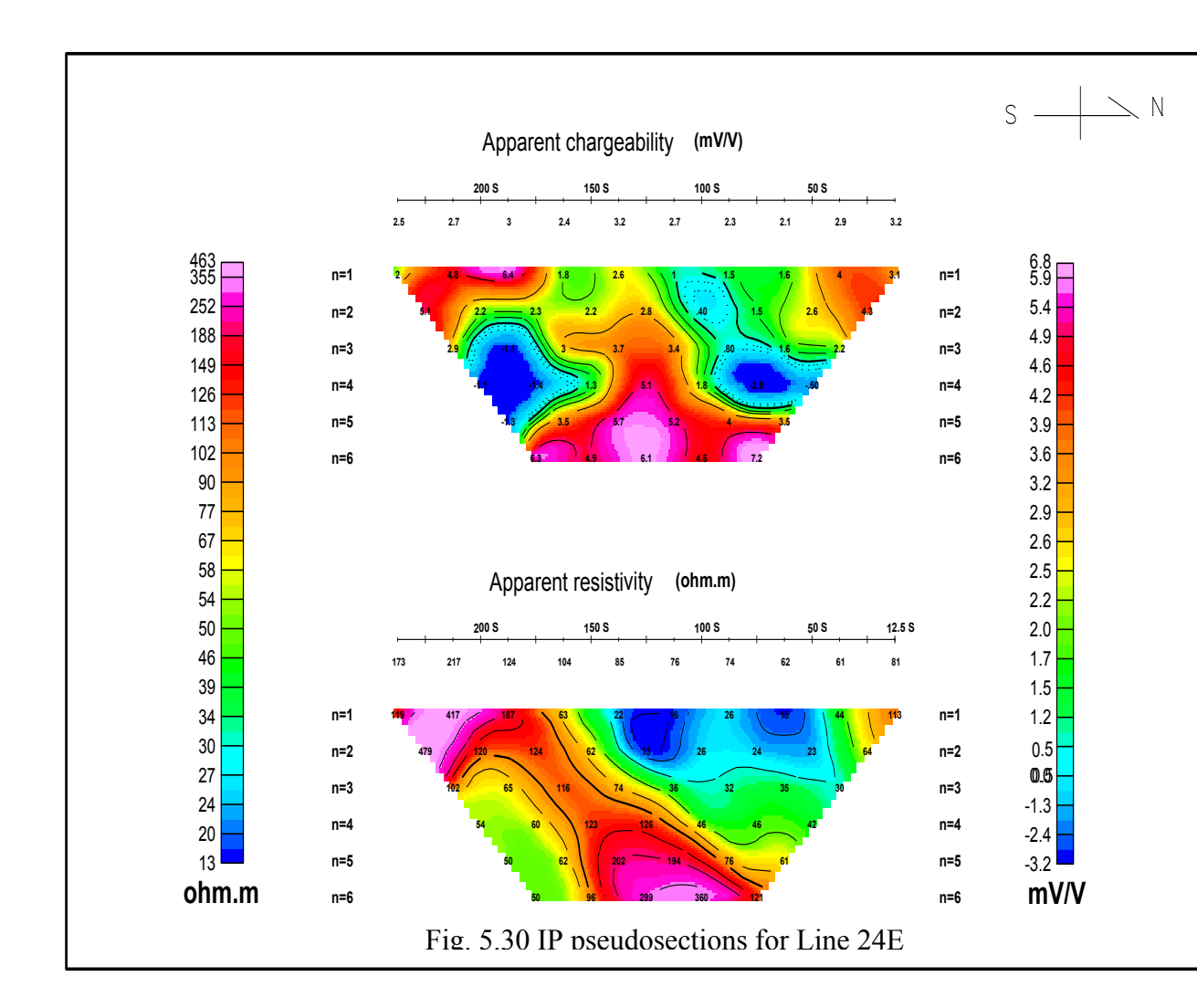


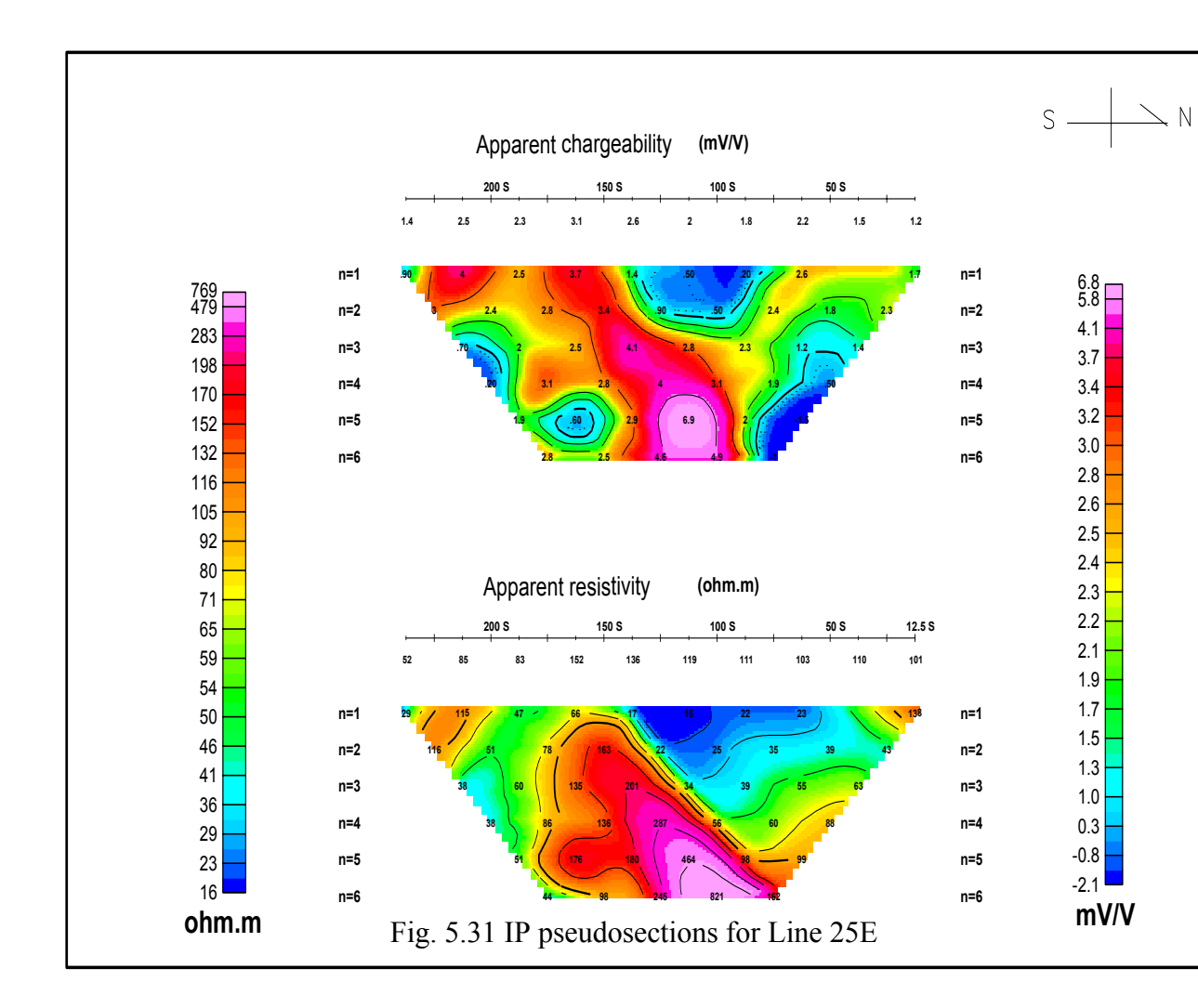
5.3.3.23 Line 24E

Two major chargeability anomalous zones are shown to be located between stations 62.5S and 175S; and between stations 175S and 287.5S (Fig. 5.30). The first anomaly has three peaks at n = 6, which are centred around stations 62.5S, 125S and 162.5S. They all have their highest chargeability values of 7.2, 6.1 and 6.3 mV/V occurring at n = 6. The second anomaly is resistive, and occurs at the southern end of the line. It has its highest chargeability value of 6.1 mV/V at n = 1, which implies that it is a near surface feature.

5.3.3.24 Line 25E

Line 25E shows an anomalous zone which stretches between stations 75S and 150S (Fig. 5.31). It is resistive and has two offshoots coming to surface, having its highest chargeability value of 6.9 mV/V occurring at n = 5. Another small peak is centred on station 212.5S. It starts at n = 1 and may be extending to depth.





Chapter 6

Interpretation, Conclusion and

Recommendations

6.1 Interpretation of Magnetic Results

The magnetic profiles in Appendix B suggest that the northern part of the survey area is a fairly magnetic quiet zone, i.e. there is little variation on the profiles in this zone. This is apparent generally between stations 0S and 100S on Lines 3E up to 7E, 9E, 10E, 12E, 14E, 21E and 25E. This can be due to low susceptibility rocks near the surface. The profiles outline anomaly amplitudes in the range of 540 nT up to 4 200 nT on most of the lines. The causative bodies are near surface as suggested by the small wavelengths ranging between 50 m and 95 m. The shape of the profiles around stations 130S up to 210S, on the majority of the lines suggests the presence of an anomalous feature running WNW - ESE across the study area. On the reduced to the pole map (Fig. 4.8), the fences are coinciding with the Northern magnetic high anomaly from Line 8E up to Line 10E, and they are also coinciding with the Southern magnetic high anomaly on

Line 17E and on Line 23E. The power line is coinciding with the Northern magnetic high on Lines 1E up to 3E. As explained earlier, since most of the magnetic high peaks are independent of the fences and power lines it indicates that these anomalies cannot be attributed to these cultural effects.

The Northern magnetic high anomaly (Fig. 4.8) is trending NW-SE with an average width of 50 m, with a strike of about 1 km from Line 1E up to Line 18E. In this Northern magnetic anomaly there are localized peaks on Line 3E station 200S; between Lines 8E and 9E around station 150S; on Line 12E between stations 125-150S; on Line 16E station 75S; on Line 17E station 187.5S and between Lines 22E and 23E around station 200S. The Southern magnetic high is offset from the Northern anomaly by about 140 m. It has a similar trend and its strike length is 400 m. There is a prominent magnetic low feature, stretching between Lines 13E up to Line 25E and having a SE trend. The boundaries of the anomalies are clearly defined on the analytic signal map (Fig. 4.10).

Comparison of the topographic map (Fig. 1.1) and the total field map (Fig. 4.7) shows that the magnetic highs on the western end of the grid are coinciding with the low lying areas, and those on the eastern corner of the grid are coinciding with the high topography. On the local geology map (Fig. 1.3), the banded ironstone formation is found to be lying on the southern boundary of the farm and the granites are dominant in the south-eastern corner. The prominent NW-SE magnetic anomaly is in the vicinity of the banded ironstone formation, and has a similar trend. Therefore it can be inferred to be the source

of the magnetic anomalies, since ironstones contain magnetite which has a high magnetic susceptibility.

The depths to the top of the anomalous bodies estimated from the magnetic profiles using the half-slope method were found, to be ranging between 6.5 m and 25 m. The average depths to the deep magnetic sources and to the shallow sources were estimated using the power spectrum map (Fig. 4.9), to be 32 +/- 2 m and 8 +/- 1 m respectively. These values suggest in general that the anomalous bodies are near surface features. The anomalies can be due to rocks with a high magnetite content such as ironstones and sulphides.

6.2 Interpretation of Induced Polarisation Results

The induced polarisation method was successful in revealing five anomalous zones, namely WIP1 on the NW end of the grid, WIP2 lying to the west of the survey area, SIP1 located to the south of the grid, NIP1 situated on the northern side and EIP1 which is lying near the eastern end of the study area (Fig. 5.2 - 5.8).

The WIP1 anomaly starts from the surface down to n = 6, which is about 87.5 m using the relation, depth $\sim (n+1)x/2$ (Bertin, 1976). It is most probably due to chargeable and resistive bodies such as disseminated sulphides. The WIP2 anomaly is due to deep-seated, chargeable and less resistive material. It is associated with resistivities as low as

35 Ω m, which suggests that it is highly conductive and polarisable. Graphite has resistivity values in the range of 0.001 up to 10 Ω m and clays have resistivity values in the range of 1 up to 120 Ω m (Parasnis, 1986). Sulphide ore minerals have resistivity values in the range of 0.0001 up to 10 000 Ω m (Robinson and Coruh, 1988). These resistivity values eliminate graphite leaving clays or sulphides as the possible causes of this anomaly. The SIP1 anomaly is near surface and has moderate resistivities. It is highly polarisable and its probable cause could be the same as that for the WIP2 anomaly. NIP1 anomaly is due to a deep-seated chargeable and resistive body. The probable cause of this anomaly is disseminated sulphides. The EIP1 anomaly starts from the surface and it extends down to about 87.5 m. It is conductive and can be due to massive sulphides.

The negative IP effects found on most of the lines can be associated with bodies of limited lateral extent, especially if the bodies are relatively near the electrode contact points. They can be found in horizontally multilayered situations where the lowest layer is more conductive than the layer immediately above and the uppermost layer is at least somewhat polarisable (Sumner, 1976).

The presence of material with resistivity contrasts surrounding a polarisable region can also create an unusual IP response pattern (Sumner, 1976). Negative IP response may occur in the vicinity of 2-D (e.g. dykes) and 3-D (e.g. batholiths) polarisable bodies. Certain 1-D structures also produce negative IP response. This is a geometrical effect

related to the dipolar field and the position of the measuring electrodes (Telford et al., 1990).

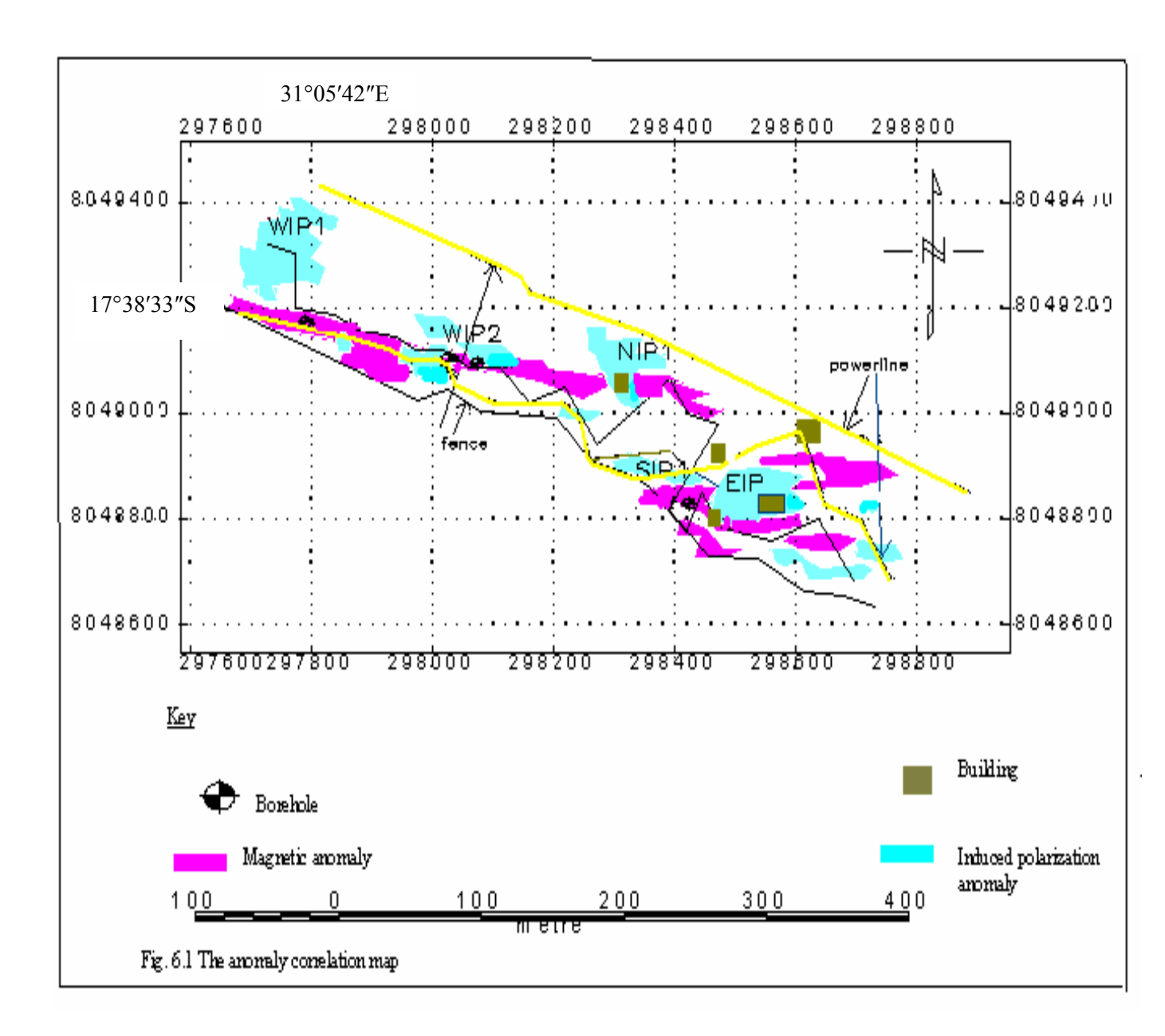
6.3 Correlation of the Magnetic and Induced

Polarisation Results

The correlation map (Fig. 6.1) shows that most of the IP anomalies at the eastern end of the grid are falling under the magnetic high areas. This indicates that there is some degree of correlation between the magnetic and the induced polarisation anomalies.

The induced polarisation anomalies that are overlapping with the magnetic high anomalies include the EIP1 anomaly and part of the SIP1 anomaly. It can therefore be inferred that the causative bodies of these anomalies are possibly massive sulphides or magnetite, since these give a good magnetic response. This eliminates the possibility that clays are a possible cause of these anomalies since they give a poor magnetic response. The northern half of the SIP1 anomaly can be due to disseminated sulphides. These disseminated sulphides are probably associated with massive sulphides forming a halo on the eastern half of the anomaly.

Several induced polarisation anomalies including the WIP1, NIP1 and WIP2 anomalies are located in magnetic low regions. It can be deduced that their causative bodies are probably clays or disseminated sulphides.



6.4 Discussion and Conclusion

The magnetic method was successful in outlining two linear magnetic high trends, namely the Southern (which is lying in a low resistivity zone) and the Northern magnetic highs which run across the grid. It also shows a magnetic low trend lying S-E towards the eastern end of the grid.

The exact locations and symmetry of the anomalies are shown on the reduced to the pole map (Fig. 4.8) and the analytic signal map (Fig. 4.10) respectively. From Fig. 4.8 it can be concluded that these anomalies are due to high susceptibility rocks such as magnetite and sulphides.

The induced polarisation results were successful in identifying the:

- WIP1 and NIP1 anomalies that are both chargeable and resistive and are attributed to disseminated sulphides;
- EIP1 anomaly which is lying in magnetic high areas, conductive and chargeable and is probably due to massive sulphides and magnetite;
- WIP2 anomaly which is attributed to disseminated sulphides, and
- the SIP1 anomaly which is conductive and chargeable and is attributed to massive sulphides.

It therefore can be concluded that both methods were successful in locating the anomalies in the study area.

6.5 Recommendations

Since gold is associated with sulphides, IP is the best method to use as disseminated sulphides give a strong IP response. Geochemical sampling is strongly recommended in order to confirm the presence of the sulphides themselves and also the presence of gold in the sulphides. It is also important for estimating the profitability of opening a gold mine in the area. Drilling is also recommended before any mining activities take place in order to confirm the presence of the gold mineralization. Possible sites for drilling include Line 1E around station 150S and Line 19E around station 225S.

The location of boreholes e.g. towards the end of Lines 3E and 7E (Fig. 6.1) can be taken as a confirmation for areas of low resistivity on the pseudosections for these lines (Fig. 5.10 and Fig. 5.14). Since water is very important on a dairy farm the following target areas for water have been identified, based on resistivity data: Line 14E around station 112.5S, Line 17E around station 250S and Line 23E around station 100S.

References

Baldock, J.W., 1991. The Geology of the Harare Greenstone Belt and Sorrounding Granitic Terrain. Zimbabwe Geological Survey Bulletin No. 94, Zimbabwe, p 13 - 24.

Bertin, J., 1976. Presentation and Application of the IP Method Case Histories. Vol. 1 of Experimental and Theoretical Aspects of Induced Polarisation. Geopublication Associates, Gebruder Borntraeger. 250pp.

Blakely, R.J., 1996. Potential Theory in Gravity and Magnetic Applications. Cambridge University Press, Cambridge. 441pp.

Breiner, S., 1973. Applications Manual for Portable Magnetometers. GeoMetrics, California. 58pp.

Campbell S.D.G and Pittfield P.E.J., 1994. Structure and Related Gold Deposits of Greenstone belts in Northern Zimbabwe Craton. Zimbabwe Geological Survey Bulletin No. 101, Zimbabwe, p 147 - 150.

Dobrin, M.B. and Savit, C.H., 1988. Introduction to Geophysical Prospecting. McGraw Hill International, New York. 867pp.

Foster, R.P., Stove, C.W. and Wilson, J.F., 1986. Archaean Gold Mineralisation in Zimbabwe. In: Anhaeusser, C.R. and Maske, S. (eds), Mineral deposits of southern Africa, Johannesburg, p 43 – 112.

Grant, F.S. and West G.F., 1965. International Theory in Applied Geophysics. McGraw Hill Ltd, New York. 584pp.

Jelsma, H.A., 1993. Granites and Greenstone in Northern Zimbabwe: Tectono-Thermal Evolution and Source Regions. Ph.D. Thesis, Vrije Universiteit, Amsterdam. 267pp.

Milligan P.R. and Gunn P.J., 1997. Enhancement and Presentation of Airborne Geophysical Data. Journal of Australian Geology and Geophysics 17, p 64 – 75.

Milsom, J., 1989. Field Geophysics. Halsted Press, New York. 182 pp.

Parasnis, D.S., 1979. Principles of Applied Geophysics, 3rd Edition. Chapman and Hall, New York. 275 pp.

Parasnis, D.S., 1986. Principles of Applied Geophysics, 4th Edition. Chapman and Hall, New York. 402 pp.

Reynolds, J.M., 1997. An Introduction to Applied and Environmental Geophysics. John Wiley and Sons Ltd, England. 796 pp.

Robinson, E.S. and Coruh, C., 1988. Basic Exploration Geophysics. John Wiley and Sons Ltd, England. 562 pp.

Sheriff, R.E., 1984. Encyclopedic Dictionary of Exploration Geophysics, 2nd Edition. Society of Exploration Geophysicists, United States Of America. 323pp.

Sumner, J.S., 1976. Principles of Induced Polarisation and Geophysical Exploration. Elsevier Scientific Publishing Company, Amsterdam. 277 pp.

Swift, W.H., 1961. An Outline of the Geology of Southern Rhodesia. Government Printer, Salisbury. 73pp.

Telford, W.M., Geldart, L.P. and Sheriff, R.E., 1990. Applied Geophysics, 2nd Edition. Cambridge University Press, Cambridge. 770pp.

Vinyu, M.L., 1994. The Geochronology and Geochemistry of Post-Orogenic

Granitoids within the Harare-Shamva Greenstone belt. Ph.D. Thesis, University of Zimbabwe. 340pp.